Sources of high temperature degradation of cement-based materials: Nanoindentation and Microporoelastic Analysis

by

Matthew J. DeJong

Bachelor of Science, University of California at Davis (2001)

Submitted to the Department of Civil and Environmental Engineering
in partial fulfillment of the requirements for the degree of

Master of Science in Civil and Environmental Engineering

at the

MASSACHUSETTS INSTITUTE OF TECHNOLOGY

June 2005

Signature of Author ....
Department of Civil and Environmental Engineering
May 6, 2005

Certified by ....
Franz-Josef Ulm
Associate Professor of Civil and Environmental Engineering
Thesis Supervisor

Accepted by..... ....
Andrew J. Whittle
Chairman, Departmental Committee for Graduate Students

Sources of high temperature degradation of cement-based materials: Nanoindentation and Microporoelastic Analysis

by

Matthew J. DeJong

Submitted to the Department of Civil and Environmental Engineering
on May 6, 2005, in partial fulfillment of the
requirements for the degree of
Master of Science in Civil and Environmental Engineering

Abstract

The effects of high temperature exposure on cement-based materials have been under investigation for quite some time, but a fundamental understanding of the sources of high temperature degradation has been limited by measurement capabilities. Using recent developments in nanotechnology and microporoelastic modeling, this study identifies sources of high temperature degradation at the nanoscale for the first time.

For reference and comparison with existing literature, the traditional methods of thermogravimetry, uniaxial compression, and resonant frequency are used to measure mass loss, compressive strength and elastic modulus, respectively. However, microscopic measurement of the elastic modulus and hardness is the primary experimental focus of this study. Microindentation is used to measure the properties of homogenized cement paste, whereas nanoindentation is used to measure the properties of the various phases which make up cement paste. All experimental methods are performed on cement paste subjected to specified investigation temperatures ranging from 25°C to 700°C.

Using experimental results in combination with data in the literature, microporoelastic modeling is used to identify the sources of high temperature elasticity degradation which are inherent to each cement paste phase. Only through this unique combination of experimental and theoretical investigations are two primary sources of high temperature elasticity degradation separately identified at the nanoscale: 1) dehydration (loss of bound water) within the elementary building block of C-S-H, and 2) a decrease in packing density of both the low-density and high-density C-S-H phases above 300°C.

Based on these identified sources of high temperature elasticity degradation, a model which predicts the elasticity of cement paste as a function of temperature (up to 700°C) is developed.

Thesis Supervisor: Franz-Josef Ulm
Title: Associate Professor of Civil and Environmental Engineering

Acknowledgements

First, I would like to acknowledge Professor Franz-Josef Ulm whose vision and expertise were vital to the completion of this research study. I also gratefully acknowledge the Lafarge Group for providing the financial support for this research. Additionally, several other people contributed to this research project that deserve acknowledgement and appreciation. I thank Georgios Constantinides for sharing his expertise regarding indentation testing of cement-based materials. His work in this field is what this research study is built upon. I thank Dr. Alan Schwartzman, director of the NanoMechanical Laboratory at MIT, and Chris Bobko for their assistance with indentation testing. I thank Dr. John T. Germaine for sharing his expertise in laboratory testing and for his assistance with macroscopic testing. I also thank all the members of the research group for making my research experience enjoyable: Chris Bobko, Sophie Cariou, Georgios Constantinides, JongMin Shim, Emilio Silva, and Matthieu Vandamme. Last, I thank Cara, whose support cannot be measured.

Contents

List of Tables

List of Figures

Part I

General Presentation

Chapter 1

Introduction

1.1 Industrial Context

Concrete is the most widely used construction material in the world today because its properties are well-known and it is relatively inexpensive. Its many structural applications include buildings, bridges, dams, etc. Under normal exposure conditions, the majority of concrete applications never experience temperatures above about 50°C. However, in these same cases, the response of concrete due to high temperature is still critical due to the possibility of exposure to fire. Design of structures to preserve human safety during the event of a fire has been a concern for a long time, but recently, with the collapse of the World Trade Center, the issue of fire resistance has resurfaced. Furthermore, with the increased design of tall buildings with massive monolithic concrete cores, a better understanding of the effect of high temperatures exposure on cementitious materials is required in order to verify the safety of such structures in the event of a fire.

In general, concrete demonstrates a good resistance to high temperature exposure compared with other building materials, and has therefore been widely used for specific high temperature applications. Concrete walls and floors are often exposed to high temperatures in industrial application where furnaces or other high temperature machinery are present. Another critical application which initiated a lot of research was the use of concrete for containment vessels, such as nuclear reactor pressure vessels which contain a high temperature environment and must also resist significant pressures.

1.2 Characteristics of Concrete Exposed to High Temperature

Because the effect of high temperature on concrete has been studied for some time, significant knowledge is available on this topic. It is known that high temperature exposure causes dehydration of the cement paste, a change in mechanical properties, expansion/shrinkage, cracking, possible spalling, discoloration, etc. At this time it is necessary to discuss the source of some of these effects in order to provide a focus for this study.

Explosive spalling is an effect of high temperature exposure which has been studied a lot. It is known to occur when concrete is exposed to very rapid heating, but the physical origin is still debated. The two main explanations are: 1) pressure build up caused by the low permeability of concrete, and 2) restrained thermal dilation which causes compressive stresses parallel to the heated surface [54].

When concrete is heated, significant cracking may occur which does not cause explosive spalling. This thermally induced cracking is also known to increase with higher rates of heating. Cracking can be caused by pressure build up or differential expansion/shrinkage. Differential expansion/shrinkage can be caused by thermal gradients within the material which occur as a result of rapid heating, but are also caused by the different thermal properties of the cement paste, sand and aggregate. After a slight initial expansion upon heating, cement paste shrinks significantly upon continuous heating to higher temperatures [19] [45], while all types of aggregates expand continuously when heated [6]. This differential expansion/shrinkage can cause significant cracking in the concrete. Additionally, the various constituents of the cement paste expand/contract at various rates and temperatures, which causes microcracking within the cement paste itself [45].

1.3 Research Motivation and Objective

The majority of the research on the mechanical properties of cementitious materials has been done at the macroscopic scale. At this scale, the researcher is able to investigate concrete, mortar, or cement paste depending on the mix design, but is unable to investigate the constituents of the cement paste itself. Cement paste is a complex heterogeneous material that acts as the "glue" which holds concrete together. Because of this, an understanding of its behavior when exposed to high temperature is critical in order to explain the effects of high temperature on concrete itself.

The main objective of this investigation is to develop a better understanding of the microstructural evolution of cement paste exposed to high temperatures and to determine how this microstructural evolution affects the mechanical properties of the material. Recent advances in the technology of nanoindentation allow the investigation of the mechanical properties of materials at very small scales. This technology will be used to investigate the effect of high temperature on the various constituents of cement paste, with the goal of identifying the specific sources that cause the previously observed high temperature material degradation of concrete. Only cement paste will be investigated, eliminating the effects of differential thermal expansion/shrinkage of sand, aggregates, and cement paste. Slow heating rates will be used to reduce the effects of thermal gradients, pressure buildup, and explosive spalling, in order to focus on the material degradation of cement paste itself.

1.4 Outline of Thesis

This thesis is divided into four main parts. The first part is comprised of two chapters. After this introduction, which has described the topic under investigation and the motivation for the research, Chapter 2 summarizes the existing knowledge of the proposed topic. Of particular importance is the introduction of the four-level microstructure of cementitious materials, and the existing knowledge of the change in porosity and elasticity of cement paste due to high temperature exposure.

Part II summarizes the experimental investigations performed and the corresponding results. Chapter 3 explains the materials used and the general methods of sample preparation. The specific experiments are then explained, and are divided into two sections: Macroscopic and Microscopic Investigation. The Macroscopic Investigation (Chapter 4) includes Thermogravimetry, Porosity (using Mass Loss), Uni-Axial Strength, and Resonant Frequency testing, which have all been previously applied to cement paste after exposure to high temperature. Results will be compared to results found in the literature. The Microscopic Investigation and includes both microindentation (Chapter 5) and nanoindentation (Chapter 6) of cement paste after exposure to high temperatures, and is the first experimental investigation of its kind. Results will be compared to macroscopic results and used for modeling in Part III.

Subsequently, Part III of this thesis involves the application of a multiscale microporoelastic model for cementitious materials using the knowledge gained in this study and found in literature. Chapter 7 introduces two microporoelastic models developed for cementitious materials by Ulm and Constantinides [56] [12]. Chapter 8 includes the application of these models to determine the sources of high temperature elasticity degradation at the microscale that lead to the observed elasticity degradation at the macroscale. The model is also used to compare the results of microindentation and nanoindentation. Using the results of microporoelastic modeling, steps towards developing a design tool which can predict the high temperature elasticity degradation of any cement paste are taken (Chapter 9).

Last, Part IV summarizes the conclusions of this study and gives suggestions for future research (Chapter 10).

1.5 Industrial Benefits

With a better understanding of the material behavior of cement paste exposed to high temperatures, the resistance of concrete to fire will be better understood and safer concrete structures can be built. Specifically, with the identification of the main sources of thermal degradation at the nano-scale, cement paste can be designed to optimize high temperature (fire) resistance.

Chapter 2

Existing Knowledge: Microstructure of Cementitious Materials and the Effects of High Temperature Exposure

In order to develop the context in which the experimental investigation was executed, an understanding of the existing knowledge of the response of cementitious materials to high temperature exposure is required. Therefore, this chapter will attempt to summarize the existing knowledge that will be built upon throughout the following chapters. First, the basics of cement chemistry are reviewed in order to understand the multiscale microstructure of hardened cement pastes that will be presented. Second, the multiscale microstructure, which separates the important phases of cementitious materials, is developed. Third, the effects of high temperature exposure on the multiscale microstructure of cementitious materials is discussed. This section includes a summary of previous investigations into the effects of high temperature exposure at each scale. Last, the porosity of cementitious materials is discussed separately because previous investigations access the porosity at each scale of the microstructure simultaneously.

Results of previous investigations are presented in detail because they will be used for comparison to the experimental results of this investigation in Part II. Additionally, the

Compound	Formula	Abbreviation	Typical Mass [%]
Tricalcium silicate	$3CaO.SiO_2$	C_3S	50-70
Dicalcium silicate	$2CaO.SiO_2$	C_2S	15-30
Tricalcium aluminate	$3CaO.Al_2O_3$	C_3A	5-10
Tetracalcium aluminoferrite	$4CaO.Al_2O_3.Fe_3O_3$	C_4AF	5-15

Table 2.1: Major compounds present in ordinary Portland cement (OPC) with corresponding typical mass percentages [52].

results of these previous investigations will be used to supplement the experimental results in Part II to allow microporoelastic modeling in Part III.

2.1 Cement Chemistry

Before reviewing the existing knowledge regarding the response of cementitious materials to high temperature, it is necessary to review the basics of cement chemistry from which to build on. The following abbreviations of cement chemistry will be used throughout this thesis: $C = CaO$; $S = SiO_2$; $A = Al_2O_3$; $F = Fe_2O_3$; $\underline{S} = SO_3$; $H = H_2O$.

2.1.1 Hydration

The four dominant compounds in Portland cement which react with water to form the hydration products seen in hardened cement paste are summarized in Table 2.1.

The two silicate compounds from Table 2.1 react with water to form the following products:

$$\begin{aligned} 2C_3S + 10.6H &\longrightarrow C_{3.4}S_2H_8 + 2.6CH \\ 2C_2S + 8.6H &\longrightarrow C_{3.4}S_2H_8 + 0.6CH \end{aligned} \tag{2.1}$$

Because the silicate compounds comprise a large percentage of Portland cement (see Table 2.1), the most prevalent product in hardened cement paste is calcium silicate hydrate ($C_{3.4}S_2H_8$), which is commonly abbreviated as C-S-H. The abbreviation C-S-H is used because of the amorphous or poorly crystalline structure of calcium silicate hydrate, and consequently the dashes indicate that no particular composition is implied [52]. The two silicate reaction equations represent the most important of the compound reactions because C-S-H generally comprises

50-70% of the final volume of hardened cement paste, and portlandite (CH) generally comprises 15-20% of the final volume. The exact percentages depend on several factors including the water/cement (*w*/*c*) ratio.

The hydration of tricalcium aluminate is a much more rapid reaction and is defined by the following set of equations:

$$\begin{gathered} 2C_3A + 27H \longrightarrow C_4AH_{19}{+}C_2AH_8 \\ 2C_3A + 21H \longrightarrow C_4AH_{13}{+}C_2AH_8 \\ C_3A + CH + 12H \longrightarrow C_4AH_{13} \end{gathered} \tag{2.2}$$

In addition to these reactions, ettringite can also form, if sulfates (SO_4^+) are present, according to the following reaction:

$$C_3A + 3C\underline{S}H_2{+}26H \longrightarrow C_6A\underline{S}_3H_{32} \tag{2.3}$$

However, once all of the sulfates are consumed, the ettringite reacts with aluminates and water to form an additional aluminate product through the following reaction:

$$2C_3A + C_6A\underline{S}_3H_{32}{+}4H \longrightarrow 3C_4A\underline{S}_3H_{12} \tag{2.4}$$

Depending on the mix design of the cement paste, all of the ettringite could be consumed, but some ettringite usually remains present throughout the hydration period [52].

The final hydration reaction involves aluminoferrite and produces hydrogarnet as described by the following equation:

$$C_4AF + 3CH + 10H \longrightarrow 2C_3(A, F)H_6 \tag{2.5}$$

The hydration reactions presented in this section are known to be simplified and are not comprehensive of all the reactions occurring during the hydration of Portland cement. However, they do summarize the hydration of the main products present in hardened cement paste and therefore include the major components which will be considered in this investigation into the response of cement paste to high temperature exposure.

2.1.2 Dehydration: The Effect of High Temperature Exposure

The basic effect of high temperature exposure on cement paste is the removal of water due to evaporation and dehydration. Although they might seem simple, these two processes cause numerous effects on the properties of cement paste. Upon initial heating from room temperature (~20°C), water is lost through evaporation of the unbound water in the pores of the cement paste. This process is straight forward, and evaporation is complete upon heating to 105°C [29] [6]. However, dehydration refers to the loss of chemically bound water from the cement paste, and is a much more complex process. Each constituent of the cement paste dehydrates at different temperatures and at different rates and will be discussed separately.

Dehydration of C-S-H

The dehydration of C-S-H is the most important factor in the decomposition of cement paste exposed to high temperatures, and occurs gradually over a large range of temperatures. The initiation of dehydration is generally assumed to occur when the desorption of evaporable water is complete (105°C), although dehydration may actually begin at slightly lower temperatures [28]. Harmathy [28] describes the dehydration process by the following reaction:

$$\text{C-S-H} \longrightarrow [(1-\xi_{CSH})\,\text{C-S-H} + (0.62\xi_{CSH})\text{C}_2\text{S} + (0.38\xi_{CSH})\text{CS}] + (1.5\xi_{CSH})\text{H} \qquad (2.6)$$

where ξ_{CSH} represents the degree of dehydration which varies from complete hydration ($\xi_{CSH} = 0$) to complete dehydration ($\xi_{CSH} = 1$). The dehydration process occurs gradually from 100°C to temperatures in excess of 800°C, as shown in Figure 2-1 which estimates the function $\xi_{CSH}(T)$ using thermogravimetry and differential thermal analysis. A primary range of C-S-H dehydration is evident from 100-300°C, and a secondary range of C-S-H dehydration is evident from 650-750°C. For simplicity, Harmathy [28] assumes that there are no intermediate dehydration products. This is not the case because of the gradual nature of dehydration, but this model does give a useful representation of the rate and range of temperatures over which dehydration occurs. According to Taylor [52], the complete decomposition of C-S-H corresponding to the formation of C_2S generally occurs at 600°C to 700°C, corresponding with the secondary range of C-S-H dehydration given by Harmathy [28].

Hydration Product	**Dehydration Range** [°C]
Major:	
Calcium Silicate Hydrate (C-S-H)	105-900
Portlandite (CH)	370-580
Minor:	
Hydrated Aluminate	75-700
Ettringite ($C_6A\underline{S}_3H_{32}$)	50-150
Hydrogarnet ($C_3(A,F)H_6$)	200-400

Table 2.2: Temperature dehydration ranges for each hydration product [52].

Dehydration of Portlandite (CH)

The dehydration of Portlandite is a similar but much more rapid process. Harmathy [28] describes the dehydration process by the following reaction:

$$\mathrm{CH} \longrightarrow [(1-\xi_{CH})\,\mathrm{CH} + (\xi_{CSH})\mathrm{C}] + (\xi_{CSH})\mathrm{H} \tag{2.7}$$

where ξ_{CH} again represents the degree of dehydration, but now for CH. The estimated function $\xi_{CH}(T)$ displayed in Figure 2-2 shows the dehydration of CH occurring from 400°C to 600°C [28]. Using thermogravimetric analysis, Taylor [52] found that dehydration starts at temperatures as low as 370°C and is 98% complete at 580°C. Similarly, Lin [36] states that the endothermal dehydration reaction occurs exclusively between 440°C and 580°C.

Dehydration of Minor Hydration Products

Because the rest of the hydration products compose a minor percentage of hardened cement paste, significantly less research has been devoted to their dehydration. Additionally, their contribution to the effects of high temperature exposure on cement paste is usually assumed to be negligible. The temperatures at which significant dehydration occurs in the minor hydration products [52] is given in Table 2.2, but throughout the following chapters their contribution will be generally neglected.

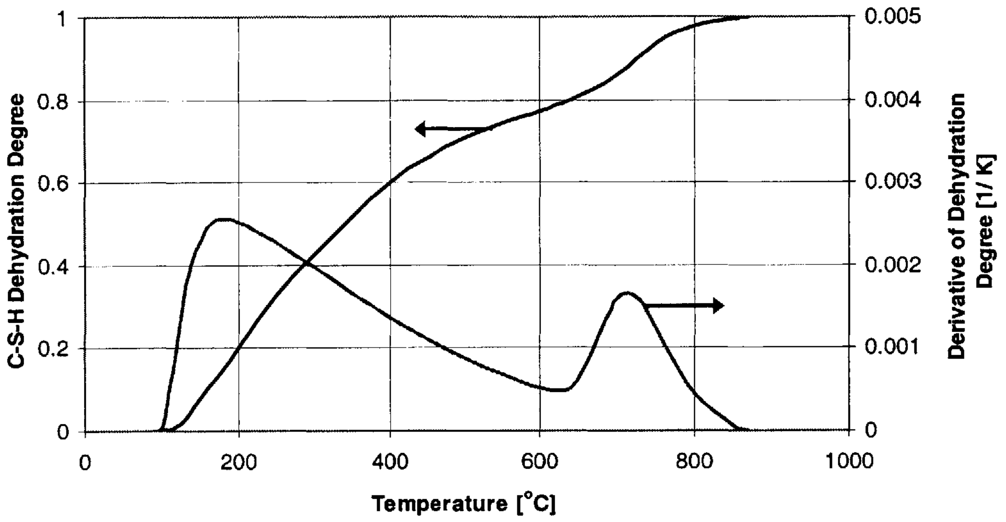

Figure 2-1: Degree of C-S-H dehydration (ξ_{CSH}) and its derivative ($d\xi_{CSH}/dT$) as a function of temperature as estimated by Harmathy [28].

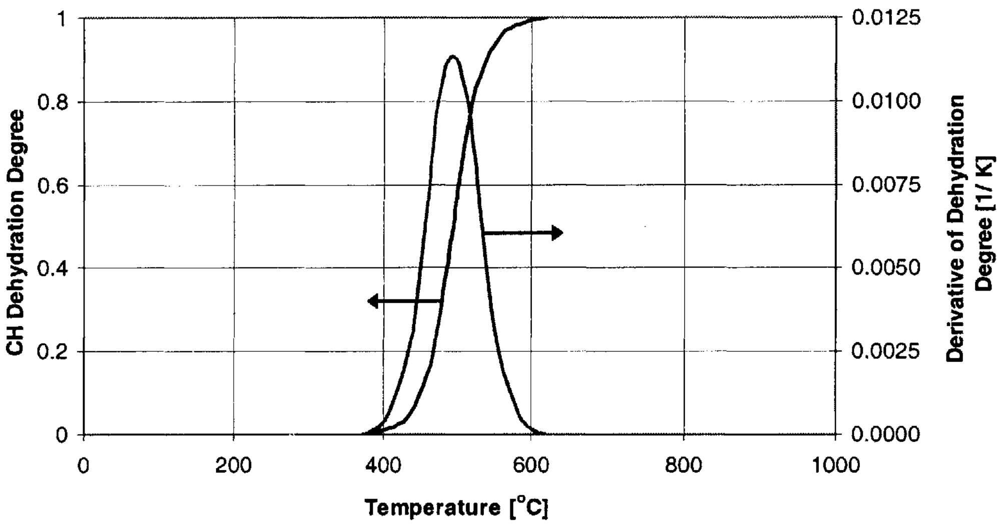

Figure 2-2: Degree of CH dehydration (ξ_{CH}) and its derivative ($d\xi_{CH}/dT$) as a function of temperature as estimated by Harmathy [28].

2.2 Multiscale Microstructure of Cementitious Materials

The summary of the reaction products in hardened cement paste presented in Section 2.1 begins to demonstrate the complex heterogeneous nature of cementitious materials. Furthermore, these reaction products manifest themselves in a range of length scales from the nanometer scale to the millimeter scale. Additionally, in concrete applications, where sands and aggregates are also included in the mix design, the scale of heterogeneity increases up to the macroscopic decimeter scale. In order to comprehensively address the multiscale properties of cementitious materials, an investigation into the length scales of the various constituents is necessary. To this end, a four level microstructure for cement based composite materials was introduced by Constantinides and Ulm [12] [56] and is presented in Figure 2-3. The four levels are separated in scale as indicated by the dimensions given in Figure 2-3. Each level of the microstructure will be discussed in the following sections and the various components of each level of the microstructure will be referred to as phases. 'Level III' of the multiscale microstructure will not be discussed because it includes mortar and concrete which are beyond the scope of this investigation.

2.2.1 Level 0: Basic Building Block of C-S-H (10^{-10}-10^{-9} m)

As mentioned in Section 2.1, C-S-H is the primary product in hardened cement paste occupying up to approximately 70% by volume. For this reason, it is the most important and investigated product in cementitious materials and it has a large effect on the properties of hardened cement paste. Also as stated in Section 2.1, the exact composition of C-S-H is quite variable. However, extensive research has lead to the conclusion of two main types of C-S-H which are described by Jennings [33] as low density (LD) C-S-H and high density (HD) C-S-H, and are described by Constantinides and Ulm [12] as low stiffness C-S-H (C-S-H_a) and high stiffness C-S-H (C-S-H_b), respectively. These two types of C-S-H manifest themselves on 'Level I' and will be discussed in the next section. However, Jennings [33] introduced the idea of the basic building block as a unit of C-S-H that is of a characteristic size of approximately 5 nm. His model depicts these building blocks coming together to form globules, which then flocculate in different formations to form the two C-S-H phases found in 'Level I' of the microstructure (see Fig. 2-4). These

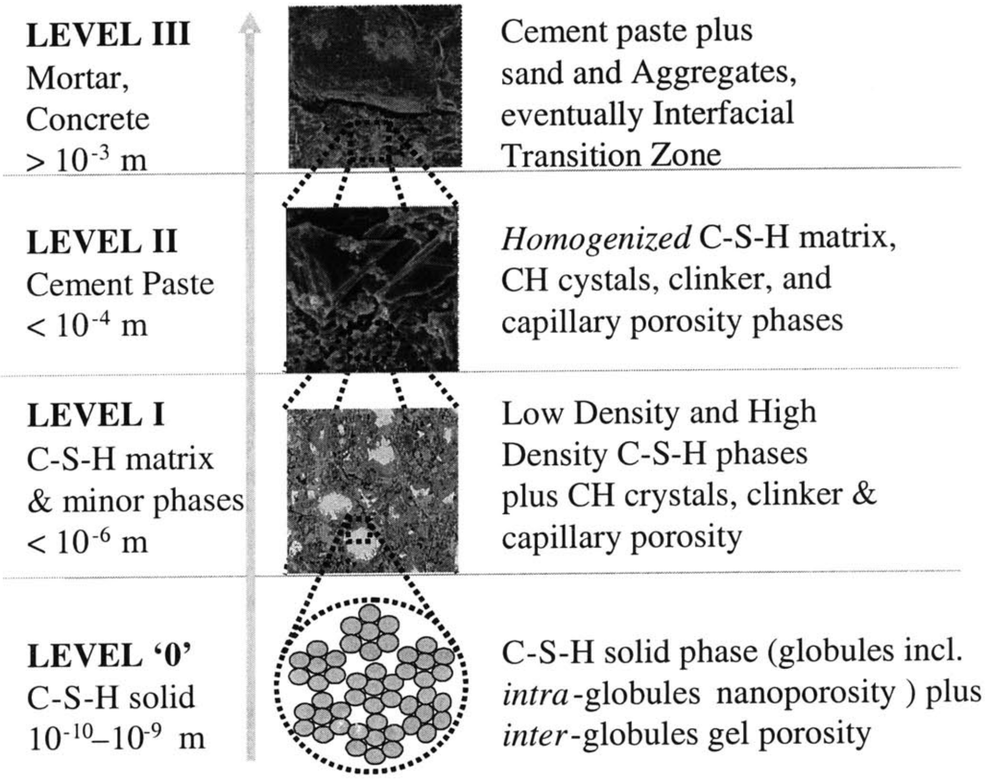

Figure 2-3: Four level microstructure of cement-based composite materials [56].

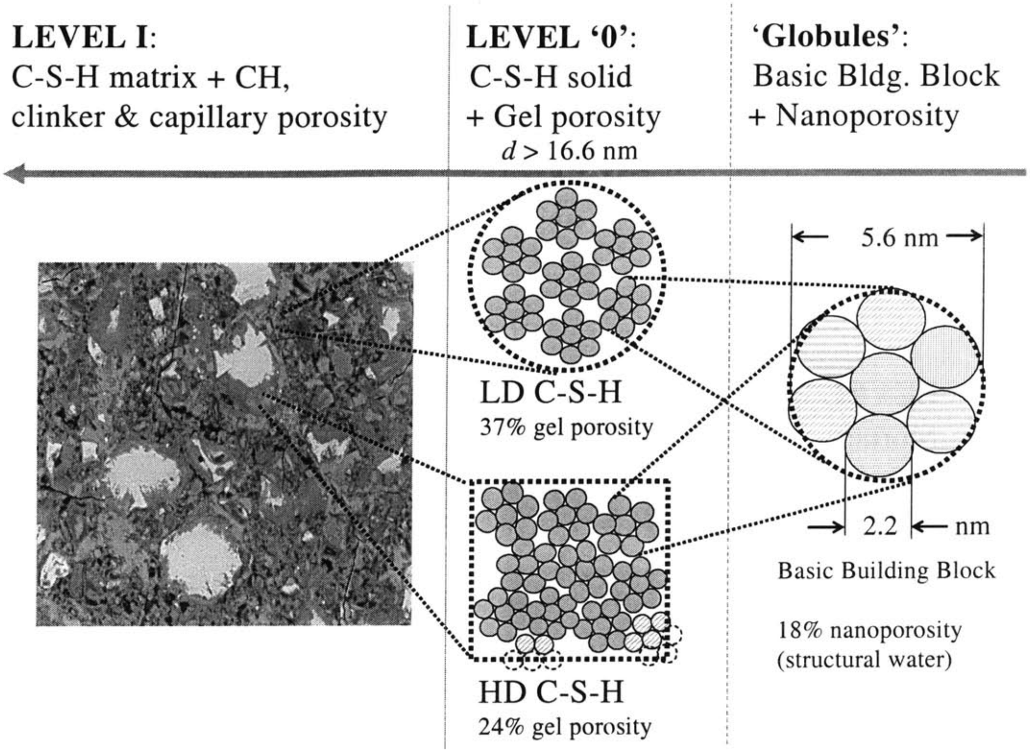

Figure 2-4: Schematic representation of the formation of the two types of C-S-H from the basic building block [56].

individual globules which are formed by an arrangement of basic building blocks are classified as the solid phase of 'Level 0' of the multiscale microstructure. Additionally, a porous 'Level 0' phase, or gel porosity, is formed between the globules when they flocculate together in different packing arrangements to form the two C-S-H phases. These two packing arrangements (or packing densities) are defined by the gel porosities which they create: LD C-S-H gel porosity ($\phi_{LD} = 0.37$) and HD C-S-H gel porosity ($\phi_{HD} = 0.24$) [33][1].

Based on the spherical representation of the basic building block introduced by Jennings [33], it is useful to compare the HD C-S-H and LD C-S-H packing densities to packing density studies in the literature. Several researchers report that the densest possible *ordered* packing of monosized spheres is achieved in the face-centered cubic (fcc) packing arrangement, which has a porosity of $\phi = 0.26$ [2] [47]. In this arrangement, all spheres have 12 contact points with

---

[1] Jennings [33] determined the densities of the two C-S-H phases from which the gel porosities were determined.

surrounding spheres, i.e. a contact number of $N = 12$. The fcc packing porosity is remarkably close to the HD C-S-H gel porosity ($\phi_{HD} = 0.24$), reinforcing the notion that HD C-S-H has a dense, highly ordered structure. Additionally, researchers have found that the densest possible *random* packing of monosized spheres has a porosity of $\phi = 0.36$ and a contact number of $N = 6$ [2] [47]. The densest random packing porosity is remarkably close to the LD C-S-H gel porosity ($\phi_{LD} = 0.37$), and indicates that LD C-S-H is still densely packed but more disordered in nature. This idea of sphere packing density will be explored in future chapters with respect to the effects of high temperature exposure on cement paste.

Based on the model of Jennings [33], gel pore diameters are on the order of 2 nm, but exact pore diameters are uncertain. Powers and Brownyard [46] do not distinguish between the two types of C-S-H but report an average gel porosity of 1.8 nm. The model by Feldman and Sereda [23] identifies gel pore diameters to range from 0.5 - 2.5 nm. One method of measuring porosity on this scale is nitrogen adsorption. Jennings [33] concluded that, using this technique, nitrogen can penetrate only the LD C-S-H and not the HD C-S-H, making a direct determination of the gel porosities impossible experimentally.

2.2.2 Level I: C-S-H Matrix with CH and Clinker Inclusions (10^{-9}-10^{-7} m)

The C-S-H matrix is composed of HD C-S-H and LD C-S-H which are formed by two possible packing arrangements of the globules as shown in Figure 2-4 and discussed in the previous section. The main factor which influences the volume fraction of each type of C-S-H is the w/c ratio. High w/c ratios ($w/c > 0.4$) yield LD C-S-H as the primary phase, while low w/c ratios ($w/c < 0.4$) yield HD C-S-H as the primary phase.

The formation process of LD C-S-H and HD C-S-H during hydration has also been investigated. Taylor [52] describes the formation of an inner product and an outer product during C-S-H hydration. The outer product, believed to correspond to LD C-S-H, forms around clinker grains first and is dominant in cement pastes with high w/c ratios. The inner product, believed to correspond to HD C-S-H, then forms at the interface of the clinker grain and the 'inside' of the outer product (LD C-S-H). Because HD C-S-H formation takes longer, cement pastes cured for short periods of time tend to have less HD C-S-H than fully hydrated cement pastes. Additionally, the thickness of the layers of both types of C-S-H increase over time as hydration proceeds. As a result of their formation process, LD and HD C-S-H are well distributed throughout the cement paste matrix. In other words, large areas of only LD C-S-H or only HD C-S-H, do not tend to occur.

The C-S-H matrix is the dominant phase at 'Level I', however, CH and residual clinker (non-hydrated) are also present in smaller volume fractions and therefore act as inclusions in the C-S-H matrix. Compared to C-S-H hydration, the formation of CH crystals is much more random in nature. Crystals are extremely variable in size, ranging from tens of nanometers up to several hundred micrometers in rare cases. For this study, CH crystal sizes will be assumed to range from 100nm to 1μm, which is a more typical range of sizes. In addition to crystal sizes being highly variable, CH crystal locations are highly variable as well. Unlike C-S-H, they are not necessarily well distributed by the formation process. In fact, since CH crystal distribution is much more random, certain areas may have significant crystal concentrations, while other areas may have very little CH.

Capillary pores also have a characteristic diameter in the 100 nm to 1 μm range and are known to form in two primary ways: chemical shrinkage during hydration and excess water beyond what is needed for hydration. First, chemical shrinkage occurs because the density of combined water in C-S-H is greater than the density of water itself, so the hydration process results in a slight decrease in total volume. This allows capillary pores to develop between hydration products. These pores can sometimes be filled by further hydration. Second, and usually considered of greater consequence, the presence of excess water not needed for hydration causes capillary pores in cement paste. Excess water is only present at w/c ratios greater than 0.38, and capillary porosity increases with the w/c ratio. Fully hydrated cement paste with a w/c ratio of 0.5 generally has a capillary porosity (ϕ_{cap}) in the range of 3-5%.

'Level I' is accessible to mechanical testing by the method of nanoindentation as demonstrated by Constantinides and Ulm [12]. Table 2.3 includes the results of various investigations into the mechanical properties of each of the C-S-H phases. It is critical to note that the mechanical properties of LD C-S-H and HD C-S-H are independent of the mix design, they are inherent properties of the C-S-H phases themselves. This is a direct result of their formation from two basic packing arrangements of the globules introduced in 'Level 0'. A summary of the investigations into the elastic modulus of the CH and clinker phases is given in Table 2.4.

C-S-H Phase	**Elastic Modulus** [GPa]	**Hardness** [GPa]	**Reference**
LD C-S-H	21.7 ± 2.2		Constantinides [12]
	20 ± 2		Acker [1]
	17.9 ± 4.7	0.45 ± 0.17	Constantinides [15]
HD C-S-H	29.4 ± 2.4		Constantinides [12]
	31 ± 4		Acker [1]
	28.9 ± 2.8	0.86 ± 0.19	Constantinides [15]

Table 2.3: Measurements of mechanical properties of C-S-H phases.

Phase	E [GPa]	ν	**Reference**
C_3S-Clinker	135±7	0.3	Velez *et al.* [58]
C_2S-Clinker	130±20	0.3	Velez *et al.* [58]
C_3A-Clinker	145±10		Velez *et al.* [58]
C_4AF-Clinker	125±25		Velez *et al.* [58]
CH	35.24		Beaudoin [8]
	48		Wittmann [59]
	39.77-44.22	0.305-0.325	Monteiro & Chang [38]
	36±3		Acker [1]
	38±5		Constantinides [12]

Table 2.4: Measurements of elastic properties of cement clinker and Portlandite.

These properties are also independent of the mix design. Nanoindentation will be used as described in Part II of this study to investigate the effects of high temperature on the various phases present at this scale.

2.2.3 Level II: Cement Paste (10^{-6}-10^{-4} m)

The C-S-H matrix, CH crystals, clinker grains, and capillary porosity (ϕ_{cap}) introduced in 'Level I' are homogenized to form a single cement paste phase which is defined as 'Level II' of the microstructure. Again, C-S-H is the dominant phase, comprising up to 80% of the volume of the cement paste. Both CH and clinker grains are stiffer than the C-S-H matrix, and can therefore have a significant effect on the mechanical properties of cement paste despite being less abundant. However, at w/c ratios above 0.38, all of the clinker is generally consumed, and the clinker phase is no longer present. The volume of the CH crystal phase tends to increase with the w/c ratio and on average comprises 15% of cement paste. It is therefore critical to the material properties at this scale. The capillary porosity also increases with w/c ratio and is known to significantly reduce elastic properties.

The mechanical properties at this scale are extremely dependent on mix design and have been investigated using several methods which will be discussed in the following section. At this time, it is unnecessary to attempt to summarize all possible mix designs and their corresponding mechanical properties. However, it will be useful to review the results of the mechanical properties of a cement paste similar to what was used in this study. Similar to nanoindentation, microindentation can access the mechanical properties of cement paste at 'Level II'. Constantinides [15] used *microindentation* on Type I OPC with a w/c ratio of 0.5 to obtain an elastic modulus of 20.3 ± 1.6 and a hardness value of 0.515 ± 0.007. These values will be used as a benchmark for the experimental investigation in Part II of this study.

2.3 Effects of High Temperature Exposure on the Multiscale Microstructure

Now that the multiscale microstructure of cementitious materials has been introduced, the effect of high temperature exposure at each scale can be discussed. Previous studies regarding the effects of high temperature will be summarized where available.

2.3.1 Effects of High Temperature Exposure at 'Level 0'

Based on the multiscale microstructure of cementitious materials, the only two effects of high temperature exposure that play a role at the level of the basic building block are the drying out of the nanoporosity ($\varphi_0 = 18\%$, see Fig. 2-4), and the dehydration of C-S-H described by Eq. (2.6). Drying out of the nanoporosity is known to occur by heating cement paste to 105°C, and generally has little effect on the microstructure. Some collapse of the microstructure could occur during drying, the effects of which will be assumed to be negligible. However, the dehydration of C-S-H (Eq. (2.6)) will necessarily occur in the basic building block, and will therefore have a significant effect on the microstructure. The effect of this dehydration reaction is not certain but the following is a list of possible consequences:

1. A change in volume of the basic building block, which could cause:

  - A change in volume of the globules but no change in the nanoporosity.
  - No change in volume of the globules but a change in the nanoporosity.
  - A change in both the volume of the globules and the nanoporosity.

2. A change in the density of the basic building block with no effect on the volume of the globules or the nanoporosity.

3. A change in mechanical properties of the basic building block.

A determination of what is actually occurring at the level of the basic building block is still out of reach the experimental methods currently available. All that can be investigated is a result of some change in the basic building block which manifests itself at larger scales. Therefore, it is beyond the scope of this investigation to determine what is actually occurring at this scale with respect to high temperature exposure.

At a slightly larger scale but still at 'Level 0', the effects of high temperature on the basic building block will have an effect on the gel porosities (ϕ_{LD}, ϕ_{HD}) and the mechanical properties of the globules ($E_{globule}$, $H_{globule}$). Obtaining the mechanical properties of the globules is again still out of reach experimentally. However, the effect of high temperature exposure on the gel porosities has been investigated and will be discussed in Section 2.4.2.

2.3.2 Effects of High Temperature Exposure at 'Level I'

The primary process that will affect this level of the microstructure is the dehydration of C-S-H. Dehydration actually occurs at 'Level 0', but causes a change in mechanical properties at this scale. Microcracking could also occur at this level due to differential shrinkage caused by dehydration. Nanoindentation will be used to experimentally determine the effects of high temperature exposure on the mechanical properties of each C-S-H phase (E_{LD}, E_{HD}, H_{LD}, H_{HD}). The following summarizes the only other investigation into the effect of high temperature on the mechanical properties of C-S-H at this scale.

Němeček *et al.* [40] published the only existing paper on the use of nanoindentation to determine the effects of high temperature exposure on the mechanical properties of C-S-H. Using an indentation depth of 500 nm, the average modulus of elasticity and hardness were

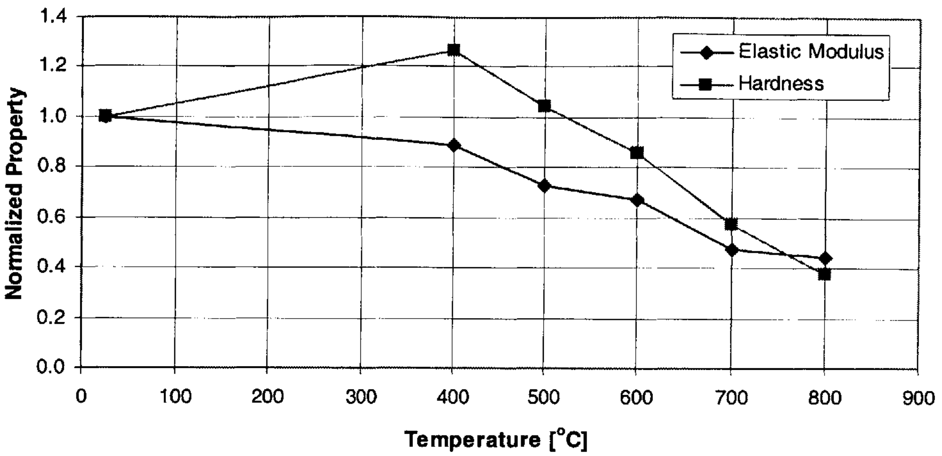

Figure 2-5: Relative residual average mechanical properties of C-S-H after heating to various temperatures (data from Němeček *et al.* [40]).

reported without distinguishing between the two types of C-S-H. The results indicate that specimens tested at room temperature have an elastic modulus of ~60 GPa and a hardness of ~2.4 GPa. These elasticity results do not compare well with the results of Constantinides [12] and Acker [1] who both report an elastic modulus on the order of ~20 GPa and ~30GPa for LD C-S-H and HD C-S-H, respectively (see Table 2.3). Additionally, the hardness results of Němeček *et al.* do not compare well with those of Constantinides [13] who reports hardness values of ~0.5 GPa and ~1.0 GPa for LD C-S-H and HD C-S-H respectively. Despite these discrepancies which seem to indicate an experimental error of some kind, the relative change in elastic modulus and hardness after various high temperature exposures are still of interest, and are displayed in Figure 2-5. Although it is not possible to determine the evolution of properties between room temperature and 400°C, the results show some interesting trends. The hardness shows a net initial increase at 400°C, followed by a relatively constant decrease up to 800°C. The elastic modulus shows a relatively small net decrease at 400°C, followed by significant drop from 400-500°C, relatively little change from 500-600°C, a second significant drop from 600-700°C, and again relatively little change from 700-800°C.

Another important effect of high temperature exposure on this length scale is the dehydration of CH described by Eq. (2.7), which initiates upon heating to approximately 370°C. This dehydration process has a significant effect on the microstructure of cement paste because it occurs in a relatively small range of temperatures and is accompanied by substantial shrinkage. It is well known that the density of CH is 2.340 kg/m^3, while the density of the dehydration product CaO is 3.370 kg/m^3 [43]. This would lead to a shrinkage of approximately 30% during dehydration, which could effectively loosen the CaO grain within a newly created pore space. Lin *et al.* [36] observed the changing morphology of CH after high temperature exposure using a Scanning Electron Microscope (SEM) and reported severe shrinkage and cracking. Handoo *et al.* [27] also used SEM investigation to observe an increase in voids due to the deformation of CH crystals after exposure to 600°C.

High temperature exposure will also have an effect on the capillary porosity at 'Level I'. The initial effect of heating is the evaporation of water from the capillary pores. Evaporation will have some effect on the homogenized mechanical properties of the material, but will have little effect on the microstructure. More importantly, the dehydration of C-S-H and CH could have a significant effect on the capillary porosity. Dehydration causes differential shrinkage/expansion which occurs at different rates and different temperatures in each phase, and could cause microcracking and an increase in capillary porosity. Previous investigations into the effects of high temperature exposure on the capillary porosity will be discussed in Section 2.4.2.

2.3.3 Effects of High Temperature Exposure at 'Level II'

The effect of high temperature on cement paste at this scale ('Level II') has been investigated using several different methods to access a variety of different properties. The following sections will attempt to summarize the known effects of high temperature on the primary mechanical properties of cement paste.

Modulus of Elasticity

The modulus of elasticity of cementitious materials has been studied by several researchers and is known to decrease with exposure to high temperature. Various experimental methods have been developed in order to measure the modulus of elasticity, but these methods are divided into two main categories: static modulus of elasticity tests and dynamic modulus of elasticity tests. Specific testing methods will be discussed further in Chapter 4, but at this time previous research studies concerning the modulus of elasticity will be presented.

The most comprehensive study into the mechanical properties of cement paste after exposure to high temperatures is that of Dias *et al.* [18]. The elasticity results of the study are displayed in Figure 2-6, upon which Dias *et al.* made the following conclusions:

- The large initial decrease in the dynamic modulus of elasticity indicate that dynamic measurements are especially sensitive to the loss of evaporable moisture in the pore space.
- The plateau in the static modulus of elasticity from 200-300^{o}C correlates well with observations that little change in the porosity of cement paste occurs after exposure to temperatures less than 300^{o}C [48] (also [22] and [35]).
- There is a rapid decrease in the static and dynamic modulus of elasticity of cement paste after exposure to temperatures above 300^{o}C and 375^{o}C, respectively, which is probably due to the onset of increasing porosity [48] (also [35]) and microcracking [45] (also [36]) in that temperature range.
- There is also a sharp drop in modulus of elasticity beyond 600^{o}C which is probably caused by a rapid increase in the dominant pore size [49] (also [35]).

Farage *et al.* [22] also investigated the effect of exposure temperatures up to 300^{o}C on the dynamic modulus of elasticity, and found similar results as Dias *et al.* (see Fig. 2-7). Only a slight decrease in elasticity was observed up to 200^{o}C, followed by a plateau in elasticity from 200-300^{o}C, again corresponding with constant porosity in the same temperature range [48] [22] [35]. Several studies have been conducted on the mechanical properties of mortars and concrete, but results vary significantly depending on the type of aggregate used and are beyond the scope of this investigation. It is noteworthy, however, that the modulus of elasticity of *concrete* often decreases by a factor of 2 between 20^{o}C and 250^{o}C [6], while Farage *et al.* [22] found the modulus of elasticity of *cement paste* to decrease by only 17% between 20^{o}C and 300^{o}C. This clearly demonstrates the importance of the interaction of sands/aggregates with cement paste on the mechanical properties of cement paste after exposure to high temperature.

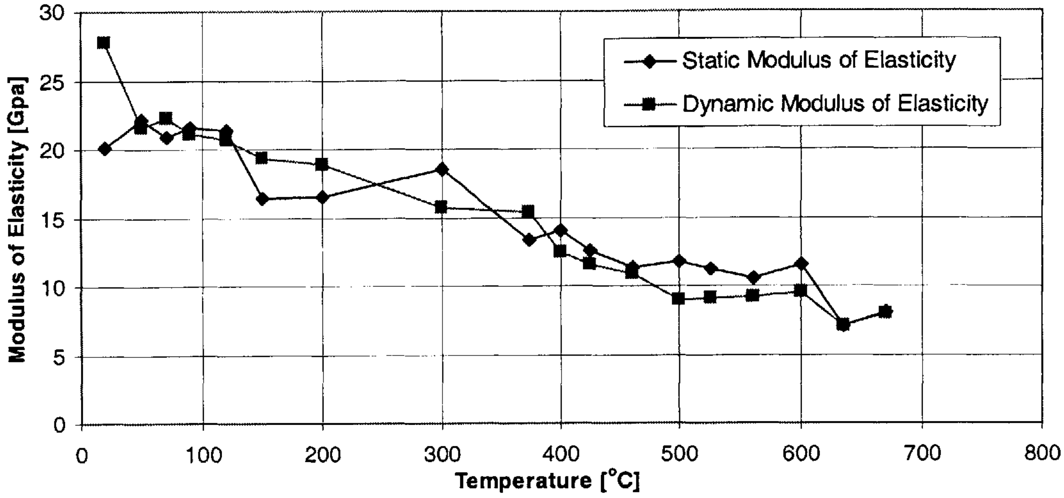

Figure 2-6: Residual dynamic and static modulus of elasticity after heating to various temperatures (data from Dias *et al.* [19]).

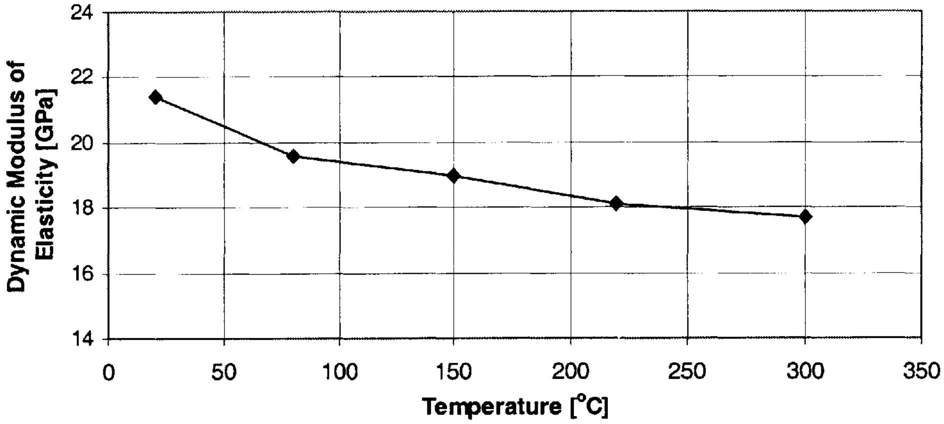

Figure 2-7: Residual dynamic elasticity after heating to various temperatures (data from Farage *et al.* [22]).

Lastly, Masse *et al.* [37] studied the effects of the w/c ratio on the dynamic modulus of elasticity of cementitious materials after exposure to high temperatures. Results showed that lower w/c ratios produce cement pastes with higher dynamic modulus of elasticity values, as expected. However, Masse *et al.* [37] came to the important conclusion that relative changes in elasticity $(E(T)/E_o)$ are the same regardless of the w/c ratio used. Therefore, relative changes in elasticity will be compared throughout this study without regard to the w/c ratio.

Compressive Strength

Dehydration reactions, changes in porosity, changes in pore pressure, and differential expansion/shrinkage are all known to have an effect on the compressive strength of cementitious materials. The results published by various researchers vary significantly due to varying mix designs as well as different experimental techniques. Results from tests on cement pastes which eliminate the effects of aggregates show less variation, and will be used to determine critical temperatures at which significant changes in compressive strength occur.

The investigation by Dias *et al.* [18] provides the most comprehensive study of the effect of high temperature on the compressive strength of cement paste. Figure 2-8 displays residual compressive strengths after heating to various temperatures, from which the following conclusions were drawn:

- The compressive strength of cement paste initially increases when heated and remains greater than the initial strength until exposure to temperatures above 300°C.
- The decomposition of CH causes a significant decrease in residual strength of cement paste after exposure to temperatures greater than 400°C. The source of this strength drop was confirmed by the observation of significant cracking due to the rehydration of CH (in samples exposed to temperatures greater than 400°C) when exposed to atmospheric moisture for extended periods of time after cooling [18].
- Another significant decrease in strength occurs after exposure to temperatures greater than 560°C. This corresponds with the decrease in modulus of elasticity observed beyond 600°C.

Komonen *et al.* [35] also investigated compressive strengths after exposure to high temperatures (see Fig. 2-9) and found a significant drop in compressive strength above 400^{o}C and a second drop in compressive strength beyond 600^{o}C, corresponding well with the results of Dias *et al.* [18].

Because compressive strengths of cementitious materials vary significantly, Bažant [6] made a qualitative assessment of the effects of high temperature exposure on compressive strength and came to the following conclusions:

- After a slight initial decrease, compressive strengths increase with heating up to 200^{o}C, and subsequently decrease continuously at higher temperatures.
- Different w/c ratios cause different initial compressive strengths but have little effect on the relative changes of cementitious materials exposed to high temperatures.
- The rate of heating and cooling can have a significant effect on residual compressive strengths after cooling: the higher the rate of cooling, the greater the reduction in residual compressive strength.

Microhardness

Recently, indentation testing has been introduced as a powerful method of accessing the mechanical properties of cementitious materials at smaller scales. Nanoindentation has been used to access mechanical properties at 'Level I' of the multiscale microstructure as discussed in Section 2.2.2, and microindentation has been used similarly to access mechanical properties at 'Level II' of the multiscale microstructure. Both micro- and nanoindentation will be used and discussed in depth in Part II of this study.

Based on the ASTM E384-99 [5] testing method, Xu *et al.* [61] used a Vickers indenter to determine the microhardness of cement paste ($w/c = 0.5$) after exposure to high temperatures. Test results on OPC are shown in Figure 2-10 and display an initial increase in microhardness up to 250^{o}C, followed by a continual decrease in microhardness thereafter. Results for unheated specimens are on the same order of magnitude as the results by Constantinides [15] given in Section 2.2.3. It is noteworthy that the effect of high temperature exposure on the microhardness is quite similar to the effect of high temperature exposure on the compressive strength discussed

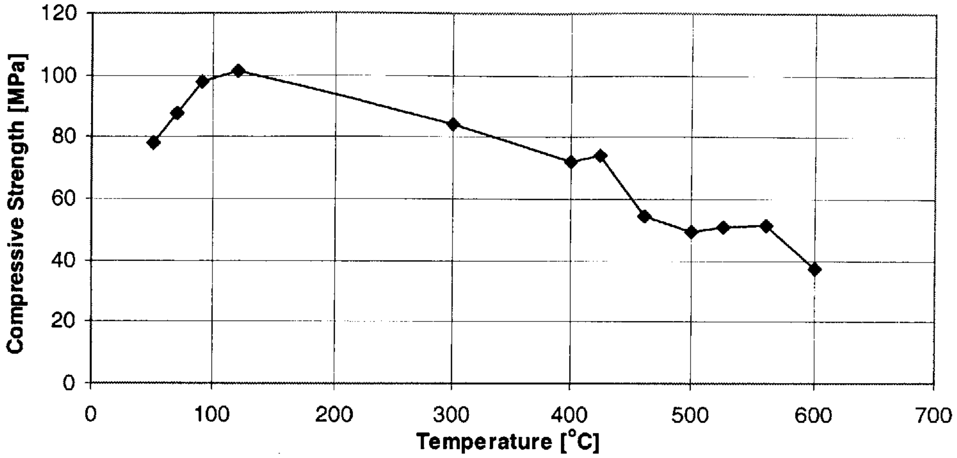

Figure 2-8: Residual compressive strength of cement paste ($w/c = 0.3$) after heating to various temperatures (data from Dias *et al.* [19]).

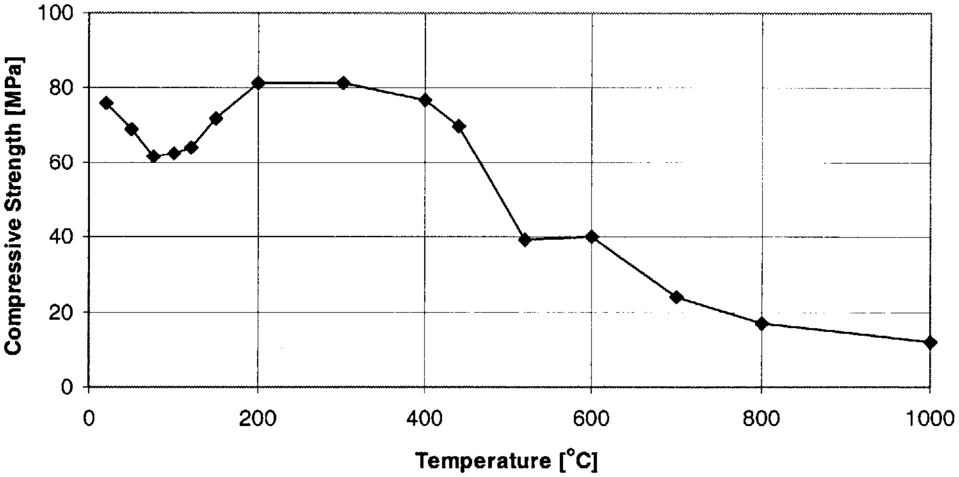

Figure 2-9: Residual compressive strength of cement paste ($w/c = 0.32$) after heating to various temperatures (data from Komonen *et al.* [35]).

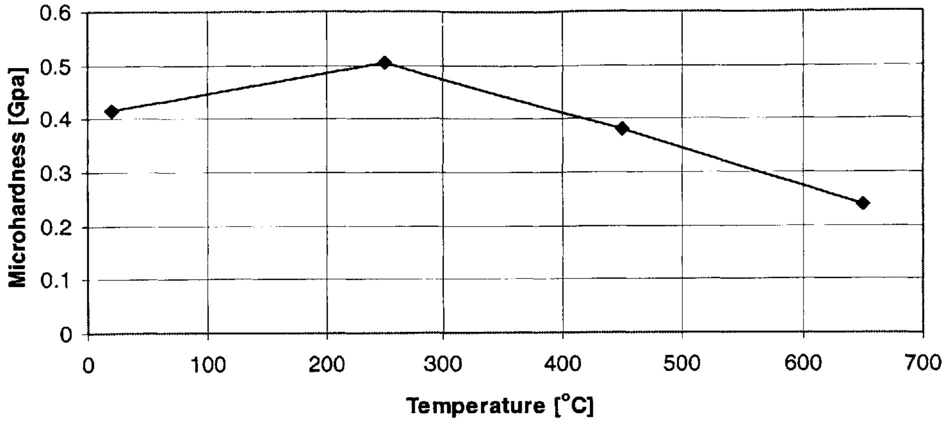

Figure 2-10: Residual microhardness of cement paste ($w/c = 0.5$) after heating to various temperatures (data from Xu *et al.* [61]).

earlier in this section. Microhardness and strength properties will be compared further in Part II of this study.

2.4 Porosity of Cementitious Materials

The effect of high temperature exposure on the porosity of cementitious materials is discussed separately because different porosities are present at each level of the multiscale microstructure and investigation techniques often access multiple scales simultaneously. Methods of measuring porosity will be discussed first, followed by a summary of previous experimental investigations into the effects of high temperature exposure on the porosity of cement paste.

2.4.1 Methods of Measuring Porosity

Porosity is critical to the elastic properties of cementitious materials and has been investigated using several methods. Each method allows measurement of different pore sizes through a variety of techniques. Because of this, results between methods are difficult to compare, and an exact measurement of the actual pore structure is difficult to determine definitively. However, results are comparable within each method, allowing meaningful analysis of the relative porosity of different materials or a single material exposed to different environmental conditions.

Generally, the methods used to investigate porosity include adsorption, small angle scattering, SEM/TEM analysis, mercury intrusion porosimetry (MIP), and weight loss measurements. The methods of MIP and weight loss will now be discussed in more detail because they are the primary methods which have been used for high temperature investigation.

Mercury Intrusion Porosimetry (MIP)

The most prominent method used to investigate the porosity of cementitious materials is MIP. A nonwetting fluid (mercury) is injected under successively higher pressures into a porous cementitious material. The pressure and corresponding injected volume are recorded and then interpreted using the Washburn-Laplace equation in which the diameter of the pores (assumed to be cylindrical) is related to the applied pressure:

$$P = \frac{4\gamma \cos\theta}{d} \tag{2.8}$$

where P is the pressure of the injected mercury, γ is the surface tension of mercury, θ is the contact angle between the mercury and the pore wall, and d is the pore access diameter. Certain assumptions and corrections have been made by various researchers to provide more accurate results (e.g. Cook [16]), but Eq. (2.8) describes the basic relation. Generally, MIP allows access to pore diameters ranging from 3 nm to 375 μm depending on the apparatus [26]. Based on the multiscale microstructure introduced above, this allows access to the capillary porosity (ϕ_{cap}), but the gel porosities (ϕ_{LD}, ϕ_{HD}) are just at the limit of this investigation technique. It is likely that MIP can access the LD C-S-H gel porosity (ϕ_{LD}), but not the HD C-S-H gel porosity (ϕ_{HD}), as will be discussed in Part III.

Although MIP is the most widely used porosity investigation technique, it has several drawbacks. Diamond [17] investigated the accuracy of the technique and states the following conclusions:

- The assumption of cylindrical pores is inaccurate. In reality, SEM images indicate that most pores are clearly not cylindrical, their boundaries are visibly convoluted, and they are often significantly elongated.

- MIP is not reliable as a method of measuring pore size distributions. MIP actually measures pore access diameters, not the diameter of the pores themselves. Accessibility of interior pores to outer surfaces of the specimen is dependent upon the connectivity of the pore space. Interior pores can only be reached through a long percolative chain of intermediate pores of varying sizes and shapes, and some interior pores may never be accessed by the mercury if connectivity is very limited. As a result, all pore diameters will theoretically be underestimated. Comparison with pore size distributions measured using SEM images verify this underestimation. The result of the dependence of MIP on the connectivity of the pore space is the emergence of a 'threshold diameter' corresponding to a pressure below which very little mercury intrusion into the specimen is recorded, and immediately above which the greatest portion of mercury intrusion takes place.

- MIP does provide a valuable method of comparison of the *total intrudable pore volume* and the *threshold diameter* between cement pastes.

One additional concern is the possibility that the application of high mercury pressures used to access fine pores cause the C-S-H gel to collapse, also leading to an incorrect estimation of pore volume [22].

Despite these drawbacks, measurements of pore size distributions using MIP have been shown to be valuable for comparison of the effects of different environmental conditions on the pore structure of cement paste. For example, Galle [26] used MIP to show another important factor related to MIP: the drying process. Before MIP can be used, the water in the pores must be removed. Galle compared the effects of vacuum-drying, freeze-drying, oven-drying at 60^oC, and oven-drying at 105^oC. These drying methods cause differences in the pore structure of cement paste, making it necessary to know the drying method used in order to effectively compare MIP results.

Water Based Weight Loss Measurement

The most basic method of measuring the initial total porosity of cement paste is that of water based weight loss measurements. This method consists of oven-drying saturated cement paste at 105^oC, and measuring the corresponding weight loss. The total porosity (ϕ_{total}) is then given by the following simple equation:

$$\phi_{total} = \frac{M^{sat} - M^{dry}}{\rho^{water} V^{sat}} \tag{2.9}$$

where M^{sat} is the saturated mass, M^{dry} is the dry mass, ρ^{water} is the density of water, and V^{sat} is the saturated volume. Inherent in this equation are the assumptions that: a) no change in the microstructure of the cement paste occurs, and b) complete evaporation of water from all of the pore spaces (ϕ_0, ϕ_{LD}, ϕ_{HD}, and ϕ_{cap}) occurs. In reality, hydrates like ettringite and C-S-H actually begin dehydrating below 105^{o}C, as discussed in Section 2.1 (see Table 2.2), which could affect the microstructure. Galle [26] studied the effect of oven-drying at 105^{o}C using MIP and concluded that significant changes in the microstructure do occur and lead to an overestimation of the total porosity which was attributed to capillary stresses, C-S-H and ettringite dehydration, and microcrack generation. Because of this, Galle suggests oven-drying to 60^{o}C as a more appropriate method of drying for MIP investigation. However, the escape of interlayer water from the C-S-H gel does not occur until temperatures of 90-105^{o}C are reached [24] [36]. Additionally, it is unclear if interlayer water is removed during freeze-drying or vacuum-drying. Therefore, oven-drying at 105^{o}C will be used in this study as a method of determining initial total porosity (Levels 0, I, and II combined), although it might cause slight overestimation.

2.4.2 Effects of High Temperature on the Porosity of Cementitious Materials

Several investigations have been conducted using MIP to determine the pore structure of cementitious materials, but relatively few investigations have focused on the effect of high temperature exposure on the pore structure of cement paste. Additionally, results of these investigations vary because investigators used different types of cement, *w/c* ratios, and heating procedures. In an attempt to summarize the general effects of high temperature exposure on the pore structure, a few investigations will be discussed in detail.

The most comprehensive study using MIP to determine the effects of high temperature exposure on the pore structure of cement paste is that of Komonen *et al.* [35]. Figure 2-11 displays the total pore volume increase and corresponding sample weight loss of cement paste

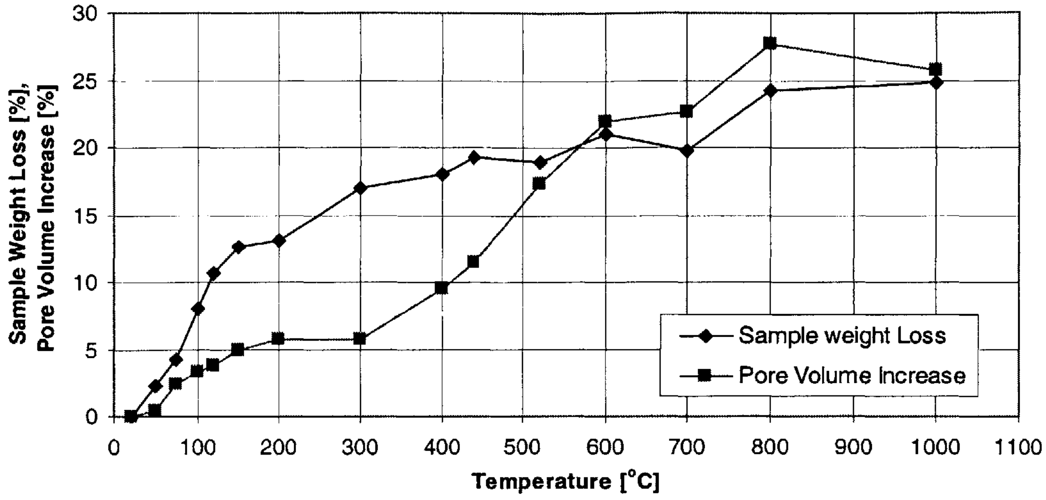

Figure 2-11: Residual pore volume increase (MIP) and sample weight loss after heating to various temperatures (data from Komonen *et al.* [35]).

(w/c = 0.32) after exposure to various temperatures. The study also included investigation into the residual pore size distributions after exposure to each temperature. Although exact pore sizes are not reliable because of the shortcomings of MIP discussed in the previous section, the general evolution of the pore structure was effectively determined. From the results of total porosity and pore size distribution tests, the following conclusions were drawn:

- Below 120°C, pore volume increased due to evaporation and decrystallization of ettringite causing a slight coarsening of the pore structure.
- From 120-300°C, little change in the total pore volume occurred and the volume of mesopores (< 40 nm) was nearly constant. The pore structure coarsened slightly from 200-300°C in the capillary porosity range (>100 nm) but still almost no change in total pore volume was detected. (The gel porosity (~2 nm) also remains quite stable in the temperature range from 150-350°C, but increases at higher temperatures [32].)
- From 300-440°C, the total pore volume increased rapidly while the overall pore size distribution changed only slightly. However, a significant increase in the pore sizes below 10nm occurred.

- From 440-600^{o}C, the total porosity continued to increase rapidly accompanied by an increase in capillary pores (>100 nm) due to the decomposition of CH.
- Above 600^{o}C, the total pore volume continually increased and the most notable coarsening of the pore structure took place. The volume of capillary pores (>100 nm) increased significantly and the average pore size of the capillary pores continued to increase with exposure to higher temperatures.

Komonen *et al.* [35] also noted that the increase of total pore volume up to 300^{o}C was significantly less than could be expected by weight loss measurements (which agrees with investigations on mortar [48]). The premise of this conclusion is that loss of water through dehydration would directly increase the porosity that is detectable using MIP. However, based on the multiscale microstructure introduced in Section 2.2, dehydration would occur in the basic building block of C-S-H, which is well below the pore access range of MIP. Furthermore, dehydration clearly causes shrinkage, which causes an overall decrease in volume. Therefore, because porosity is measured as a percentage of the total volume, shrinkage could cause little change in porosity while weight loss could be significant.

Also noteworthy is the increase in porosity below 10nm after exposure to temperatures of 300^{o}C and above. Additionally, with the observation that the gel porosity (~2 nm) remains relatively constant below 350^{o}C and then increases at higher temperatures. This indicates that the volume and mean pore diameter of the gel porosities increase significantly after exposure to temperatures above 300^{o}C. According to the multiscale microstructure, this would cause a decrease in packing density of LD C-S-H and HD C-S-H, or equivalently an increase in the gel porosities (ϕ_{LD}, ϕ_{HD}).

Lastly, Farage *et al.* [22] studied the effects of temperatures up to 300^{o}C on the pore structure of cement paste ($w/c = 0.4$), and found similar results (see Table 2.5). Total porosity increased significantly up to 150^{o}C, and then remained constant up to 300^{o}C. The threshold diameter, characteristic of the pore diameter of the connectivity of the capillary network, showed little variation with temperature. Farage also reports that pore size distributions changed significantly after exposure to 80^{o}C, but remained relatively unchanged at higher temperatures up to 300^{o}C.

Temperature [°C]	**Threshold Diameter** [μm]	**Total Porosity** [%]
20	0.5	21.0
80	0.2	21.8
150	0.4	24.0
220	0.6	23.8
300	0.4	23.7

Table 2.5: Residual porosity and threshold diameter using MIP after heating to various temperatures (data from Farage [22]).

2.5 Concluding Remarks

As has been demonstrated, the effects of high temperature exposure on cementitious materials have been extensively investigated by several researchers. This chapter was not meant to be an exhaustive summary of all high temperature effects, but rather to set the context for the experimental investigations in the following chapters. Tables 2.6 and 2.7 provide a qualitative summary of the various high temperature effects that have been discussed, with the goal of clarifying and organizing the information obtained for easy comparison and analysis.

Based on extensive investigation of 'Level II' of the microstructure, the effects of high temperature exposure on bulk cement paste are relatively well known. However, the sources of these high temperature effects are still in question. What plays the most important role in the degradation of cement paste due to high temperature exposure? C-S-H dehydration? CH dehydration? Increasing porosity? Microcracking? At what scale is degradation occurring? To answer these questions and get a better idea of the sources which cause thermal degradation of cement paste at smaller scales, this study will attempt to:

- Verify the results of existing studies at 'Level II' of the multiscale microstructure (Chapter 4).
- Verify the results of existing studies at 'Level II' of the multiscale microstructure using a new technique: microindentation (Chapter 5).
- Determine the effect of high temperature exposure on the phase properties at 'Level I' of the multiscale microstructure using a new technique: nanoindentation (Chapter 6).

- Link the effects of high temperature exposure at each scale of the cement paste microstructure using continuum micromechanics (Chapter 8).

In summary, a list of existing studies regarding the phase properties of cement paste is displayed in Table 2.8. Additionally, Table 2.8 displays the chapters in this investigation which attempt to verify previous results or provide new information where no previous studies exist.

Temperature Range [°C]	Dehydration Reactions	Porosity (MIP)	Microstructure (SEM/TEM)
20-105	-Decomposition of ettringite -Possible C-S-H dehydration	-Slight increase	-No observable change -Possible collapse of C-S-H due to removal of interlayer water
105-200	-Primary range of C-S-H dehydration	-Slight increase	-No observable change (slight shrinkage of C-S-H phases)
200-300	-Primary range of C-S-H dehydration	-Constant	-No observable change (slight shrinkage of C-S-H phases)
300-400	-Continual C-S-H dehydration -Possible initiation of CH dehydration	-Significant increase in <10nm range	-Microcracking around CH crystals begins -Physical state begins deteriorating
400-500	-Continual C-S-H dehydration -Primary range of CH dehydration	-Significant increase in <10nm & 100nm range	-Significant microcracking -Deformation of CH creating voids
500-600	-Continual C-S-H dehydration -CH dehydration complete at $\sim 580^{o}$C	-Significant increase in 40nm - 100nm range	-Predominance of microcracking -Deformation of CH creating voids -Disruption at C-S-H boundaries
600-700	-Secondary range of C-S-H dehydration	-Significant increase in >100nm range	-Increase in larger pores -Morphology changes in C-S-H
> 700	-Complete C-S-H dehydration	-Continuous increase in >100nm range	-Continual morphology changes due to dehydration.

Table 2.6: Summary of the effects of high temperature on the physical properties of cement paste ('Levels 0, I, and II').

Temperature Range [°C]	Elasticity	Hardness	Compressive Strength
20-105	-Dynamic elasticity decreases (up to ~20%) -Static elasticity is constant	-Possible slight increase	-Varies between studies -Most likely significant increase (~20-30%)
105-200	-Slight decrease	-Increases	-Constant / slight decrease
200-300	-Relatively Constant	-Constant / slight decrease	-Slight decrease
		-Peaks within this range	
300-400	-Slight decrease	-Continual steady decrease	-Slight decrease
		-Passes below initial value	-Passes below initial value
400-500	-Large decrease (~20-25%)	-Continual steady decrease	-Large decrease (~30-40%)
500-600	-Relatively constant	"	-Constant / slight decrease
600-700	-Large decrease (~15%)	"	-Large decrease (~10-20%)
> 700	-Continual steady decrease	"	-Continual steady decrease

Table 2.7: Summary of the effects of high temperature on the mechanical properties of cement paste ('Level II').

Phase of Microstructure	**Phase Property**	**Investigation Method**	**Existing Info. [Reference]**	**New Info. [Chapter]**
'Level 0':				
C-S-H Globule	Elasticity (E_{glob})	Modeling	-	8
	Nanoporosity (ϕ_0)	-	-	-
Gel Porosity	LD C-S-H (ϕ_{LD})	MIP	[22] [32] [35]	-
		Modeling	-	8
	HD C-S-H (ϕ_{HD})	Modeling	-	8
'Level I':				
LD C-S-H	Elasticity (E_{LD})	Nanoindentation	-	6
	Hardness (H_{LD})	Nanoindentation	-	6
HD C-S-H	Elasticity (E_{HD})	Nanoindentation	-	6
	Hardness (H_{HD})	Nanoindentation	-	6
C-S-H Matrix	Elasticity (E_{CSH})	Nanoindentation	[40]	-
	Hardness (H_{CSH})	Nanoindentation	[40]	-
Porosity	Capillary (ϕ_{cap})	MIP	[22] [35] [44]	-
		SEM	[27] [36]	-
		Modeling	-	8
'Level II':				
Cement Paste	Elasticity (E_{II})	Resonant Frequency	[19] [22] [37]	4
		Static	[19]	-
		Microindentation	-	5
	Hardness (H_{II})	Vickers	[61]	-
		Microindentation	-	5
	Comp. Strength	Uniaxial	[19] [35]	4

Table 2.8: Summary of the existing and missing knowledge regarding the effects of high temperature on the phases of cement paste at each level of the multiscale microstructure.

Part II

Experimental Investigation

Chapter 3

Experimental Overview, Materials, and Specimen Preparation

In order to determine the effects of high temperature exposure on cement paste, experimental investigations were conducted and were divided into two primary sections: 'Macroscopic Investigations' and 'Microscopic Investigations'. Macroscopic investigations refer to tests conducted on bulk cement paste at a length scale $> 10^{-3}$ m, effectively testing a homogenized material at the macroscale. Microscopic investigations include tests on cement paste at both the microscale (10^{-6}-10^{-4} m, 'Level II'), and nanoscale (10^{-9}-10^{-7} m, 'Level I'). Testing at these different length scales will allow a determination of properties at each scale which will be connected through homogenization and upscaling techniques in Chapter 8. The remainder of this chapter will define the state of the material at the time of application of all testing methods.

3.1 Materials

The focus of this study is to determine the effects of high temperature on the material properties of cement paste at the nanoscale, microscale, and macroscale. For this reason, all testing was performed on hardened cement paste, i.e., no sand or aggregate was included in the mix. Cement paste was prepared using Type I Ordinary Portland Cement (OPC) with the composition given in Table 3.1. A w/c ratio of 0.5 was used for all specimens because it is a typical w/c ratio for basic concrete applications and because a large amount of knowledge is available

CaO	**SiO_2**	**Al_2O_3**	**MgO**	**SO_3**	**Na_2O**	**Fe_2O_3**	**K_2O**	**C_3S**	**C_2S**	**C_3A**
62.30	20.80	4.40	3.80	2.90	0.39	2.40	1.28	53.0	20.0	8.0

Table 3.1: Composition of Type I OPC in mass percentage of each component as provided by the manufacturer.

regarding cementitious materials with this *w/c* ratio. Specimens were cast in cylindrical molds and vibrated at the time of casting to remove air bubbles. All specimens were removed from their molds within 7 days of casting and were immediately placed in lime water for curing.

At an age of 28 days, the control specimens (25°C) were removed from the lime water and tested in their saturated state using the various experimental procedures outlined in Chapters 4-6. At the same age (28 days), all the remaining specimens were dried to 105°C to effectively "lock" their hydration state, allowing meaningful comparison with the control specimen results. It is well known that hydration continues well beyond 28 days, so if some specimens were allowed to cure up to 2 or 3 weeks longer than the control specimens, the results would no longer be comparable. After drying, specimens were placed in a desiccator to prevent additional hydration until further heating (or until testing in the case of the 105°C test group). The heating temperatures included in this investigation were as follows: 25°C, 105°C, 200°C, 300°C, 400°C, 550°C, and 700°C. After heating, specimens were again stored in desiccators at all times to prevent rehydration.

Additional specimens remained in lime water and were allowed to cure for 3 months (allowing nearly complete hydration) before heating and testing. These specimens were also stored in desiccators at all times after heating to prevent rehydration.

3.2 Specimen Preparation

3.2.1 Microscopic Investigations

Specimens were cast in 11.5 mm diameter cylindrical molds approximately 60 mm in length. After curing, but before drying, the ends were cut off and specimens were cut into four segments of 10-14 mm in length using a diamond saw. Special care was taken to note which section of the original specimen the samples were cut from: top, top-middle, bottom-middle, and bottom. Only samples cut from the two middle sections of the original specimens were used in testing to reduce the possible effects of sedimentation during the casting and vibration process. The microscopic investigations conducted (nano- and micro- indentation) are both surface tests so extreme care is necessary to prepare a smooth surface to ensure accurate results. For this reason, all specimens were sanded twice using sandpapers of increasing fineness (grit), and then polished using four diamond suspension solutions with diamond particles of increasing fineness. Particle sizes in the diamond solutions ranged from 6.0 μm to 0.25 μm. After polishing, samples were placed in an ultrasonic bath to remove all dust and diamond particles.

After the specimens were prepared, they were dried and heated to various temperatures and were then placed in a desiccator until testing. Ideally, the samples would be polished immediately following heating instead of before heating to eliminate the possibility of the surface roughness increasing during heating due to differential shrinkage or microcracking. However, sanding and polishing after heating was attempted and was found to degrade the surface and increase the roughness instead of making samples smoother. Surface degradation was probably due to the fact that cement paste is more brittle when it is dried, so sanding and polishing created a fractured surface rather than decreasing the surface roughness. Therefore, specimens were polished before heating because it is the best available method. Additionally, polishing before heating should be sufficient because differential shrinkage and microcracking mainly affect the structure of cement paste above 400°C, so the majority of investigated temperatures would not be significantly affected. It should be noted that results from samples heated to higher temperatures could contain effects of increased surface roughness.

3.2.2 Macroscopic Investigations

Specimens used for macroscopic investigation were prepared according to the requirements of each testing procedure. The following summarizes the preparation procedures specific to each testing method.

Uni-Axial Compression

Specimens used for uniaxial compression testing were also cast in 11.5 mm diameter molds of approximately 60 mm in length. After curing, the ends of the specimens were cut off, and specimens were cut into two segments of 20-25 mm in length, to achieve an acceptable diameter/length ratio. The method of Uni-axial compression testing will be discussed in detail in Chapter 4, but at this time it is necessary to mention the necessity of smooth ends to prevent end effects during testing. For this reason, samples were again sanded prior to heating. Uni-axial compression testing was conducted on both the top and bottom segments of the original specimen and results were averaged to cancel out the possible effects of sedimentation.

Resonant Frequency

Specimens used for resonant frequency testing were cast in 10.5 mm diameter cylindrical molds approximately 120 mm in length. After curing, the ends of the specimens were cut off providing samples of 100-110 mm length to achieve a diameter to length ratio suitable to testing methods. Shorter samples (60-100 mm) were also tested to determine if length effects were significant. Five standard sample plus one short sample were tested at each temperature of investigation. Samples were again sanded prior to heating. Sedimentation will have no effect because almost the entire samples were tested and an approximately equivalent amount of material was cut off of each end.

Thermogravimetric Analysis

Samples used for thermogravimetric analysis were cut from the specimens used for microscopic investigations. Samples were cut into cubes with a volume of approximately 5 mm^3, as required by the maximum allowable mass (50 mg) of the testing equipment. The location in the original specimen from which the samples were cut affects the results and will be discussed further in Chapter 4.

3.3 Heating Procedure

The heating procedure has a critical effect on the behavior of cement paste after exposure to high temperature. Heating was performed using a Barnstead FB1400 Furnace with a Eurotherm 2116 temperature controller which allowed programming of heating and cooling rates and the time at maximum temperature. The following outlines the heating procedure used in order to optimize the material state for experimental investigation.

3.3.1 Heating Rate / Cooling Rate

The heating rate and cooling rate can have a significant effect on the state of the material after heat exposure. If specimens are heated rapidly, explosive spalling can occur as discussed in Chapter 1. Explosive spalling is beyond the scope of this investigation, so a slow heating rate was used to avoid spalling behavior.

More importantly, the heating rate needs to be slow enough to limit thermal gradients which can cause excessive cracking of the cement paste. All cracking can not be prevented, but an attempt was made to limit cracking as much as possible. Additionally, dehydration of the cement paste (see Section 2.1) causes the release of bound water into the pore space in the form of vapor. This released water vapor needs to have sufficient time to migrate out of the cement paste through the pore space preventing excessive pore pressures from building up. If heating is too quick, the released water vapor can be trapped causing excessive pressure build up and additional hydration of C-S-H, called 'internal autoclaving' [22] [44]. Ideally, these factors should be avoided and therefore necessitate slow heating rates. However, several temperatures are being investigated so extremely slow heating rates will result in large delays between tests. Based on these factors, specimens were heated and cooled at a rate of 1 K/min. This rate was selected to limit cracking while maintaining a heating time which allowed all temperatures to be investigated within a reasonable time period.

3.3.2 Time at Peak Temperature

The amount of time the specimen is held at the peak temperature is important to ensure a uniformly heated state before cooling. If the heating rate is too fast, a longer time at the peak temperature will allow the entire sample to achieve a thermal state of equilibrium before cooling. Additionally, released water vapor needs time to migrate out of the pore space. Thermal diffusivity decreases with temperature [6], so longer peak temperature exposure will theoretically be necessary at higher temperatures. However, all specimens were exposed to peak temperatures for an excessive period of 24 hours to ensure sufficient time for equilibrium to be reached. Prior to heating, specimens were also dried at 105°C for 24 hours to be certain that all water had been evaporated from the nanopores, gel pores, and capillary pores. Complete drying at 105°C is critical because it is the temperature from which the initial total porosity

Sample Location in Original Specimen	**Total Porosity [%]**
Top	45.4
Top-Middle	44.3
Bottom-Middle	43.4
Bottom	41.5
Average:	43.6

Table 3.2: Initial total porosity measurements ("Water Based Weight Loss Measurement" method) of samples used for microscopic investigations.

calculations are made.

3.4 Initial Porosity Measurements

Initial total porosity was determined using the method of 'Water Based Weight Loss Measurement' introduced in Section 2.4.1. To review, the total porosity is obtained using Eq. (2.9), which requires knowledge of the initial saturated volume, the initial saturated mass, and the dried mass after heating to 105°C. Volume was obtained using a micrometer to measure dimensions with an accuracy of 0.01 mm, and mass was measured to an accuracy of 0.001 grams. The average total porosity of all specimens was 43.6%, which corresponds well with the results of Galle [26] who measured a total porosity of 43.3% for a similar cement paste ($w/c = 0.5$). Additionally, the average porosity of each segment of the samples prepared for microscopic investigation are shown in Table 3.2 and clearly evidence the existence of sedimentation within the specimens.

3.5 Concluding Remarks

The primary goal of this chapter was to define the state of the material (cement paste) at the time of testing. In summary, the following items were addressed:

- **Material:** The material used was Type I OPC with a w/c ratio of 0.5.
- **Sample Preparation:** The material cured for 28 days before drying, heating, and testing. Details of curing, heating, polishing, etc. were discussed.

- **Initial Porosity:** The initial porosity was measured and compared to other investigations. Results were included in this chapter because they give an idea of the initial state of the material, and give no indication of the effects of high temperature. Additionally, initial porosity measurements showed that sedimentation did occur, and needs to be accounted for. Methods of accounting for sedimentation were discussed, but the effects of sedimentation need to be kept in mind when analyzing results in the following chapters.

The state of the material at the time of testing is critical in order to obtain meaningful results. Equally important is the fact that all specimens were cast, cured, dried, heated and stored together. This ensured that the material state of all specimens was the same, regardless of the experimental investigations for which they were used. As a result, comparison of the results of the various experimental investigations can be meaningful.

Chapter 4

Macroscopic Investigation

Macroscopic investigations include all experiments conducted on bulk cement paste: 'Level II' of the multiscale microstructure (see Fig. 2-3). As previously noted, the majority of existing research on cement paste has been performed at this scale. The results of macroscopic investigations are presented in this chapter along with discussion of how the results were interpreted, utilizing comparison with results of previous studies where applicable.

4.1 Thermogravimetry

Thermogravimetry (TG) is a technique which measures the mass change of a sample as a function of temperature. Thermal changes accompanying mass change, such as decomposition, dehydration, etc., can be effectively measured using TG. Generally, the sample is placed on a microbalance inside of a furnace with a programmable temperature schedule. During testing the mass, temperature and time are recorded. Thermogravimetric tests were conducted at the Center for Materials Science and Engineering (CMSE) at MIT using a Perkin Elmer TGA7 Thermogravimetric Analyzer.

Wendlandt [60] includes Calcium Silicate Hydrates (C-S-H) in his discussion of the applications of thermogravimetric analysis, stating that it has been effectively used to quantify the amount of CH in cement paste and the amount of bound water in C-S-H. In this research, however, TG was used for comparison with manual mass loss measurements of samples used for the other investigations in this study. This comparison will be useful to determine whether samples have lost the appropriate mass at any given temperature, providing an assessment of whether the 'Time at Peak Temperature' (see Section 3.3) is long enough for equilibrium to be reached. Additionally, this comparison will be useful to determine if a significant amount of water rehydrates during the cooling period. If either equilibrium is not reached or rehydration occurs, the manually measured mass loss would be less than the mass loss found using TG.

4.1.1 Methods

Thermogravimetric tests were performed on cement paste samples in a temperature range from ~20°C (room temperature) to 1000°C in three stages. First, the temperature was increased from 20°C to 105°C at a nominal rate of 5 K/min in order to remove all evaporable water from the sample. Second, the temperature was held constant at 105°C for 60 minutes to ensure that all evaporable water was removed. This stage is critical to accurately determine the mass of evaporable water lost during heating to 105°C so that the initial total porosity can be calculated using Eq. (2.9). Additionally, allowing the sample to reach equilibrium at 105°C provides an effective division between the initial period of evaporation and the subsequent period of dehydration. Third, the temperature was increased from 105°C to 1000°C at a nominal rate of 5 K/min, during which dehydration occurred.

4.1.2 Results

The results of thermogravimetric analysis are shown in Figure 4-1 which displays the normalized mass loss (current mass divided by initial mass) versus temperature and the derivative (mass rate) of the mass loss versus temperature. The derivative of the mass loss clearly shows the primary range of C-S-H dehydration between 105°C and 300°C, and the primary range of CH dehydration between 400°C and 600°C. The secondary range of C-S-H dehydration is only slightly visible between 650°C and 800°C. The normalized mass loss curve is vertical at 105°C indicating that significant mass loss continues to occur during the second stage of heating (constant temperature). The normalized mass loss after the second stage of heating is 0.755, from which the initial total porosity is calculated to be 46.3%. This is a bit higher than the average porosity of all specimens (ϕ_{total} = 43.6%) found in Section 3.4 using 'Water Based Weight Loss Measurements'.

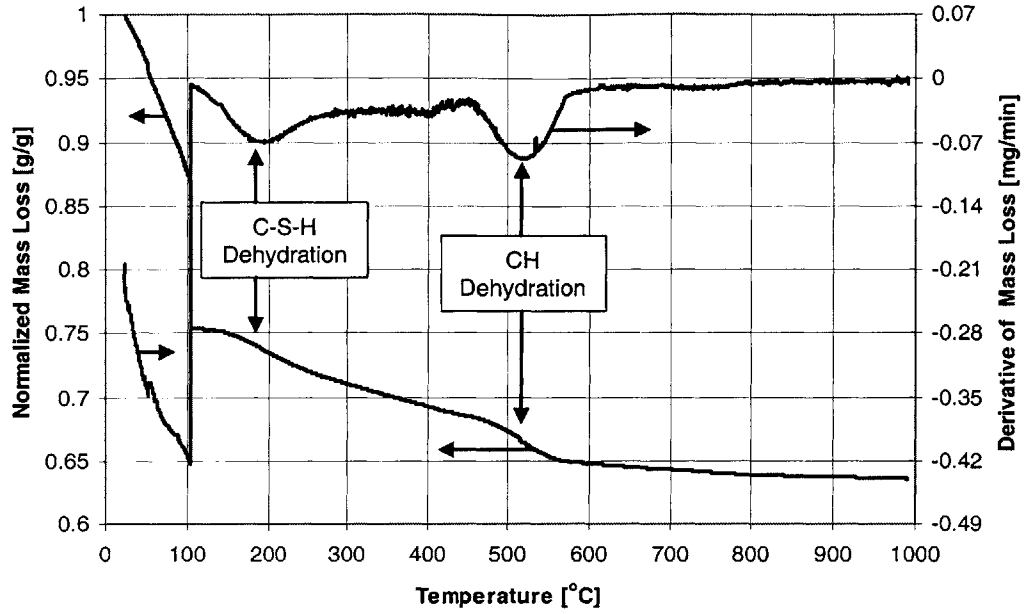

Figure 4-1: Results of thermogravimetric analysis on cement paste.

4.1.3 Discussion

Figure 4-2 shows the average manual mass loss measurements in addition to the results of thermogravimetric analysis. Initial comparison indicates that because manually measured mass losses were less than TG results, equilibrium was not reached or significant rehydration may have occurred during cooling. However, further analysis indicates otherwise. The sample used for thermogravimetric analysis was taken from between the top and top-middle sections of the original specimen (see Fig. 4-3). To check if sedimentation is an issue, the manual mass loss for each section of the original specimens was determined and is shown in Figure 4-4. The results of the thermogravimetric test fit nicely between the top and top-middle results for manual measurements indicating that sedimentation is the cause of the original discrepancy, and that the manual heating procedure is sufficiently accurate. Additionally, the total porosity of 46.3% measured using TG is comparable with the average total porosity of the top section of the specimens (ϕ_{total} = 45.4%) given in Table 3.2 (see Section 3.4).

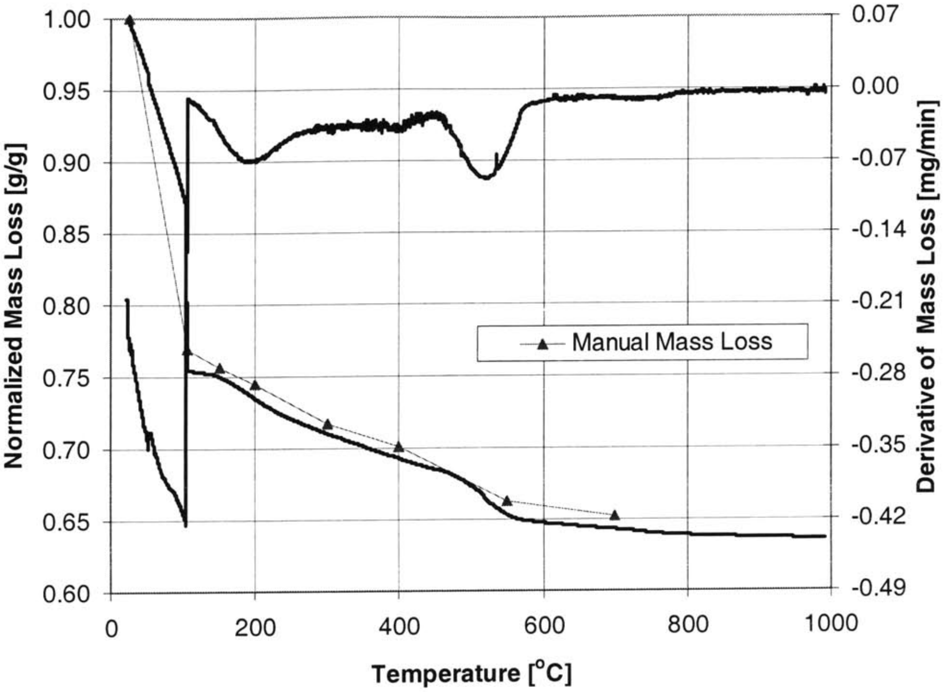

Figure 4-2: Comparison of TG results and normalized manual mass loss measurements.

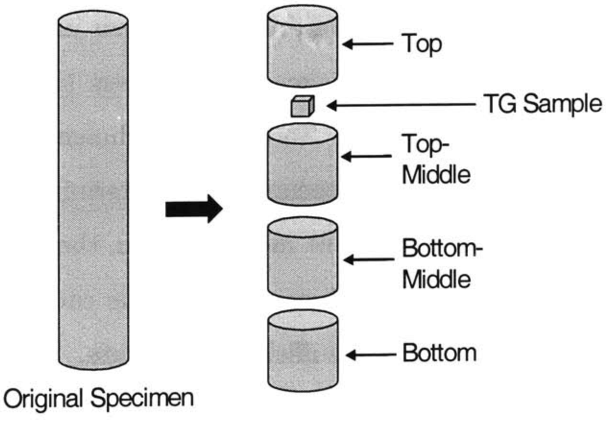

Figure 4-3: Location of TG sample cut from original specimen.

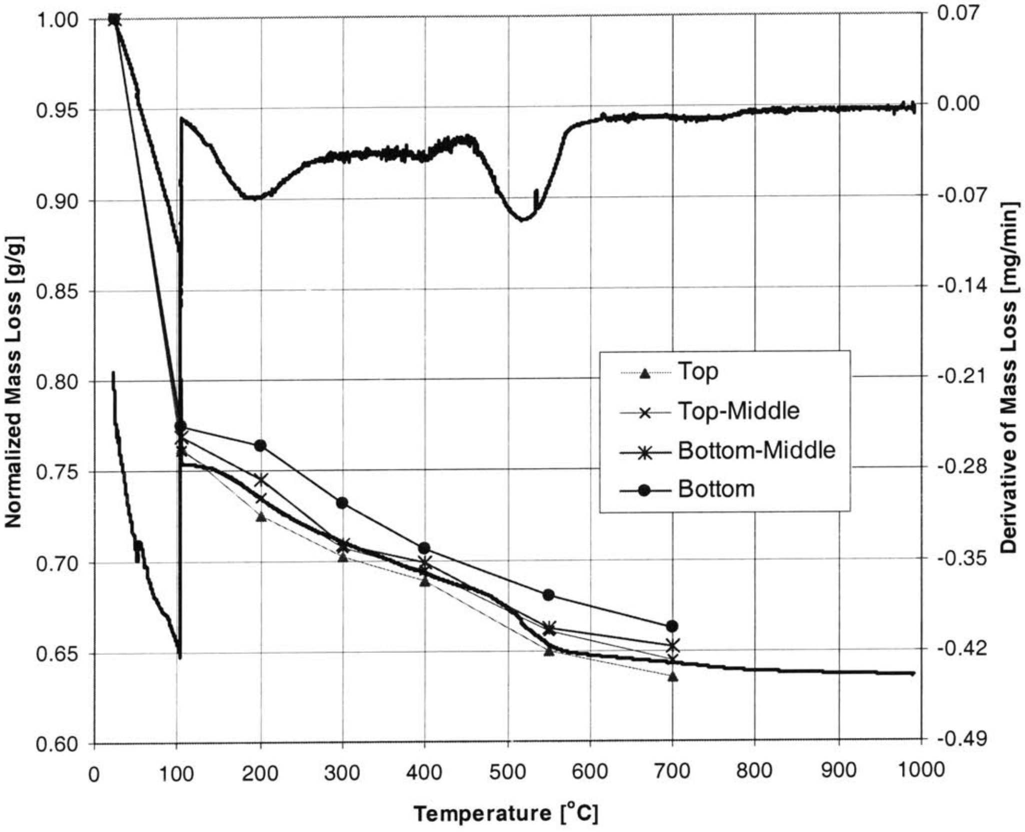

Figure 4-4: Comparison of TG results and normalized manual mass loss measurements of each section of the original specimen.

4.2 Thermal Effects on Volume and Density

The change in volume of cement paste due to high temperature exposure is of interest for correlation with the results of thermogravimetry (change in mass). To determine volume change, cylindrical samples were dimensioned immediately after removal from the furnace. The diameter was measured at three different angles in the middle and at each end of each specimen (a total of 9 measurements), from which an average diameter was determined. The length was also measured three times and results were averaged. All measurements were made to an accuracy of 0.01 mm. Using these measurements, the relative volume change after exposure to each temperature was determined. The volume change results were then used in conjunction with mass loss results to determine the change in density due to high temperature exposure. Relative changes in volume, density, and mass are plotted together in Figure 4-5. Additionally, since all mass loss is assumed to be due to loss of pore water up to 105°C, the relative changes of these properties above 105°C are of interest and are plotted in Figure 4-6.

It is interesting to note that the rate of volumetric shrinkage is approximately constant up to 550°C, but the volume then remains almost constant between 550°C and 700°C. Accordingly, the density decreases significantly between 550°C and 700°C, even though the rate of mass loss decreases in this range. Comparison of this result with MIP measurements is useful to determine the evolution of the microstructure which causes this decrease in density. Komonen *et al.* [35] used MIP to find that the dominant pore diameter in cement paste increases from less than 100nm at 520°C, to ~150 nm at 600°C, and to ~250 nm at 700°C. Meanwhile, the total pore volume increases significantly (5%) between 520°C and 600°C, but then remains almost constant between 600°C and 700°C. In summary, between 600°C and 700°C the rate of mass loss decreases, the rate of density loss increases, the dominant pore diameter increases, and the total pore volume remains relatively constant. Clearly, the pore structure is coarsening more than would be expected from the weight loss measurements. Therefore, it seems logical to conclude that the solid phases which include the gel porosities are densifying, causing an increase in the larger pores, or capillary porosity. At this juncture this is only a preliminary conclusion which will be further discussed using the results of microscopic investigations (see Chapter 6).

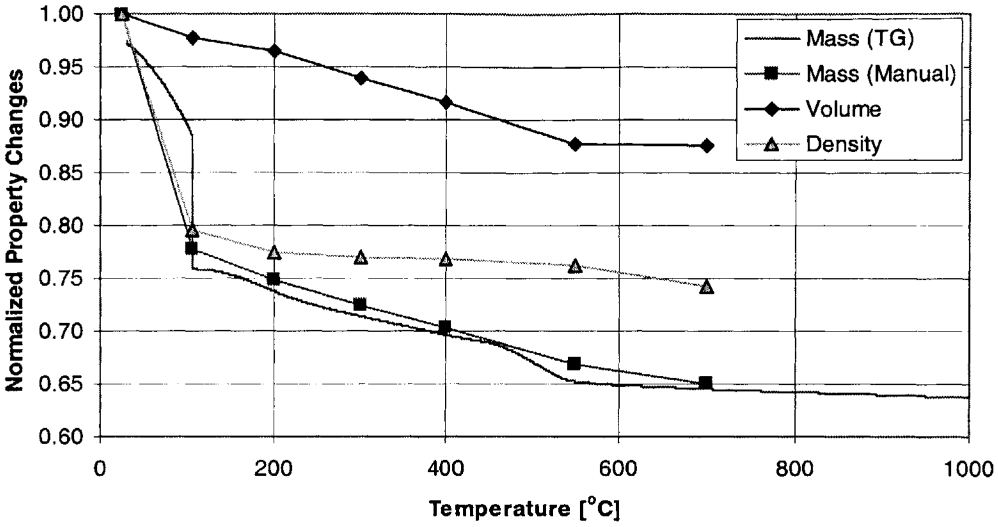

Figure 4-5: Change in mass, density, and volume normalized to 25°C.

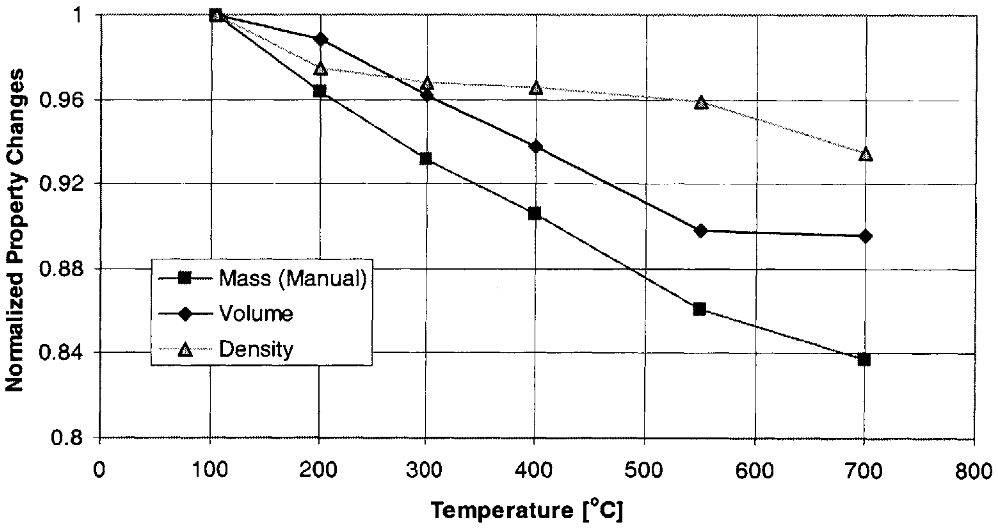

Figure 4-6: Change in mass, density, and volume normalized to 105°C.

4.3 Uniaxial Compression

Uniaxial compression testing is the most common test method used on concrete. It is relatively inexpensive and easy to perform and is important because it measures the compressive strength of concrete, upon which most design codes are based. Additionally, the static modulus of elasticity can also be determined using uniaxial compressive testing, further increasing the benefits of this inexpensive testing method. For these reasons, the effects of high temperature exposure on concrete were initially studied using this testing method.

Research studies regarding the effects of high temperature exposure on both the compressive strength and the static modulus of elasticity of cement paste were already discussed in Section 2.3.3. The results of the current investigation will be compared with existing results to verify that the heating procedure yields a material that is consistent with materials used in other research studies.

4.3.1 Methods

Uniaxial compression is a relatively simple test but it is very sensitive to variations in procedure and must therefore be carried out according to strict standards in order for results to be comparable with existing results in the literature. The standard procedure is defined in ASTM 39 [3]. Generally, cylindrical specimens are compressed between two bearing blocks by increasing the compressive load (load controlled) or increasing the compressive displacement (displacement controlled) until failure occurs. During testing, compressive displacement and load are recorded and the maximum load resisted by the material is divided by the cross-sectional area to determine the compressive strength. Specific factors which affect the measured compressive strength are:

- **End Conditions:** The primary factor which influences the results of uniaxial compression testing is the effect of end conditions. Specimen ends need to be smooth to avoid stress concentrations that might be caused by uneven surfaces. In this investigation, specimen ends were sanded smooth to reduce these stress concentrations as described in Section 3.2.2. Additionally, it is necessary for the specimen ends to be cut perpendicular to the center line of the specimen to avoid stress concentrations caused by uneven contact

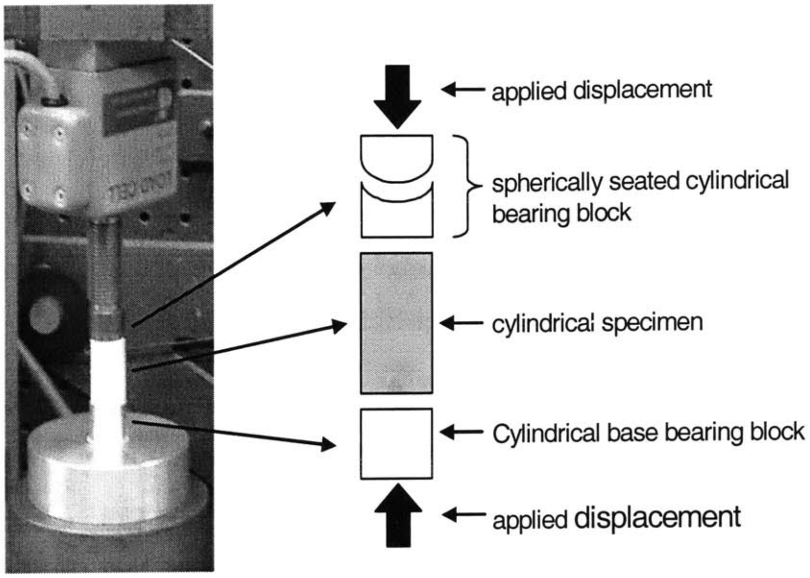

Figure 4-7: Schematic drawing and image of setup for uniaxial compression testing.

with the bearing blocks. Care was taken to provide perpendicular ends when specimens were cut with the diamond saw. Additionally, a spherically seated bearing block was also used to bear on the upper specimen surface so that full contact with the specimen surface was ensured (see Fig. 4-7).

- **Loading Rate:** Generally, the measured compressive strength of concrete has been found to increase with increased loading rates. The standard range of loading rates is defined as between 0.15-0.35 MPa/s. Although displacement controlled testing was used in this investigation, loading rates were maintained within the defined standard range, which should minimize rate effects on the compressive strength.

- **Length-to-Diameter Ratio:** During compression, frictional forces at the ends of the specimen resist expansion that would occur due to Poisson's effects, therefore creating a lateral confinement at the ends of specimens. This confinement is greatest right at the ends of the specimen and slowly dissipates to zero at approximately $\sqrt{\frac{3}{2}}d$ from the specimen ends, where d is the diameter of the specimen [3]. Beyond this confinement zone at each end, a state of true uniaxial compression is achieved. As a result, a standard length-to-diameter (l/d) ratio is necessary to establish a consistent 'confinement effect' so that results are comparable between laboratories. Standard cylinders are defined as having a l/d ratio of 2.0 [3] even though this ratio still produces some lateral confinement within the specimen due to the Poisson's effects previously described. Smaller l/d ratios have been found to increase lateral confinement and therefore cause larger measured compressive strengths, while larger l/d ratios have the opposite effect. It has been found that results are within an acceptable range of 5% for l/d ratios between 1.5 and 2.5. In this investigation, l/d ratios were kept within a range of 2.0 to 2.5.

- **Moisture Conditions:** Drying concrete causes an increase in strength that is not well understood. Explanations include a change in the structure of C-S-H during drying and/or a change in the internal friction and cohesion, causing particles to effectively 'slip' by each other less easily. As a result, ASTM C39 [3] specifies that concrete be maintained and tested in its saturated state. However, this is not possible for exploration of high temperature effects because resaturation would cause rehydration of C-S-H, rendering useless results. Therefore, dry specimens will be tested as is standard for high temperature investigations of compressive strength [19].

- **Cross Sectional Area:** The direct result of the uniaxial compressive test is the maximum load resisted by the material, but this maximum load needs to be divided by the cross sectional area in order to calculate the compressive strength. The cross-sectional area can be accurately measured before testing, but it will increase when compression is applied due to Poisson's effects. In this investigation, a common approximation assuming constant volume of the specimen was used, which relates the corrected area to the initial area through the following equation:

$$A_{corrected} = \frac{A_{initial}}{1 - (\varepsilon_{axial}/100)} \tag{4.1}$$

  where ε_{axial} is the compressive strain parallel to the direction of loading.

Specimens were tested immediately after removal from the furnace or desiccator to prevent rehydration effects from occurring. Six specimens were tested at each temperature and results were averaged.

Temperature [°C]	Compressive Strength [MPa]	Normalized Compressive Strength [%]
25	49.9 ± 4.2	100
105	73.4 ± 6.9	147
200	65.5 ± 5.4	131
300	57.0 ± 5.7	114
400	46.2 ± 4.2	93
550	36.9 ± 6.3	74
700	16.4 ± 1.8	33

Table 4.1: Residual compressive strength after heating to various temperatures. Average values and standard deviations are from six specimens at each temperature.

4.3.2 Results

Average residual compressive strengths after exposure to various temperatures are shown in Table 4.1 and Figure 4-8. Drying (exposure to a temperature of 105°C) caused a significant increase (42%) in compressive strength, as was expected, beyond which compressive strengths decreased continuously. Compressive strengths remained higher than the initial compressive strength until temperature exposures between 300-400°C. An increase in the rate at which the compressive strength decreases is noticeable beyond 550°C, and the ultimate residual compressive strength after exposure to 700°C was found to be 16.4 MPa (33% of the initial strength).

Observation of failed unheated specimens (saturated) clearly indicated that end effects were present. Undamaged cones at specimen ends are characteristic of lateral confinement and were easily visible (see Fig. 4-9). Observation during failure indicated that specimens heated up to 400°C failed in a more explosive manner than saturated specimens, indicating an increase in brittleness of the material. Because of this explosive failure, evidence of end effects was rarely seen. At higher temperatures (550°C and 700°C), failure became less explosive and was dominated by successive cracking resulting in a 'crumbling' type of failure.

4.3.3 Discussion

Comparison indicates that the normalized compressive strength results of this investigation are very similar to the results of Dias *et al.* [18] presented in Section 2.3.3 (see Fig. 4-10). It is noteworthy that the drop in compressive strength above ~400°C indicated by the results of

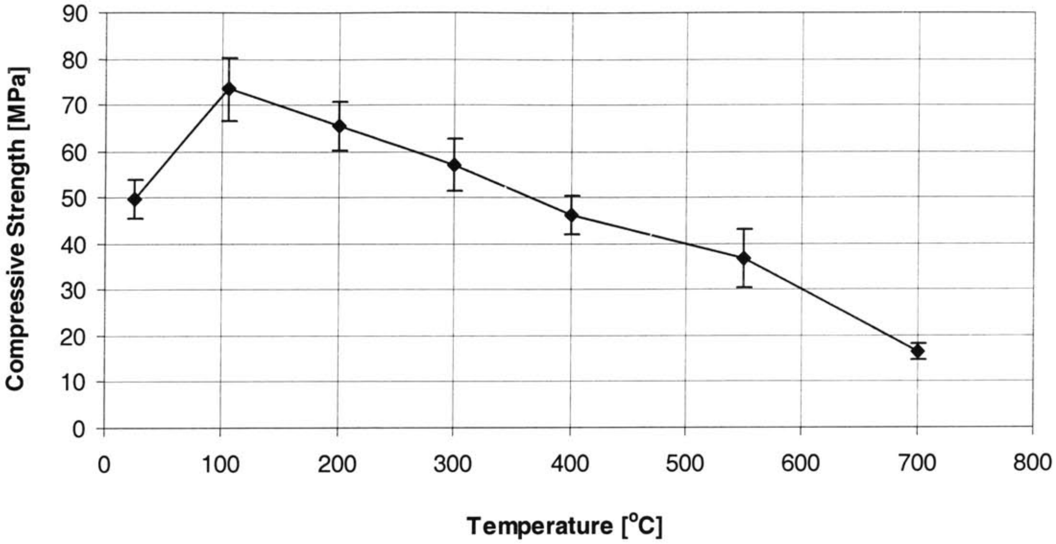

Figure 4-8: Average residual compressive strength after exposure to various temperatures.

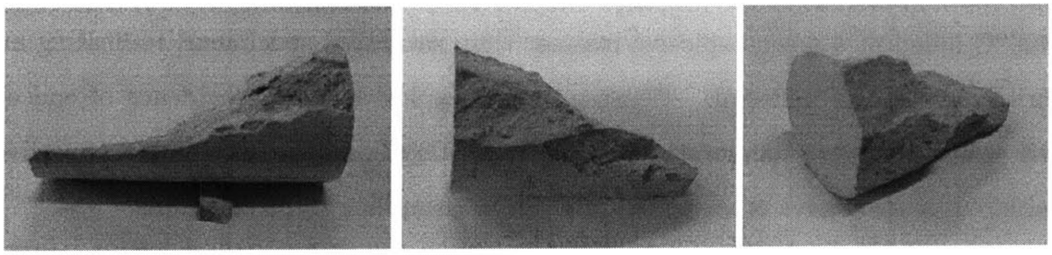

Figure 4-9: Failed uniaxial specimens indicating the presence of lateral confinement at specimen ends.

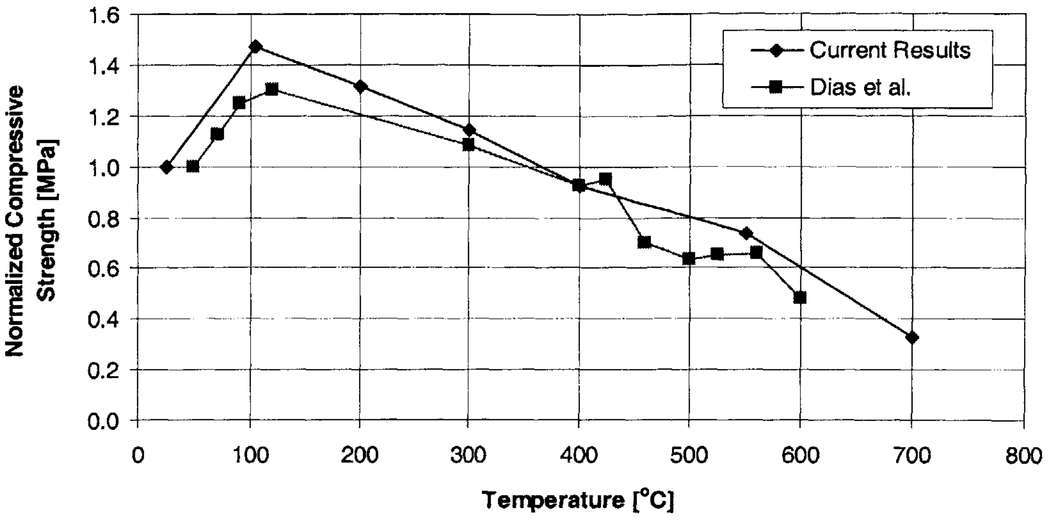

Figure 4-10: Comparison of uniaxial compressive strength results with the results of Dias *et al.* [18].

Dias *et al.* was not observed in this investigation because larger temperature increments were used. Besides this minor difference, the similarity of results verifies the general behavior of residual compressive strength after exposure to high temperature summarized in Table 2.7.

4.4 Resonant Frequency

Resonant frequency testing is one of two primary non-destructive techniques used to measure the dynamic modulus of elasticity of cementitious materials. The other technique is Ultrasonic Pulse Velocity (UPV) testing which was not used in this study, but the results of which will be utilized for comparison. Both methods have the benefit of leaving the sample intact which is particularly useful for measuring progressive changes in a material due to various environmental conditions such as temperature exposure. The standard test method for resonant frequency testing is defined in ASTM C215 [4].

Resonant frequency testing has been successfully used to measure the fundamental transverse, longitudinal, and torsional resonant frequencies of concrete cylinders or prisms for the purpose of calculating the dynamic modulus of elasticity. Generally, this is done using either the forced resonance method or the impact resonance method. Both methods impose a vibration on the specimen and measure the response in order to determine the resonant frequency. In this study, the resonance impact method was used and the fundamental longitudinal resonant frequency was measured. After the resonant frequency is determined, the dynamic modulus of elasticity can be calculated.

Longitudinal vibrations in a cylindrical rod result from compressive-dilational waves involving particle motions parallel to the axis of the rod. The following classical wave equation for longitudinal waves in a rod can be easily derived:

$$\frac{\partial^2 u}{\partial x^2} = \frac{1}{{C_L}^2}\frac{\partial^2 u}{\partial t^2} \tag{4.2}$$

where u is the displacement in the axial direction (x), t is the time, and C_L is the longitudinal wave velocity as defined by the following equation:

$$C_L = \sqrt{\frac{E}{\rho}} \tag{4.3}$$

where E is the modulus of elasticity and ρ is the density of the cylindrical rod. The classical wave equation has a general solution of the form:

$$u = F_1\left(t + \frac{x}{C_L}\right) + F_2\left(t - \frac{x}{C_L}\right) \tag{4.4}$$

where F_1 and F_2 are arbitrary functions. Derivation of the special case of longitudinal standing waves in a rod can be made which correspond to the resonant frequencies of the rod. The resulting resonant frequency solutions, however, are dependent on the end conditions. In the impact resonance method used in this study, both ends of the rod are free to vibrate, which yields the following set of resonant frequency solutions:

$$f_j = \frac{jC_L}{2L}; \quad j = 1, 2, 3, \ldots \tag{4.5}$$

where L is the length of the rod and j represents the longitudinal mode of vibration. Combining Eqs. (4.3) and (4.5), the relationship between the dynamic modulus of elasticity and the fundamental resonant frequency (f_1) is found:

$$E = 4L^2 {f_1}^2 \rho \tag{4.6}$$

For cylindrical specimens, as used in this study, this relationships corresponds to the following equation given in the ASTM standard [4]:

$$Dynamic\ E = 5.093 \left(\frac{L}{d^2} \right) M \left(f_1 \right)^2 \tag{4.7}$$

where M corresponds to the mass of the specimen and d corresponds to the diameter.

4.4.1 Methods

All resonant frequency tests were performed in the non-destructive evaluation laboratory of W.R. Grace in Cambridge, MA. Precise guidelines for measuring the fundamental longitudinal resonant frequency using the impact resonance method are given in ASTM C215 [4], but the general procedure used will now be described. In order to allow the specimen to vibrate freely in the fundamental mode, the specimen must be supported at locations of zero vibration, called nodes. The fundamental longitudinal mode has only one node located at the midpoint of the specimen, where it was supported (see Fig. 4-11). The specimen was impacted perpendicular to one end and the response was recorded using an accelerometer at the other end. Petroleum jelly was used between the accelerometer and the specimen to ensure that contact was maintained at all times resulting in clearer resonant frequency peaks. The acceleration signal was then processed by a digital Fourier transform algorithm in a frequency analyzer to convert the signal to the frequency domain. Using the resulting frequency distribution, the resonant peak was located and the corresponding resonant frequency recorded (25,300 Hz in Fig. 4-11). Each specimen was tested until 3-5 resonant frequency measurements were obtained. The average resonant frequency value was used to calculate the dynamic modulus of elasticity using Eq. (4.6).

All specimens were tested in their saturated state before heating to the various temperatures of investigation, and then again after heating. Six samples (5 standard, 1 short) were tested at each temperature of investigation and results were averaged. An aluminum sample was also

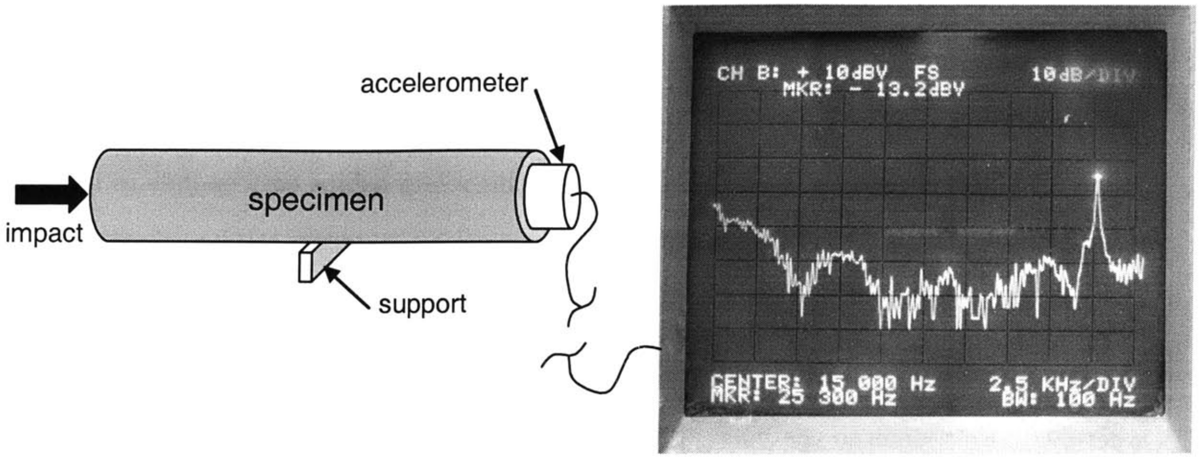

Figure 4-11: Schematic diagram of impact resonance test used to measure the fundamental longitudinal resonant frequency.

tested during each test session to verify that the testing procedure was consistent.

4.4.2 Results

The aluminum sample tested yielded the same resonant frequency during all test sessions, corresponding to a dynamic modulus of elasticity of 69.1 GPa. Reported moduli of elasticity for aluminum generally range from 69-71 GPa, indicating that the testing procedure used was quite accurate. The average dynamic modulus of elasticity of all 36 saturated samples was 19.5 GPa with a standard deviation of 0.51 GPa. Resonant frequency peaks were distinctly visible in the frequency distribution plots produced by the frequency analyzer. The effect of high temperature exposure on the dynamic modulus of elasticity can be seen in Figure 4-12, which shows the results of all temperatures investigated. These results show a drastic drop in modulus of elasticity after drying (105^{o}C) which was unexpected and needs to be further investigated. Resonant frequency peaks were less distinguishable and less reproducible on the frequency distribution plots of all heated samples. After heating to temperatures beyond 105^{o}C, the elastic modulus decreased steadily with exposure to higher temperatures reaching an ultimate minimum value of 2.25 GPa ($\sim$12% of the initial value) after exposure to 700^{o}C. The length of the samples was found to have no significant effect on the results.

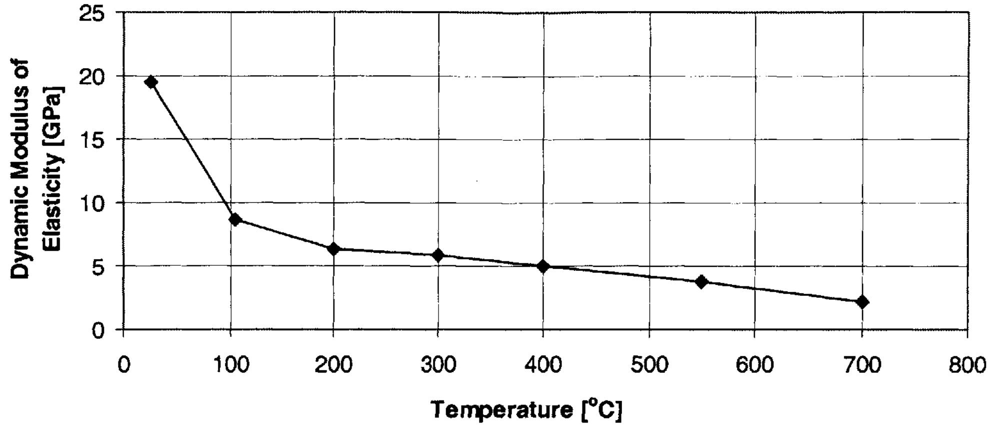

Figure 4-12: Average residual dynamic modulus of elasticity after exposure to various temperatures.

4.4.3 Discussion

Normalized dynamic modulus of elasticity results are compared with the results of Dias *et al.* [18] in Figure 4-13. Clearly, the drop in elasticity after drying observed in this investigation was not nearly as drastic in the results of Dias *et al.* The best explanation of this is the testing method used. Dias *et al.* used UPV testing which has been noted to be more effective than resonant frequency testing for investigation of the effects of high temperature on cementitious materials [20]. Resonant frequency testing is more sensitive to local damage [20] [37] or physical flaws [50] which lead to an underestimation of the actual modulus of elasticity of the bulk material. Perhaps more critical, however, are the shortcomings of the impact resonance method itself. This method relies on the vibration response from one single impact to determine the resonant frequency of a sample. This works quite well for solid (non-porous) or saturated porous materials, but is less effective in more discontinuous or porous materials such as dried cement paste. In porous materials, the longitudinal compressive-dilational waves are more dispersive and therefore yield blurred frequency distributions leading to uncertain results. On the other hand, both UPV and the forced resonance method use continuous forcing techniques which allow vibrations to be controlled and recorded more precisely, decreasing dispersal effects and leading to more accurate results.

Despite the drastic initial drop in modulus of elasticity, the relative changes in elasticity after drying are worth investigating. Figure 4-14 displays the dynamic modulus of elasticity results of this study normalized to 105°C and the results of Dias *et al.* normalized to 90°C for comparison. The decrease in elasticity in both investigation is relatively consistent, although the results of Dias *et al.* are more comprehensive because smaller temperature increments were used.

Based on this discussion, the initial saturated modulus of elasticity (19.5 GPa) seems to be accurate. Masse *et al.* [37] found the elastic modulus of saturated cement paste ($w/c = 0.5$, cured for 28 days) to be ~18.5 GPa, which corresponds well with current results. However, results from samples exposed to higher temperatures appear to underestimate actual values. Because of this, the normalized results of Dias *et al.* will be used for comparison with microscopic investigations in Chapter 5.

4.5 Visual Observation

Specimen surfaces were observed visually after heating to determine various qualitative effects of high temperature exposure that could not be quantified experimentally. All observation were made with the naked eye or a low power microscope. The distinguishable qualitative effects were:

- Color change: Saturated samples were gray in color, and exposure to temperatures up to 400°C did not cause any significant color change. However, samples exposed to 550°C and 700°C were significantly lighter in color, still grayish but almost white.

- Cracking: The most noticeable visual effect of high temperature exposure was cracking. Generally, cracking increased with the exposure temperature (see Fig. 4-15). After exposure to 105°C, very little cracking was visible. After exposure to 200°C, 300°C, and 400°C, thin cracks were visible but not abundant, with the frequency and size of cracks increasing slightly with exposure temperature. However, exposure to 550°C and 700°C resulted in a significant increase in crack abundance, connectivity and size. Especially after exposure to 700°C, cracks were thicker and easily visible with the naked eye.

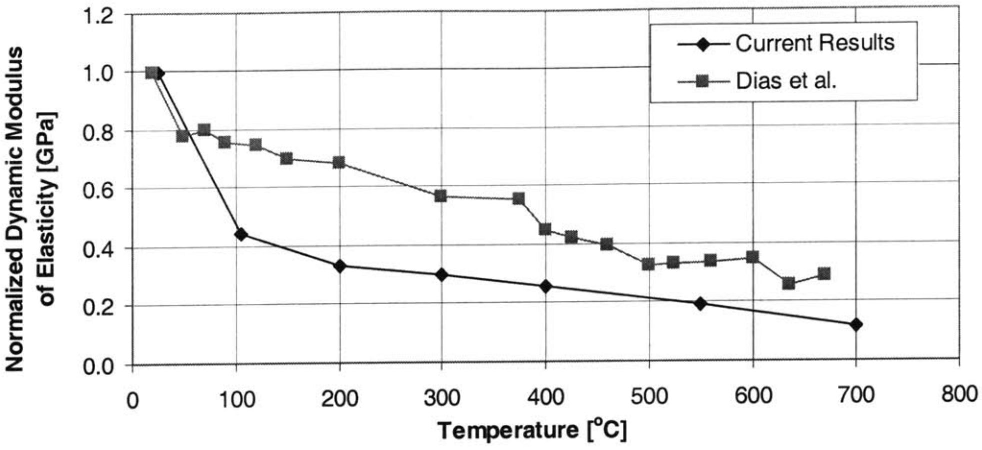

Figure 4-13: Comparison of dynamic modulus of elasticity results with the results of Dias *et al.* [18].

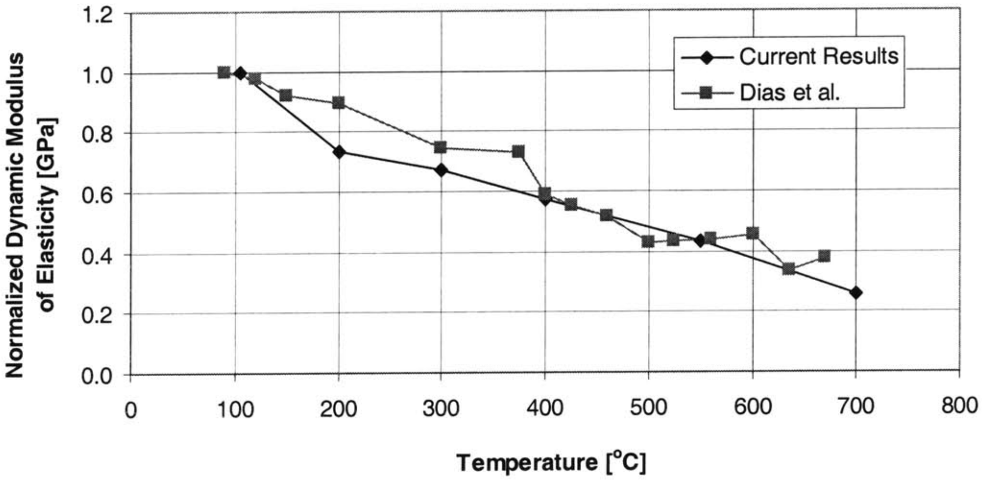

Figure 4-14: Comparison of relative change in the dynamic modulus of elasticity after drying with the results of Dias *et al.* [18].

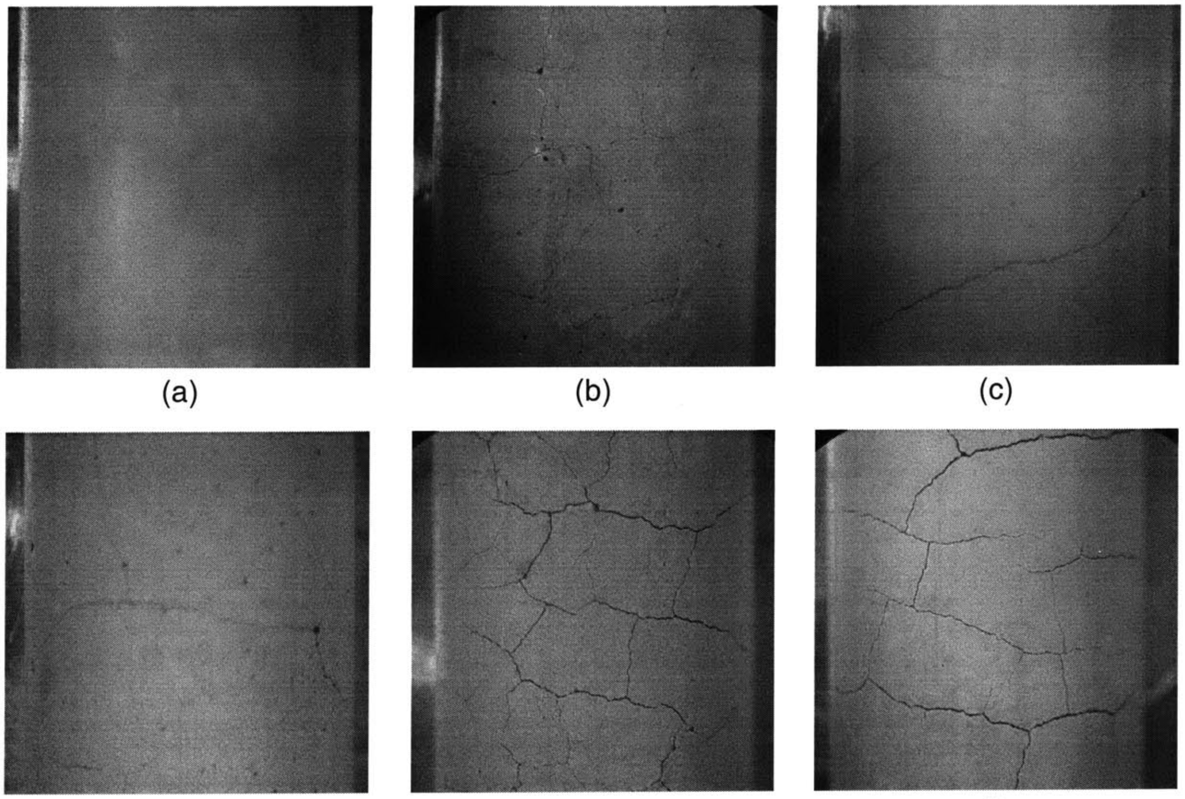
(a) (b) (c) (d) (e) (f)

Figure 4-15: Side view of ~11.5 mm diameter cylindrical samples after exposure to (a) 105°C, (b) 200°C, (c) 300°C, (d) 400°C, (e) 550°C, and (f) 700°C.

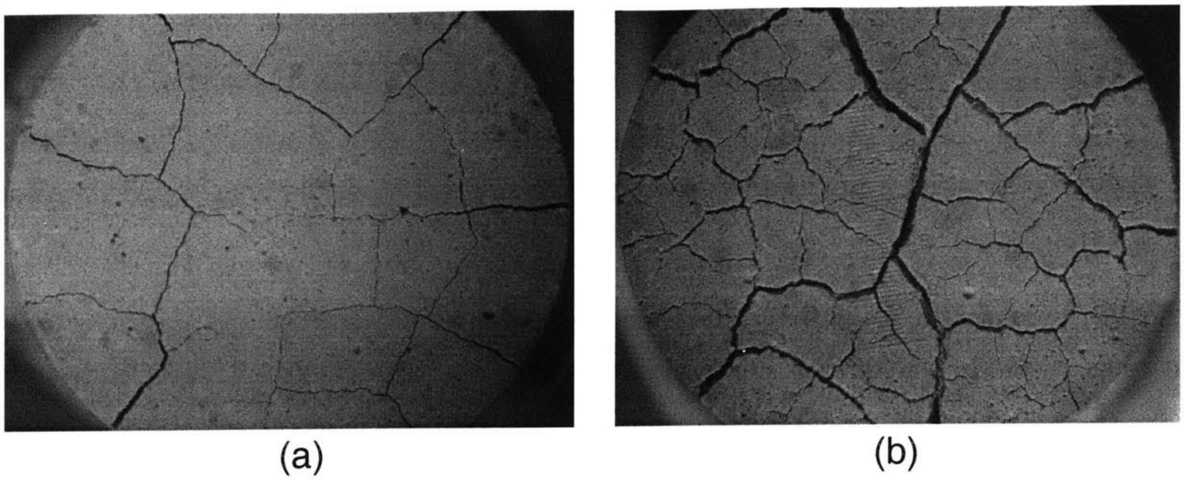
(a) (b)

Figure 4-16: Surface images of samples after exposure to 550^oC and (a) storage in a desiccator, (b) exposure to atmospheric moisture.

- Rehydration: After surface indentation testing was conducted, some samples were left exposed to atmospheric conditions (not placed back in the desiccator), and then observed after several days. Samples exposed to temperatures up to 400^oC did not change significantly, but the number and size of the cracks in samples exposed to 550^oC and 700^oC increased considerably (see Fig. 4-16). This observation is clearly a result of the rehydration of CaO to form CH, which is accompanied by a 44% increase in volume [43]. Because CH dehydrates from 380-580^oC, the majority of CH dehydration occurred in samples exposed to 550^oC and 700^oC. Accordingly, exposure to atmospheric moisture caused the re-formation of CH, noticeable by an increase in cracking due to the large volume change of the CH phase. This observation verifies the importance of storing the heated specimens in a desiccator at all times because rehydration of CH significantly changes the material microstructure. Similarly, although the rehydration of C-S-H is not visually noticeable because it is not accompanied by such a large change in volume, it still occurs and changes the material in an undesirable fashion.

4.6 Summary and Conclusions of Macroscopic Investigations

The primary purpose of this chapter was to verify existing results in the literature. However, at the same time, a better understanding of factors that affect the state of the material, and therefore the experimental results, was obtained. The main contributions of each investigation method were:

- **Thermogravimetry:** TG results confirmed the temperatures of primary C-S-H dehydration (105-300°C), secondary C-S-H dehydration (650-800°C), and CH dehydration (400-600°C). Comparison with manual mass loss measurements also allowed the conclusion that heating procedures were successful (i.e. heating rates and times were sufficient and significant rehydration during cooling did not occur).
- **Volume and Density Measurements:** After drying (heating to 105°C), mass and volume decreased steadily up to 400°C, leading to a slight steady decrease of density. However, between 550°C and 700°C the volume remained constant causing a large decrease in density. This corresponds with the drastic increase in mean pore diameter and total pore volume shown by MIP measurements in the same temperature range.
- **Uniaxial Compression:** Results confirmed the increase in compressive strength during drying and compared remarkably well with the results of previous investigations. This showed that normalized compressive strength results are independent of the w/c ratio.
- **Resonant Frequency:** The impact resonance method is not well suited for dry, porous materials. Because of this, curing time, which defines the volume of the capillary porosity, plays an important role in RF testing. However, normalized results showed good agreement with the results of previous investigations.
- **Visual Observation:** Color change and increased cracking occurred after exposure to temperatures of 550°C and above. Additionally, the effects of rehydration after cooling had a severe effect on the material state after exposure to similar temperatures.

This chapter verified that the material tested yielded results similar to the results of previous investigations. With this established, the results of microscopic investigations can now be compared with new and existing results with confidence.

Chapter 5

Microindentation

In this study, microscopic investigation includes both microindentation and nanoindentation. Microindentation was used to access the properties of bulk cement paste ('Level II') and nanoindentation was used to access the properties of the different phases that make up cement paste ('Level I'). The basic procedure and analysis are the same for both investigation techniques, and will be summarized at the beginning of this chapter on microindentation. However, because microindentation and nanoindentation were executed using different equipment and at different length scales, specific testing and analysis methods of each experimental investigation need to be addressed independently. The methods specific to microindentation will be addressed in this chapter, and specific nanoindentation methods will be presented in Chapter 6. Finally, the results of microindentation will be presented and discussed at the end of this chapter.

5.1 Basics of Indentation Testing

Indentation testing has been performed for quite some time, but significant advances in recent years have made the testing method more efficient, effective, and powerful. This is largely due to the development of improved equipment which has the capability of continuously recording the force and penetration depth at the micronewton and submicron scale, respectively. Traditionally, indentation has been primarily used to investigate homogeneous materials such as metals and polymers, but recently developed analytical techniques have allowed successful determination of the mechanical properties of heterogenous materials as well [12].

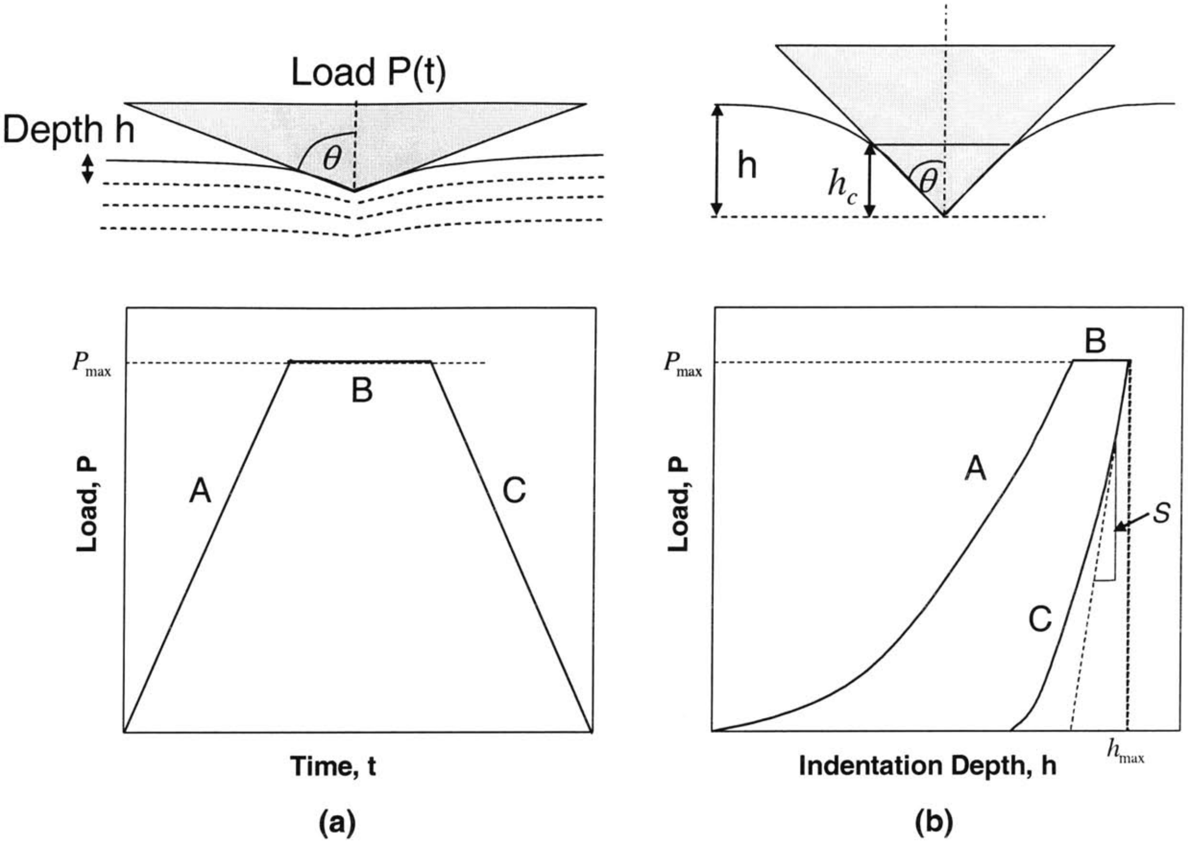

Figure 5-1: Typical indentation (a) loading function and (b) load-displacement response curve [13].

5.1.1 Experimental Procedure

An indenter with known geometry and mechanical properties is pushed into the material under investigation until a specified maximum load or depth is reached, then held at the maximum load for a specified time, and then retracted from the material leaving an indentation (see Fig. 5-1(a)). During this indentation, the force and displacement are continuously measured and yield an indentation curve as shown in Figure 5-1(b). The specified depth of the indentation determines the volume of the material being tested, and therefore determines the scale at which the results are applicable. Therefore, in order to access mechanical properties at the submicron scale, indentation depths need to be in the nanometer range, making accurate force and displacement measurement extremely difficult. Force and displacement are typically measured using capacitors which allow load and displacement resolutions of approximately 0.5 μN and 0.2 nm, respectively, depending on the machinery used. In order for such high resolution to be possible, extreme care needs to be taken to limit environmental effects which could cause inaccurate results. As a result, indentation equipment is typically mounted in a sealed chamber to reduce thermal and other environmental effects, and needs to be isolated from vibration.

In this investigation, a Berkovich indenter was used in all experiments. A Berkovich indenter is a three-sided pyramid with an equivalent cone inclusion angle (θ) of 70.3^o (see Fig. 5-1). Interpretation of Berkovich indentation data in order to obtain mechanical properties of materials has been extensively investigated and will now be discussed.

5.1.2 Individual Indentation Analysis

The two mechanical properties most frequently determined from the load-displacement data given by indentation are the indentation modulus, M, and the hardness, H. The hardness is traditionally defined by the following equation:

$$H = \frac{P_{max}}{A_c} \tag{5.1}$$

where P_{max} is the peak load during indentation and A_c is the projected area of contact at the peak load. The peak load can be easily determined from indentation data, but the contact area is more difficult to determine and will be discussed in more detail later.

For a linear elastic isotropic material, the indentation modulus was first investigated by Bulychev *et al.* [9] who showed that the Hertz-type contact solution holds for indentation analysis:

$$S = \frac{dP}{dh} = \frac{2}{\sqrt{\pi}} M \sqrt{A_c} \tag{5.2}$$

where $S = dP/dh$ is the experimentally determined unloading slope, M is the indentation modulus, and A_c is the area of contact at the peak load. Solving Eq. (5.2) for M yields:

$$M = \frac{\sqrt{\pi}}{2} \frac{S}{\sqrt{A_c}} \tag{5.3}$$

The indentation modulus, M, is related to the elastic modulus of the indented material, E, through the following equation:

$$\frac{1}{M} = \frac{(1-\nu^2)}{E} + \frac{(1-\nu_i^2)}{E_i} \tag{5.4}$$

where ν is the Poisson's ratio of the indented material, and E_i and ν_i are the elastic modulus and the Poisson's ratio of the indenter itself. This equation includes the effect of non-rigid indenters on the load-displacement results. However, a diamond indenter is typically used (and was used in this study) for which $E_i = 1,140\ GPa$ and $\nu_i = 0.07$ [31] [41]. Because the elastic modulus of cementitious materials is much lower ($< 50\ GPa$), the indenter will be assumed to be rigid, yielding the following equation for the elastic modulus:

$$E = M\left(1-\nu^2\right) \tag{5.5}$$

Correct determination of the elastic modulus is therefore dependent on the Poisson's ratio, although not extremely dependent because the property is squared in Eq. (5.5). The Poisson's ratio is not measured during indentation but can be taken as ~0.24 for cement pastes at room temperature [12] [22]. Additionally, measurements of the Poisson's ratio after high temperature exposure are rare and somewhat contradictory, but generally do not indicate a strong dependence on temperature [34]. Farage [22] found the Poisson's ratio of cement paste to vary from 0.24 to 0.19 after exposures up to 300^{o}C, which results in only a 2% difference in the modulus of elasticity using Eq. (5.5). Based on this knowledge, the Poisson's ratio will be assumed to be 0.24 for all temperatures, which might cause a slight underestimation of the actual elastic modulus after exposure to high temperatures.

Unloading Slope (S)

It is necessary to determine the unloading slope, S, from the indentation data in order to determine the indentation modulus from Eq. (5.3). The elastic unloading region of the indentation data is typically fit using the following power function:

$$P = b\left(h - h_f\right)^m \tag{5.6}$$

where h_f is the residual indentation depth, and b and m are fitting parameters of the unloading response. For elastic indentation, $h_f = 0$, Sneddon's solution [51] provides the theoretical value of m for the following indenter geometries: $m = 1$ for flat cylindrical indenters, $m = 1.5$ paraboidal indenters, and $m = 2$ for conical indenters. From Eq. (5.6), the initial unloading slope can be directly determined:

$$S = \frac{dP}{dh} = m\,(b)^{\frac{1}{m}}\,(P_{max})^{\frac{m-1}{m}} \tag{5.7}$$

Oliver and Pharr [41] observed that, for a large variety of materials, the value of the fitting parameter m using Berkovich indentation ranges from 1.25 to 1.51, with a mean value of 1.40. This corresponds best with the theoretical value of m for a paraboidal indenter ($m = 1.5$).

Area of Contact (A_c)

Traditionally, the projected contact area, A_c, has been the most difficult parameter to accurately measure. Based on Eqs. (5.1) and (5.3), it is clear that accurate measurement of the contact area is critical to obtain both the hardness and indentation modulus. The hardness is directly proportional to the contact area, making it especially dependent on correct contact area measurement. However, because the elastic modulus is proportional to the square root of the contact area, it is less sensitive to errors in the measurement of the contact area.

Originally, the contact area was determined by measuring the size of the indentation using direct imaging techniques. Optical imaging works well for larger indentations, but lacks the resolution necessary to measure smaller contact areas corresponding to indentation depths in the nanometer range. Other imaging techniques (AFM, TEM, etc.) have been successfully used to measure these smaller contact areas, but they are too time consuming and tedious to use when hundreds of indentations are being analyzed. Because of this, extensive research has been conducted to determine the contact area without the necessity of imaging. The most widely used method of determining the contact area, and the one used in this study, is that of Oliver and Pharr [41]. Assuming that the indenter is rigid, the projected contact area, A_c, can be computed directly as a function of the contact depth, h_c, as follows:

$$A_c = F(h_c) \tag{5.8}$$

where the function F depends only on the geometry of the indenter. For example, for a perfect Berkovich indenter, the area function is:

$$A_c(h_c) = 24.5(h_c)^2 \tag{5.9}$$

However, in reality the indenter geometry changes as the tip becomes blunt due to repeated indentation. Because of this, the area function is calibrated by indenting in a material with known elastic properties (such as fused silica). The area function is fit using the following equation:

$$A_c(h_c) = 24.5(h_c)^2 + C_1(h_c) + C_2(h_c)^{1/2} + C_3(h_c)^{1/4} + C_4(h_c)^{1/8} + ... \tag{5.10}$$

where the constants, C_i, are determined by the calibration.

Now, it is necessary to determine the contact depth, h_c, from the experimental data. To this end, Oliver and Pharr [41] suggested the extension of the relation between elastic contact depth and indentation depth ($h_c/h = 2/\pi$) to elastoplastic indentation:

$$h_c - h_f = \frac{2}{\pi}(h_{max} - h_f) \tag{5.11}$$

where h_{max} is the peak indentation depth. Both h_f and h_{max} can be obtained directly from indentation data, so h_c can be determined and the contact area can be calculated ($A_c = \pi(h_c \tan\theta)^2$ for conical indenters). However, the value of h_f tends to be very sensitivity to surface conditions so its use should be avoided if possible. Because the unloading slope is fit by Eq. (5.6), the following equation applies to conical indenters ($m = 2$) and is useful to avoid the necessity of measuring h_f:

$$h_c - h_f = 2\left(\frac{P_{max}}{S}\right) \tag{5.12}$$

Combining Eqs. (5.11) and (5.12) yields:

$$\frac{h_c}{h_{max}} = 1 - \epsilon\left(\frac{P_{max}}{Sh_{max}}\right); \quad where\ \epsilon = 2\left(1 - \frac{2}{\pi}\right) = 0.73 \tag{5.13}$$

where ϵ is a geometric constant. Oliver and Pharr [41] also determined the value of ϵ using similar arguments for a flat cylindrical indenter ($\epsilon = 1.0$) and a paraboidal indenter ($\epsilon = 0.75$). Based on the experimental results for m previously mentioned, they concluded that the unloading behavior of Berkovich indentation is best described theoretically by a paraboidal indenter geometry, and therefore a geometric constant of $\epsilon = 0.75$ should be used. Consequently, h_c can be calculated from indentation data and the direct measurement of A_c has been successfully avoided.

$M - H$ Scaling Relation

Dimensional analysis can be used to develop a theoretical relationship between the hardness, H, and the indentation modulus, M, for any homogeneous material:

$$M \propto H^{\alpha} \tag{5.14}$$

where α is a function of the equivalent cone angle of the indenter and the method of contact area estimation [15]. Using (5.1) and (5.3), it is readily recognized that M should scale with H according to:

$$M \propto \sqrt{H} \implies \alpha = 0.5 \tag{5.15}$$

Relation (5.15) holds strictly only for indentation in a homogeneous half-space. Any deviation from this relation, therefore, can be attributed to errors in the determination of M and H that could be caused by improper estimation of the contact area, surface roughness, material imperfections (e.g. cracks), heterogeneities of similar length scale to the depth of indentation, etc. The value of α will be used throughout this chapter as a means of evaluating the quality of the indentation data.

5.1.3 Indentation Analysis for Multi-Phase Multi-Scale Composites

The method that was used for determining the mechanical properties of a material using individual indentation data has now been established, but this individual indentation analysis assumes indentation into a homogeneous material. A proper evaluation of the results of indentation in heterogenous composite materials is still necessary.

Separation of Scale

All materials are heterogeneous at some scale, so an evaluation of the scale of heterogeneity relative to the indentation scale is necessary. In order to apply continuum indentation analysis effectively, the characteristic size of heterogeneity, l, must be much smaller than the characteristic size of the material scale under investigation, L, which is determined by the indentation depth. Provided that this 'separation of scale' requirement ($l << L$) is met, continuum indentation analysis can be accurately applied.

The separation of scale requirement ($l << L$) is necessarily fulfilled for materials that are homogeneous down to the atomic scale (e.g. metals, polymers), because indentation depths corresponding to the atomic scale are impossible. However, for highly heterogeneous materials like cement paste, the 'separation of scale' requirement ($l << L$) needs to be addressed with care. For example, the goal of microindentation is to access the material properties of bulk cement paste, which has been defined as 'Level II' of the multiscale microstructure. Cement paste consists of several phases (LD C-S-H, HD C-S-H, CH,...) which can be defined as having a characteristic size, l. The characteristic size of the material under investigation is defined by the indentation depth, h. Therefore, in order to determine the homogenized mechanical properties of cement paste, the microindentation depth h must be much larger than l ($h >> l$).

Alternatively, the mechanical properties of the various phases of a heterogeneous material may be desired. In this case, the characteristic size of the heterogeneity, $\pounds$, must be much *larger* than the characteristic size of the material scale under investigation, L. This allows investigation of a specific phase while preventing influence from the surrounding phases. Now, provided that both 'separation of scale' requirements ($l << L << \pounds$) are met, continuum indentation analysis can be accurately applied and the mechanical properties of the individual phases of a heterogeneous material can be determined. For example, the goal of nanoindentation is to access the mechanical properties of the various phases of cement paste. The phases (LD C-S-H, HD C-S-H, CH,...) of the multiscale microstructure are now defined as having a characteristic size, $\pounds$. Additionally, each phase is heterogeneous and composed of other phases (gel pores, globules) with a characteristic size, l. Again, the characteristic size of the material under investigation is defined by the indentation depth, h. Therefore, in order to determine the mechanical properties of the individual phases, the nanoindentation depth must fit between the two characteristic sizes of heterogeneity ($l << h << \mathcal{L}$).

Grid Indentation

Using the separation of scale requirements discussed above, an indentation depth can be selected for both microindentation and nanoindentation. However, it is necessary to determine if the indentation results confirm that correct indentation depths were selected. One possible method of verifying indentation depths would be to locate and measure the characteristic length of each of the phases of the indented heterogeneous material, and then indent on each located phase to the determined depth. However, in complex heterogeneous materials like cement paste, phases vary in characteristic length and locating individual phases is extremely laborious and difficult. As an alternative, the most effective method of verifying indentation depths is repeated indentation. Repeated indentation is done in the shape of a rectangular grid, which allows surface mapping of the indentation results.

Grid indentation is effective and necessary for both microindentation and nanoindentation. For microindentation, one must verify whether the indentation depth is sufficient to access the homogenized properties of cement paste. If the indentation depth is sufficient, all microindentations should theoretically yield the exact same results. However, because indentation analysis assumes a perfectly flat surface and a perfectly homogeneous material, some variation in results is inevitable. To account for this variation, plotting the frequency distribution of the results provides a means of determining if one single homogenized phase is present at the scale of investigation. For example, Figure 5-2 shows that at greater indentation depths where homogenization has occurred (as is the goal of microindentation) one single peak is present in the frequency distribution. Furthermore, from this frequency distribution, the mean value can be determined to represent the homogenized material.

Grid indentation is also effective for nanoindentation where the phase properties of a heterogeneous material are desired. Again, if the phases of a heterogenous material can be located and indented individually, then phase properties can be directly determined. However, because this is not yet possible, plotting frequency distributions of grid indentations provides a means of determining if the selected nanoindentation depth has successfully accessed individual phases. For example, Figure 5-2 shows that indenting the same material to lesser depths results in

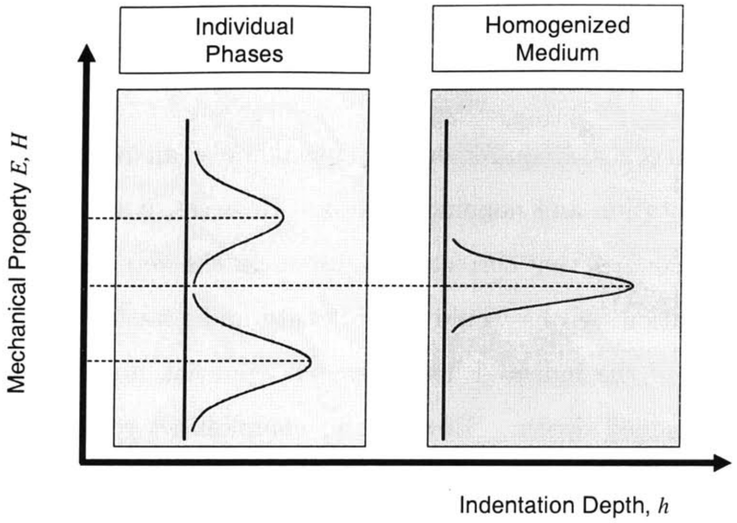

Figure 5-2: Illustration of the homogenization of composite materials by increasing the indentation depth [13].

two (or more) individual phases instead of one, indicating that the selected indentation depth accessed individual phase properties, not homogenized material properties. Furthermore, the mean values of the frequency distribution can be determined to represent the individual phases of the heterogeneous material. Analyzing frequency distributions where several phases are present requires care, and will be discussed further in Chapter 6.

In summary, smaller indentation depths access the properties of the individual phases, whereas larger indentation depths access the homogenized properties of a material. Grid indentation provides an effective method of determining which properties are being accessed.

5.2 Specific Methods of Microindentation

Microindentation tests were conducted using the NanoTest 600 (Micro Materials, Ltd.) indenter in the NanoMechanical Technology Laboratory at MIT. The general method of indentation testing and analysis was presented in the previous section, but the specific methods of microindentation will now be introduced.

5.2.1 Testing Methods

Microindentation samples were prepared as described in Section 3.2.1. Each investigated temperature (25°C, 105°C, 200°C, 300°C, 400°C, 550°C, and 700°C) was tested in the same manner, described by the following specifications:

- **Indentation Depth:** The indentation depth determines the volume of material being tested and therefore defines the length scale, or 'Level' of the multiscale microstructure, that is being investigated. As previously discussed, the goal of microindentation is to access the bulk properties of cement paste ('Level II'), so a proper indentation depth must be selected accordingly. The phases (C-S-H, CH, porosity) of cement paste typically have a characteristic length scale < 1 μm, so an indentation depth of 10 μm was selected to access the homogenized properties of the material.
- **Load Function:** A typical indentation load function is displayed in Figure 5-1(a). Specifically, a loading and unloading rate of 10 mN/s was used, with a dwell time at the maximum load of 30 seconds. During unloading, the load was also held constant for 30 seconds at 10% of the maximum load, from which a thermal drift correction was calculated and applied.
- **Grid Spacing and Size:** An eight by eight indentation grid (64 total indents) was used for each temperature of investigation (see Fig. 5-3). The specified grid spacing was 150 μm yielding a total grid surface area of 1,050 μm x 1,050 μm (approximately 1 mm^2). The grid spacing was chosen to be small enough so the surface could be mapped effectively, but large enough so that each indent was not influenced by its neighbor.
- **Calibration:** Load and depth calibrations and machinery compliance were all measured and applied as suggested by the manufacturer of the equipment used.

5.2.2 Analysis Methods

In order to determine the hardness and elastic modulus from the indentation data, the Oliver and Pharr [41] method (see Section 5.1) was used. Because the indentation depth was selected to determine the homogenized mechanical properties of cement paste, the mean values of the

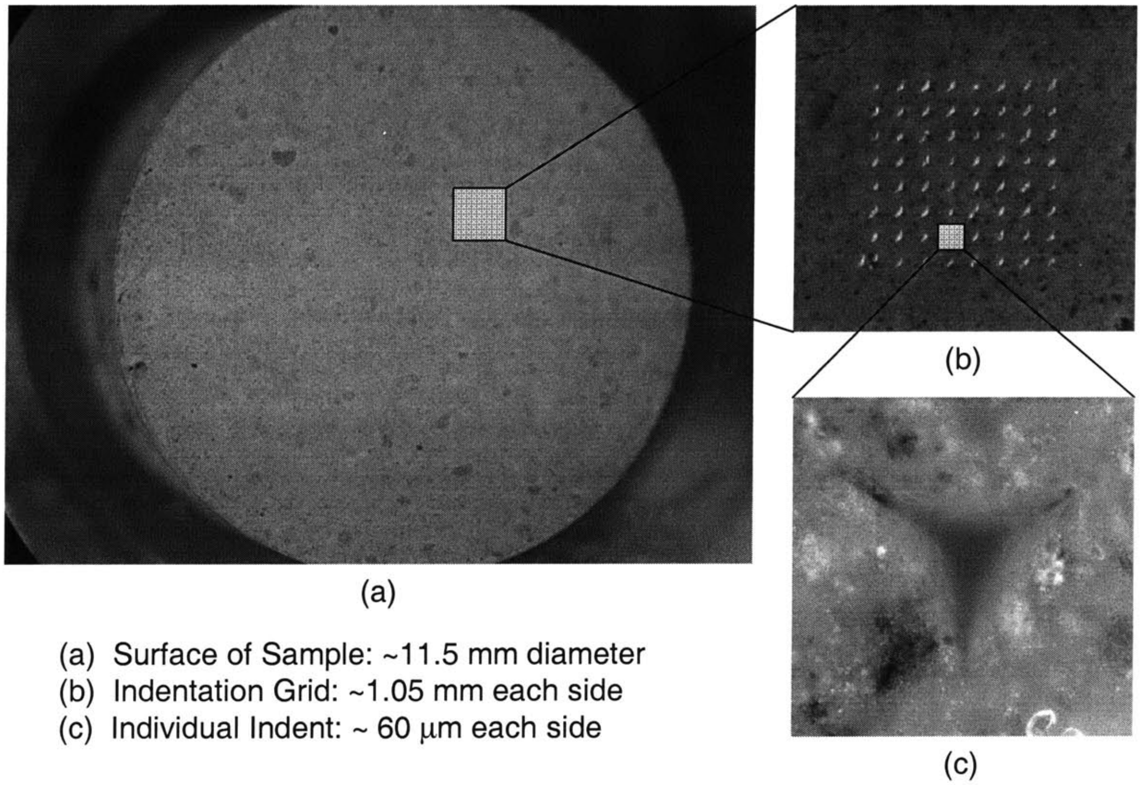

(a) Surface of Sample: ~11.5 mm diameter
(b) Indentation Grid: ~1.05 mm each side
(c) Individual Indent: ~ 60 μm each side

Figure 5-3: Images of (a) the surface of the indented sample, (b) the indentation grid, and (c) an individual indent.

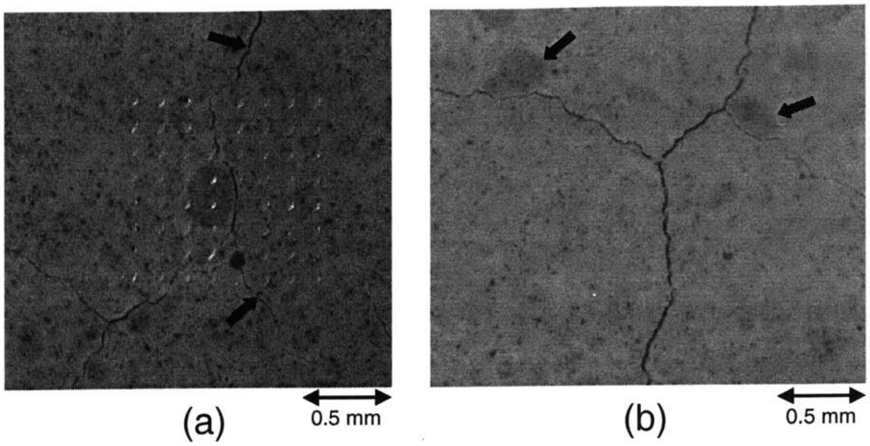

Figure 5-4: Optical images of sample surface after exposure to high temperature: (a) indentation grid (light spots) with cracking and dark areas visible, and (b) crack propagation between and around stiff darker areas.

hardness and elasticity were calculated for each temperature investigated. However, before taking the mean, the validity of each indentation needed to be evaluated. Validity was determined using optical images of the indented area as shown in Figure 5-4(a), which displays the indentation grid of the sample surface after exposure to high temperature. Three imperfections were noticed in the optical images that needed to be dealt with. First, the cracks present in Figure 5-4 clearly create a discontinuous, non-homogeneous material, making continuum indentation analysis invalid. All indentations affected by such cracking were eliminated.

Second, indentation analysis was used to determine that the darker spots in Figure 5-4(a) were much stiffer than the average material, and visual observation indicated that cracks tended to develop around and between these darker areas after exposure to high temperatures (see Fig. 5-4(b)). These darker spots were determined to be a result of pre-hydration: cement paste that was already hydrated due to moisture in the OPC powder prior to mixing. As a result, these dark spots represent a different material because they were essentially hydrated at a very low w/c ratio, which explains their increased stiffness. Again, these dark areas create a heterogeneous material at the scale of investigation, so all indentations affected by these darker areas were eliminated.

Third, large voids (see Fig. 5-4(a)) were sometimes present due to insufficient vibration during casting. These voids were easily located in optical images and all indentations affected by voids were eliminated. The average elastic modulus and hardness were then determined from the indentations that were not influenced by any of these three factors.

5.3 Results

Table 5.1 summarizes the results of microindentation. On average, 25% of indents were eliminated using the optical imaging technique discussed in the previous section. Optical images and their corresponding surface maps are displayed and discussed later in this section. The maximum depth (h_{max}) is basically constant at all temperatures, which was expected because the test was depth controlled. However, the maximum load (P_{max}) needed to achieve the maximum depth increased initially and then decreased after exposure to higher temperatures. A similar trend is noticed in the hardness (H) results, which makes sense because the hardness is directly proportional to the maximum load (see Eq. (5.1)). Obtaining the indentation modulus (M) and the hardness (H) was the primary goal of this investigation and these results will be discussed extensively throughout the remainder of this section. However, the scaling relation parameter α is also of interest. The indentation modulus is plotted with respect to the hardness in Figure 5-5, from which α was determined for all investigated temperatures. The values of α were slightly higher than the expected value of 0.5, indicating that surface roughness or material heterogeneities may have had a slight effect on the results. However, the fact that α remained relatively constant at all temperatures of investigation indicates that changing surface conditions did not cause the observed change in mechanical properties after high temperature exposure. In other words, heating had little effect on the surface condition of the material, so the method of polishing all samples prior to heating was successful.

The average indentation modulus and hardness after exposure to various temperatures are displayed in Figure 5-6 and Figure 5-7, respectively. Generally, the indentation modulus decreased with increased exposure temperature, with a substantial decrease after exposure to temperatures of 550°C and 700°C. However, at 200°C the results show a large decrease in indentation modulus followed by a large increase at 300°C. The average hardness initially increased after drying at 105°C, and decreased thereafter. A substantial decrease was again

Temp.	No. of Indents		h_{max}	P_{max}	M	H	α
[°C]	Total	Used	[μm]	[mN]	[GPa]	[GPa]	
25	64	55	10.57 ± 0.12	417 ± 92	16.5 ± 2.6	0.162 ± 0.035	0.63
105	64	42	10.42 ± 0.10	572 ± 121	15.6 ± 2.9	0.237 ± 0.051	0.79
200	64	46	10.44 ± 0.09	442 ± 74	11.3 ± 1.3	0.184 ± 0.032	0.61
300	64	47	10.30 ± 0.09	537 ± 118	13.2 ± 2.2	0.231 ± 0.054	0.68
400	64	42	10.26 ± 0.06	495 ± 94	12.6 ± 1.6	0.215 ± 0.044	0.56
550	64	51	10.31 ± 0.12	318 ± 65	7.97 ± 1.0	0.136 ± 0.028	0.61
700	64	54	10.27 ± 0.09	187 ± 35	4.83 ± 0.67	0.081 ± 0.016	0.62

Table 5.1: Summary of the results of microindentation.

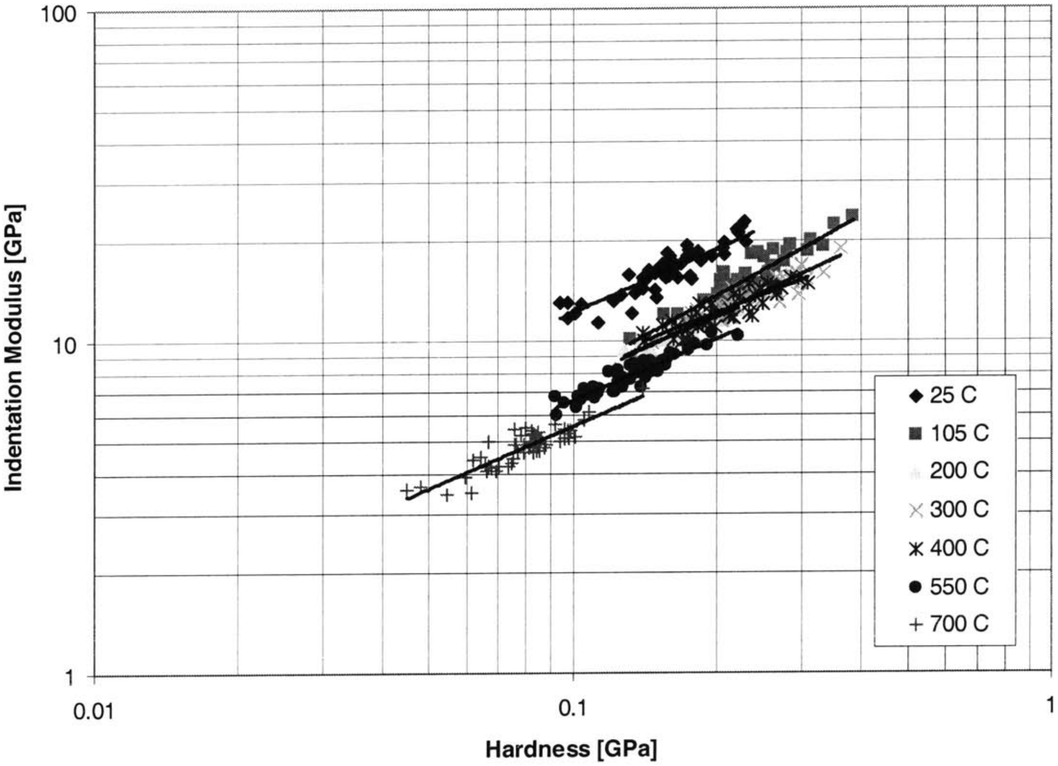

Figure 5-5: Microindentation results: indentation modulus versus hardness for all indentations at all temperatures of investigation.

noticed after exposure to 550°C and 700°C. Also, a large decrease was again noticed at 200°C followed by a large increase at 300°C.

Figure 5-5 also nicely displays the trend in hardness and indentation modulus with respect to temperature. Clearly, the hardness initially increases and then steadily decreases with increased temperature exposure, while the indentation modulus steadily decreases with temperature exposure throughout all temperatures of investigation.

Elasticity Surface Maps

Surface mapping provided a visual spatial distribution of the indentation modulus. Surface maps were critical to this investigation because they provided a means of linking visual observations (cracking, color, voids) with the results of microindentation analysis (indentation modulus). This link allowed a determination of the influence of heterogeneities (cracking, voids, dark areas) on the results in order to eliminate invalid data. Indentation modulus surface maps and their corresponding surface images are displayed in Figures 5-8 and 5-9.

Frequency Distributions

The indentation modulus frequency distributions of all temperatures investigated are displayed in Figure 5-10. All distributions contain one dominant distinguishable peak, indicating that the results represent homogenized mechanical properties (see Fig. 5-2). Gaussian distributions can be fit to each frequency distribution to further verify that the results apply to a homogenized material. For example, Figure 5-11 demonstrates that a Gaussian distribution fits the saturated (25°C) indentation data quite well.

5.4 Discussion

Generally, the distinguishable trends in the microindentation results presented in the previous section compare well with the summary of existing knowledge in Table 2.7. A slow steady decrease in the indentation modulus up to 400°C was expected, as were the large decreases in indentation modulus at 550°C and 700°C. However, the dip in indentation modulus at 200°C was not expected. Similarly, the initial increase in hardness was expected, as were the large

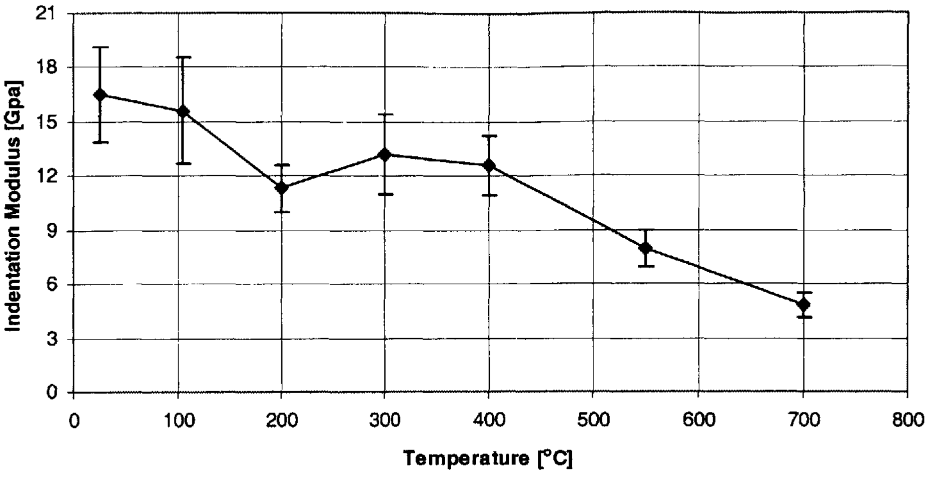

Figure 5-6: Microindentation results: average indentation modulus of cement paste exposed to various temperatures.

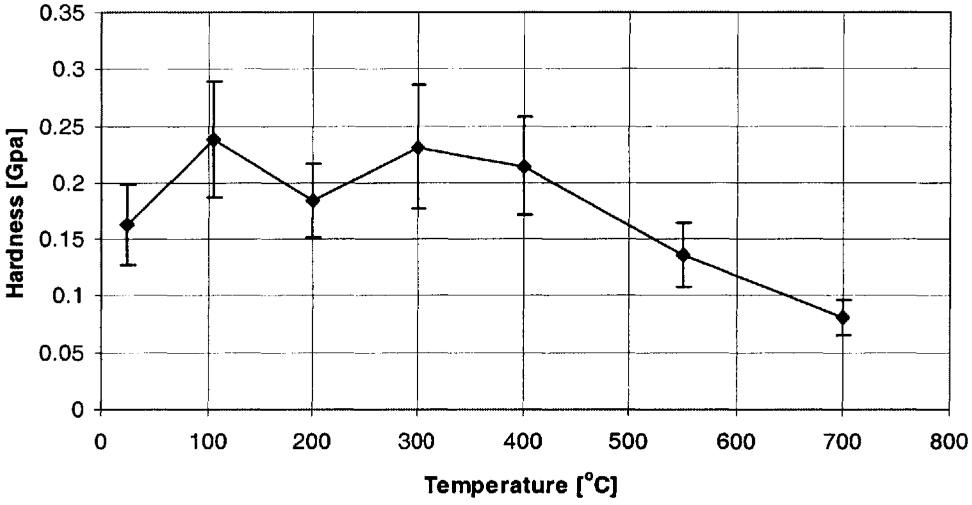

Figure 5-7: Microindentation results: average hardness of cement paste exposed to various temperatures.

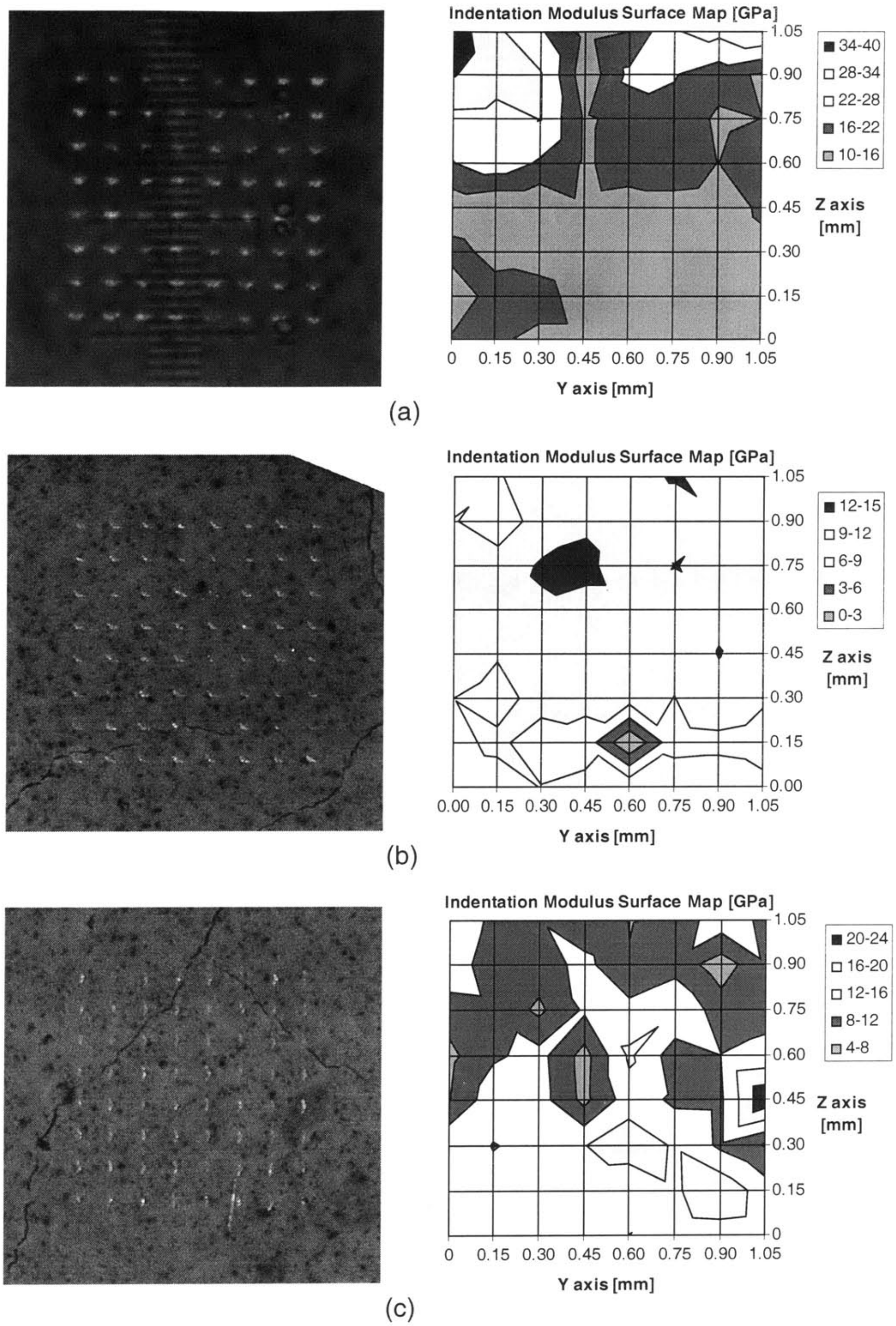

Figure 5-8: Microindentation grid and corresponding indentation modulus surface map for samples heated to (a) 105°C, (b) 200°C, and (c) 300°C.

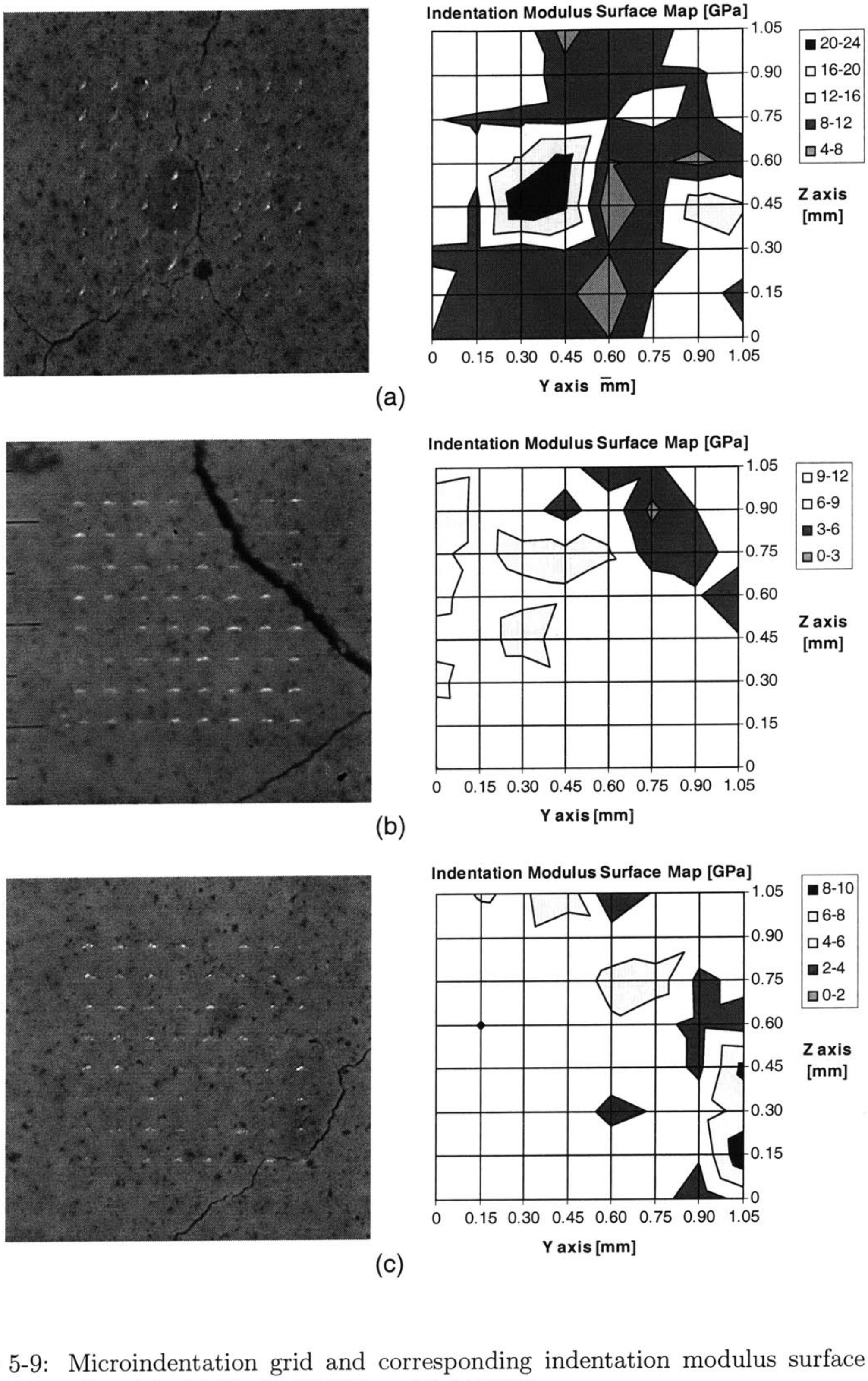

Figure 5-9: Microindentation grid and corresponding indentation modulus surface map for samples heated to (a) 400°C, (b) 550°C, and (c) 700°C.

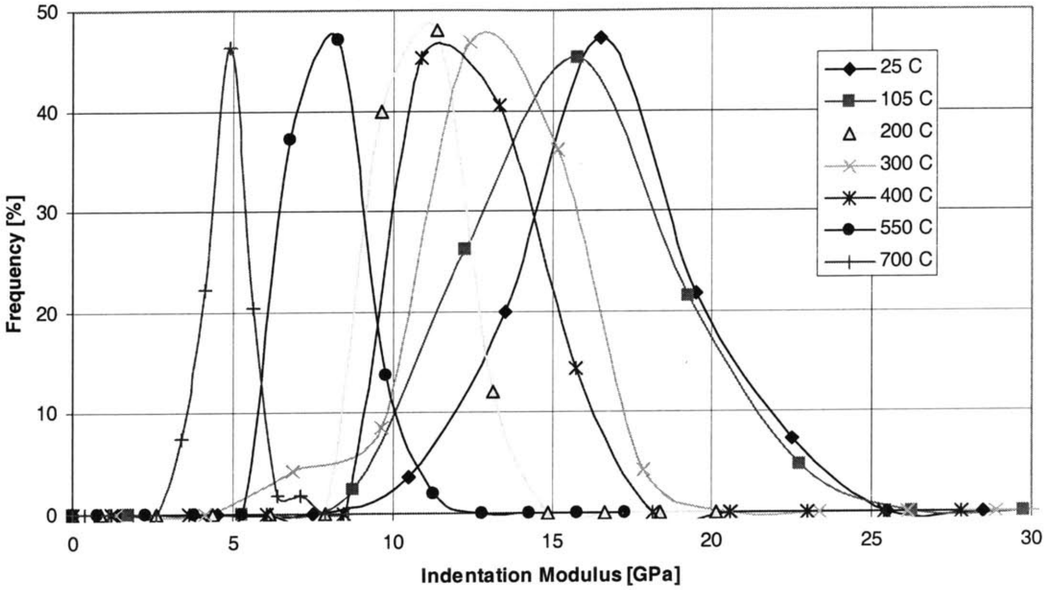

Figure 5-10: Microindentation results: indentation modulus frequency distributions of all temperatures investigated.

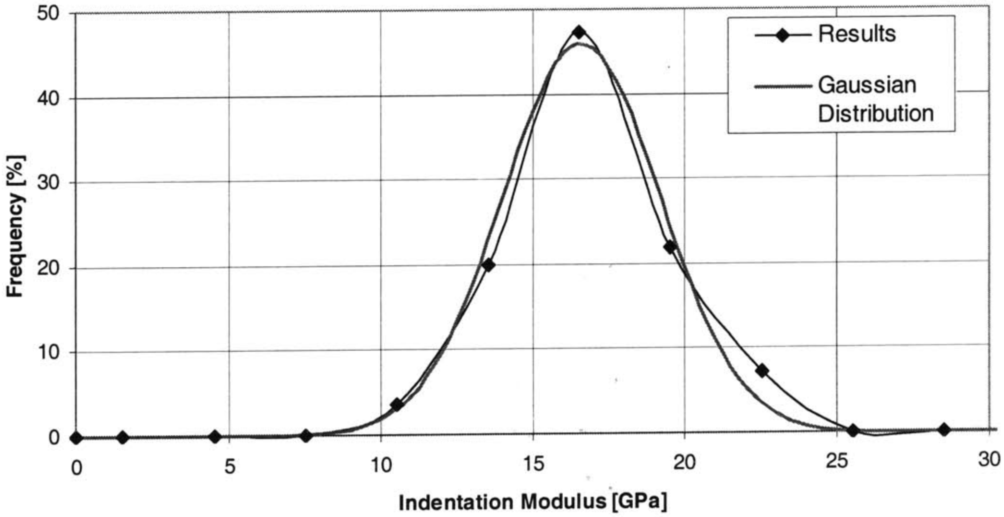

Figure 5-11: Microindentation results: indentation modulus frequency distribution of saturated cement paste fit with a Gaussian distribution.

decreases in hardness at 550^{o}C and 700^{o}C, but the dip in hardness at 200^{o}C also came as a surprise. Further investigation of the results of samples exposed to a temperature of 200^{o}C was necessary.

Furthermore, although the trends observed in the results (except the 200^{o}C datum) were similar to data in the literature, the quantitative values of both the modulus of elasticity and the hardness were lower than expected. Using microindentation, the initial modulus of elasticity was found to be 15.7 GPa (assuming $\nu = 0.24$), whereas using resonant frequency the elastic modulus was found to be 19.5 GPa. Additionally, Constantinides [13] ($w/c = 0.5$, cured for >90 days) found an initial modulus of elasticity of 19.1 GPa using microindentation. All other elastic modulus values for heated samples appear to be reasonable relative to the initial saturated value, but were therefore also lower than expected. Similarly, using microindentation, the initial hardness was found to be 0.163 GPa, whereas Xu *et al.* [61] ($w/c = 0.5$, cured for 90 days) found an initial hardness value of 0.415 GPa and Constantinides [13] found an initial hardness of 0.498 GPa. Again, all other hardness values for heated samples were also lower than expected.

In order to investigate these unexpected results, an additional saturated sample (25^{o}C) and an additional sample heated to 200^{o}C were tested. These samples were cured in lime water for 90 days (instead of 28 days) and then prepared, heated, and tested using the same methods previously described. The new results are plotted with the original results in Figure 5-12. Clearly, both the indentation modulus and hardness increased significantly because of the increased curing time. The new initial modulus of elasticity was found to be 20.8 GPa (assuming $\nu = 0.24$), which seems more reasonable when compared with resonant frequency results and the results of Constantinides [13].

The most likely explanation for the higher elasticity results is the evolution of the pore structure during curing. Cook and Hover [16] used mercury intrusion porosimetry (MIP) to investigate the pore structure of several cement pastes after different curing periods. For a w/c ratio of 0.5, they found that the dominant pore size decreases from around 1,000 nm after a few days of curing, to less than 100 nm after 56 days of curing. They also found that the overall porosity decreases considerably during the same curing period. As a result, the volume and dominant pore size of the capillary porosity seems to have been much higher at the time of testing (cured for 28 days) than for fully hydrated cement paste with a w/c ratio of 0.5. Clearly this had a significant effect on the modulus of elasticity measured by microindentation. However, the saturated resonant frequency test seems to have been less affected by larger capillary porosity. This can be explained by the dependence of the resonant frequency results on the density of the material. The density of the water filling the capillary pores contributes significantly to the density of the material, therefore contributing significantly to the results of resonant frequency testing. However, the water in the capillary pores contributes little to resisting the indenter as it is pushed into the material.

Because the capillary porosity increases with the water cement ratio [16], it seems that our initial indentation tests were essentially on a material with a w/c ratio higher than 0.5. However, because the relative evolution of the modulus of elasticity with respect to temperature is independent of the w/c ratio [37], the normalized original results are still valid. Therefore, the original relative elasticity values will be used with the new initial value of 20.8 GPa. Assuming that the evolution of the hardness with respect to temperature is also independent of the w/c ratio, the original relative hardness values are similarly applicable. Normalized elasticity and hardness values for the original (cured for 28 days) and new (cured for 90 days) microindentation results are plotted in Figure 5-13.

Using Figure 5-13, the validity of the original results of the sample heated to 200°C can be more easily assessed. The new elasticity value at 200°C appears to fit much better than the original value in the expected evolution of the elasticity. The new hardness value also fits better, although it was still lower than expected. Further testing would be necessary to conclusively determine the relative change in elasticity and hardness after heating to 200°C, but the new results seem more logical and will be assumed to be correct for modeling purposes.

Now that the unexpected results have been addressed, the normalized microindentation elasticity results were plotted with the results of Dias *et al.* [18] for comparison (see Fig. 5-14). The results were plotted normal to the 105°C value to eliminate incomparable effects of drying on the resonant frequency results. Generally, Figure 5-14 shows that the trends found using microindentation compare well with the results of Dias *et al.* However, the relative decrease in elasticity is noticeably less in the microindentation results, especially for the 200°C, 300°C, and 400°C data points. This makes sense because of the different scale of investigation of each

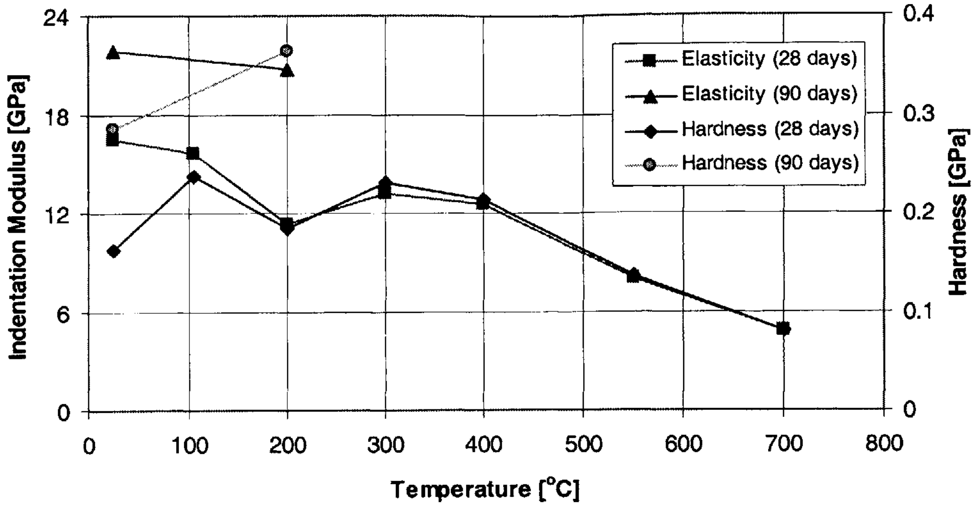

Figure 5-12: Comparison of microindentation results on cement paste cured for 28 days and 90 days.

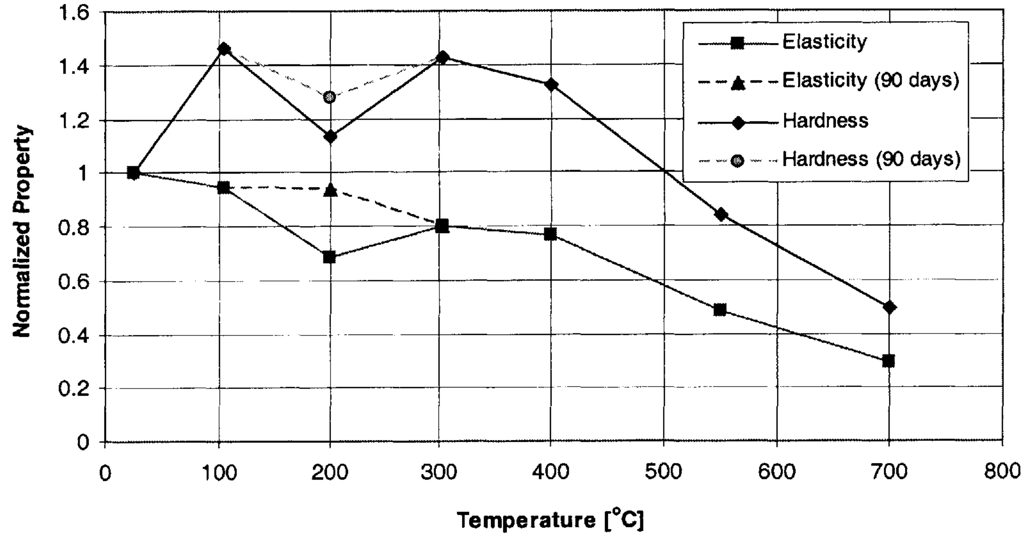

Figure 5-13: Comparison of normalized microindentation results on cement paste cured for 28 days and 90 days.

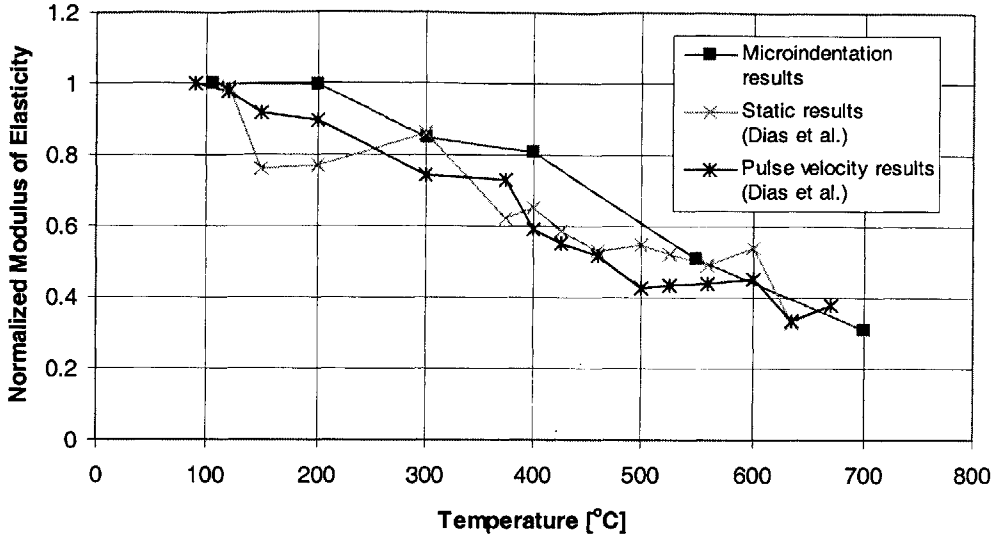

Figure 5-14: Comparison of normalized microindentation modulus of elasticity results with the results of Dias *et al.* [18].

study. In this study, macrocracks were present at the scale of investigation, but the effects of these macrocracks were eliminated using the optical images and surface mapping methods previously discussed. However, Dias *et al.* determined the dynamic and static modulus of elasticity at a larger scale, the macroscale, which included the effects of macrocracking. This is interesting because it gives a qualitative estimate of the effect of macrocracking on the elasticity of cement paste after exposure to various temperatures.

Similarly, the normalized microindentation hardness results were plotted with the results of Xu *et al.* [61] for comparison (see Fig. 5-15). The results show a similar trend: an initial increase followed by continual decrease. More temperature specific trends are impossible to compare because of the relatively few number of data points investigated by Xu *et al.* However, it is clear that the new normalized microindentation results were higher at all temperatures of investigation.

A second interesting comparison is that of hardness and compressive strength (see Fig. 5-16). The hardness and compressive strength compare remarkably well indicating an expected relationship between them. Both increase and decrease in a similar fashion, although the

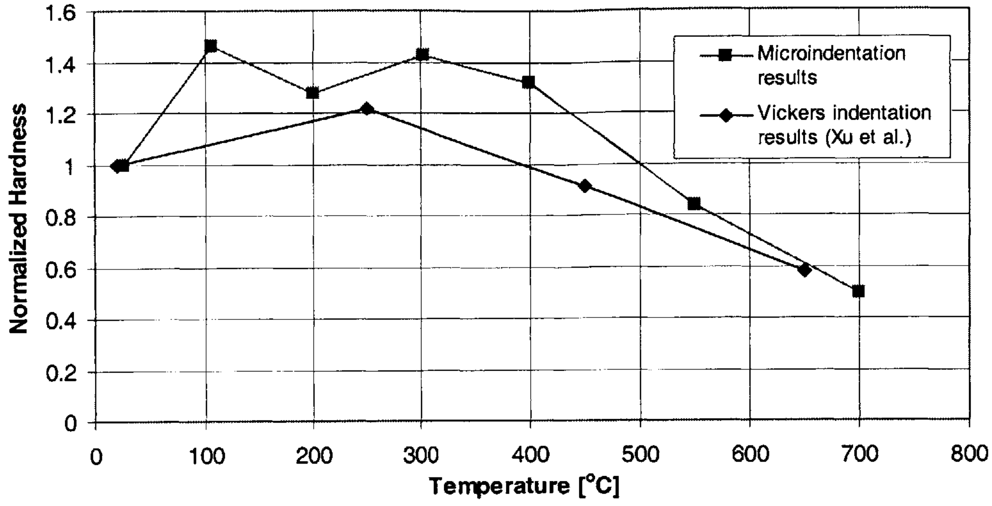

Figure 5-15: Comparison of normalized microindentation hardness results with the results of Xu *et al.* [61].

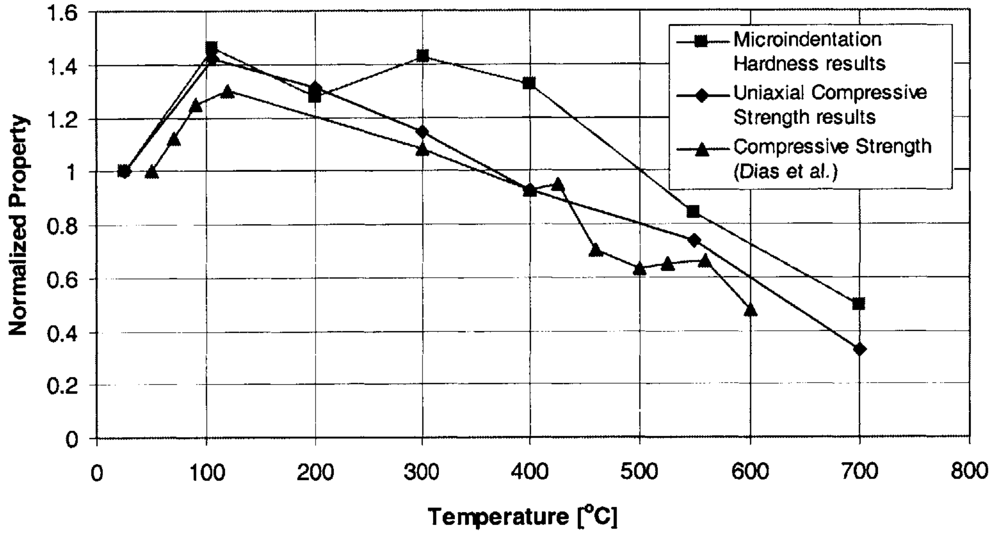

Figure 5-16: Comparison of normalized microindentation hardness results with uniaxial compressive strength results from this study and the compressive strength results of Dias *et al.* [18].

relative microindentation hardness is distinctly higher for the 300°C and 400°C data points. Again, this seems to be a result of the different scales of investigation of each study. As previously discussed, the effects of macrocracking, which increase significantly at 300°C and above, were necessarily eliminated from the microindentation results. However, the uniaxial compressive strength results, which are especially sensitive to defects such as cracking, included macrocracking effects. Therefore, the qualitative macrocracking effects that were observed in the discussion of elasticity, are further evidenced in the hardness results.

It is also interesting to note that the effects of macrocracking were reduced at the 550°C and 700°C data points. This indicates that instead of macrocracking, material degradation at a smaller scale began to govern both the hardness and elasticity results at the macroscale. Material degradation at a smaller scale is known to occur after exposure to temperatures of 550°C and higher through the coarsening of the pore structure, the dehydration of CH, and microcracking, as discussed in Chapter 2. The fact that these smaller scale effects are more critical than the extensive cracking that was visibly observed, is both significant and surprising.

5.5 Summary and Conclusions of Microindentation

Microindentation was used to determine the hardness and elasticity of homogenized cement paste: 'Level II' of the multiscale microstructure. As a result of this investigation, the following conclusions were drawn:

- **Surface Mapping:** Comparison of surface images to indentation modulus surface maps provided an effective method of evaluating the effects of visible heterogeneities like cracks, large pores, and stiff pre-hydrated areas.

- **Frequency Distributions:** Indentation modulus frequency distributions showed one clear peak indicating that the indentation depth was sufficient to access the homogenized properties of cement paste.

- **Capillary Porosity:** Microindentation of cement paste is especially sensitive to capillary porosity. Additionally, the conclusion of previous investigations that the capillary porosity of cement paste decreases significantly with curing time was confirmed.

- **Elasticity:** High temperature elasticity degradation was effectively measured using microindentation. Microindentation results compared remarkably well with macroscopic results, indicating that a majority of degradation occurred at some scale below the scale of investigation. However, the relatively small difference between macroscopic and microscopic results qualitatively showed the effect of macrocracks (which were primarily present after exposure to temperatures $> 300^o$C) on the elasticity.

- **Hardness:** Comparison of normalized hardness results and normalized macroscopic compressive strength results indicates that hardness is clearly related to compressive strength. Similar to elasticity, the difference between hardness and compressive strength qualitatively showed the effect of macrocracks (which were primarily present after exposure to temperatures $> 300^o$C) on the hardness. However, macrocracking clearly affected the hardness more than the elasticity.

Perhaps the most significant result of microindentation is the confirmation that indentation can be applied to accurately measure material properties of complex heterogeneous materials such as cement paste. Clearly, high temperature degradation of homogenized cement paste, which has been extensively measured at the macroscale, was successfully measured at the microscale. Furthermore, comparison of macroscopic and microscopic results have identified that macrocracking is one source of high temperature degradation. However, this is only the first step towards determining all of the sources of high temperature degradation of cement paste. Clearly microcracking is one source, but microindentation results indicate that the primary sources of high temperature degradation affect the microstructure at a smaller scale. This is why the results of microindentation are so critical. Because indentation has been confirmed to be effective, it can now be used to determine the effects of high temperature degradation at an even smaller scale: the nanoscale.

Chapter 6

Nanoindentation

The goal of nanoindentation is to access the hardness, elasticity and volume fractions of the various phases of cement paste at 'Level I' of the multiscale microstructure introduced in Section 2.2. The general methods of indentation were presented in Section 5.1, but the specific methods of nanoindentation will be addressed at the beginning of this chapter. Second, the unfiltered results, or 'General Results', will be presented and discussed. Third, the filtered results, or 'Phase Results', will be presented and discussed. Last, a summary of the main conclusions of nanoindentation will be presented.

6.1 Methods Specific to Nanoindentation

Nanoindentation tests were conducted using the TriboIndenter (Hysitron, Inc.) in the NanoMechanical Technology Laboratory at MIT. Methods specific to nanoindentation were divided into two categories: testing methods and analysis methods.

6.1.1 Testing Methods

Nanoindentation samples were prepared as described in Section 3.2. Each investigated temperature (25°C, 105°C, 200°C, 300°C, 400°C, 550°C, and 700°C) was tested in the same manner, described by the following specifications:

- **Indentation Depth:** The indentation depth determines the volume of material being tested and therefore defines the length scale, or 'Level' of the multiscale microstructure, that is being investigated. As previously mentioned, the goal of nanoindentation is to access the properties of the individual phases (LD C-S-H, HD C-S-H, CH) of cement paste, so a proper indentation depth must be selected accordingly. The C-S-H phases vary in size but typically have a characteristic length scale from ~40 nm up to several hundred nanometers or even micrometers in well hydrated pastes [52]. For lower water-cement ratios, their characteristic length scale can be even higher. The C-S-H phases are themselves heterogeneous at a length scale corresponding to the gel porosity (< 10 nm). Additionally, the CH crystals have a characteristic length scale that also varies, but CH crystals are known to exist up to the micrometer range, with heterogeneities only at very small scales (< 10 nm).

Ideally, indentation would be done between the two characteristic length scales of the heterogeneities of each phase, according to the 'separation of scale' requirement previously discussed (see Section 5.1.3). However, because of the varying sizes of each phase, it is impossible to directly meet this requirement. Additionally, it would be unreasonable to select indentation depths less than 100 nm, because surface roughness has a more dominant effect at that scale. As an alternative to meeting the upper 'separation of scale' requirement, statistical analysis can be conducted to determine the properties of the various phases, as long as indentation depths are significantly greater than the scale of phase heterogeneities (< 10 nm). In order to best meet the 'separation of scale' requirements, an indentation depth range of 100-300 nm was desired. Because the equipment is load controlled not depth controlled, the maximum load was selected to maintain indentation depths in the desired range.

- **Load Function:** A typical indentation load function is displayed in Figure 5-1. The maximum specified load varied from 600-800 μN for the different investigation temperatures in order to achieve the desired indentation depth of 100-300 nm. The specified time of both loading and unloading was 10 seconds, corresponding to a loading and unloading rate of 60-80 μN/s. The specified dwell time at the maximum load was 10 seconds.

- **Grid Spacing and Size:** A ten by ten indentation grid (100 indents) was used for all tests. At least two different samples were grid indented (200 total indents) for each temperature investigated. The specified grid spacing was 15 μm yielding a total grid surface area of 105 μm x 105 μm (approximately 0.1 mm^2). The grid spacing was chosen to be much larger than the maximum size of each phase, so that if characteristic phase sizes were larger than expected, they would not have a dominant effect on the statistical results. In other words, this large grid spacing allows statistical analysis to be used to accurately determine the properties of the individual phases.

- **Calibration:** Load and depth calibrations were measured and applied as suggested by the manufacturer of the equipment used.

6.1.2 Analysis Methods

The Oliver and Pharr [41] method was used to determine the indentation modulus and the hardness from the indentation data of each indent. However, a method of determining the validity of each indentation was necessary. Because indentation depths were so small, the method of optical imaging and surface mapping used for microindentation was not possible. An alternative method was necessary.

The load-displacement data was examined in order to determine the validity of each indentation. Discontinuous load-displacement plots (see Fig. 6-1(a)) were observed which had a 'jump' or several 'jumps' in the indentation depth. The cause of these jumps is uncertain, but they most likely occurred because of subsurface cracking during the force-driven indentation tests. Such cracking would explain the observed behavior: sudden increase in depth with no increase in measured load. As a result, the measured contact depth, h_c, and the corresponding contact area, A_c, were measured incorrectly. Therefore, results corresponding to these discontinuous plots were eliminated.

Up to 400°C, relatively few indentation plots were eliminated for each temperature investigated, so the number of usable results still allowed a valid statistical analysis. However, for samples exposed to higher temperatures (550°C and 700°C), the number of invalid indentations increased dramatically. As a result, a method of revising the discontinuous load-displacement plots was necessary. For load-displacement plots with only one distinct discontinuity, the depth was adjusted by the amount of the 'jump' when the discontinuity occurred (see Fig. 6-1(b)). Essentially, this revised the measured contact area to a more reasonable value. Using this

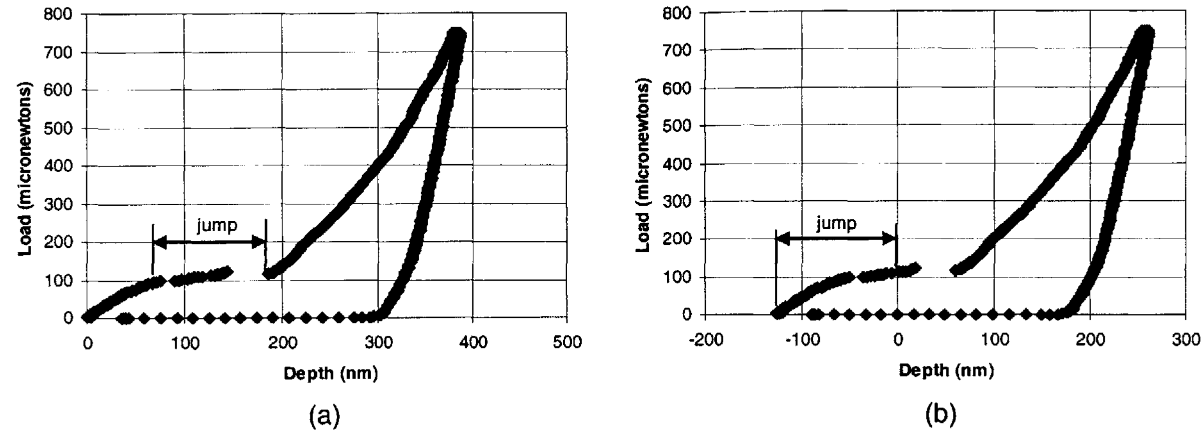

Figure 6-1: Typical discontinuous nanoindentation load-displacement plots (a) without depth correction, (b) with depth correction.

depth adjustment method where possible allowed a valid analysis of the indentation for these higher temperatures of investigation.

6.2 General Results

The primary goal of nanoindentation is to access the properties of the individual phases of cement paste at 'Level I'. However, before determining the properties of each phase using frequency distributions, an evaluation of the entire data set with no distinction between phases is useful for comparison with microindentation results. In other words, the results will first be presented as if only one homogeneous phase was present at the scale of investigation, as was the case for microindentation. Table 6.1 summarizes the nanoindentation results for all temperatures of investigation. The effect of high temperatures on the hardness and indentation modulus can be seen more clearly in Figures 6-2 and 6-3. The indentation modulus is plotted with respect to the hardness in Figure 6-4, from which α was determined for all investigated temperatures. The various temperatures of investigation are difficult to distinguish in Figure 6-4, so the indentation modulus versus hardness was also plotted separately for the indentation results on unheated samples (25°C) and samples heated to 550°C (see Fig. 6-5). This figure more clearly displays the increase in scatter that occurred as a result of an increase in exposure

Temp.	No. of Indents		h_{max}	P_{max}	M	H	α
[°C]	Total	Used	[nm]	[μN]	[GPa]	[GPa]	
25	200	179	193 ± 52	771 ± 8	23.0 ± 9.3	0.895 ± 0.473	0.43
105	200	156	186 ± 46	770 ± 9	21.8 ± 8.4	0.983 ± 0.596	0.50
200	200	160	178 ± 52	774 ± 8	22.8 ± 10.9	1.19 ± 0.736	0.38
300	200	177	205 ± 81	770 ± 12	20.7 ± 12.2	1.00 ± 0.768	0.48
400	200	142	202 ± 69	771 ± 10	20.6 ± 10.5	1.01 ± 0.753	0.50
550	200	160	345 ± 108	735 ± 40	9.17 ± 4.9	0.346 ± 0.534	0.48
700	200	139	261 ± 118	656 ± 24	11.4 ± 5.9	0.683 ± 0.693	0.36

Table 6.1: Summary of the results of nanoindentation when considering the microstructure to be one homogeneous phase at the scale of investigation.

temperature.

6.3 Discussion of General Results

The results of nanoindentation in Table 6.1 give us insight into the effectiveness of the testing procedure and the microstructure at the scale of investigation. First, the number of valid indentations can be used to qualitatively evaluate the state of the microstructure. Up to 300°C, the exposure temperature had little effect on the number of valid indentations (80-90%). However, at higher exposure temperatures, the number of valid indentations decreased dramatically. Recall that the number of indentations used at 550°C and 700°C include indentations for which the depth was corrected, while depth correction was not used for lower temperatures. Clearly, after exposure to temperatures above 300°C, the cement paste was noticeably more degraded.

Recall that the maximum *depth* was specified for microindentation, whereas the maximum *load* was specified for nanoindentation. The same specified maximum load was used for all temperatures of investigation up to 400°C, so the recorded maximum load (P_{max}) was basically constant in that temperature range. For higher temperatures of investigation, the maximum load was adjusted down slightly to maintain a maximum depth comparable with that of lower temperatures of investigation. Recall that similar depth is necessary to maintain a similar scale of investigation. Based on the results, the maximum load should have been reduced a bit more because the maximum depth (h_{max}) still increased significantly at higher temperatures. This increase in depth indicates that the material became much softer after exposure to temperatures above 400°C. The large standard deviation of all maximum depth results is

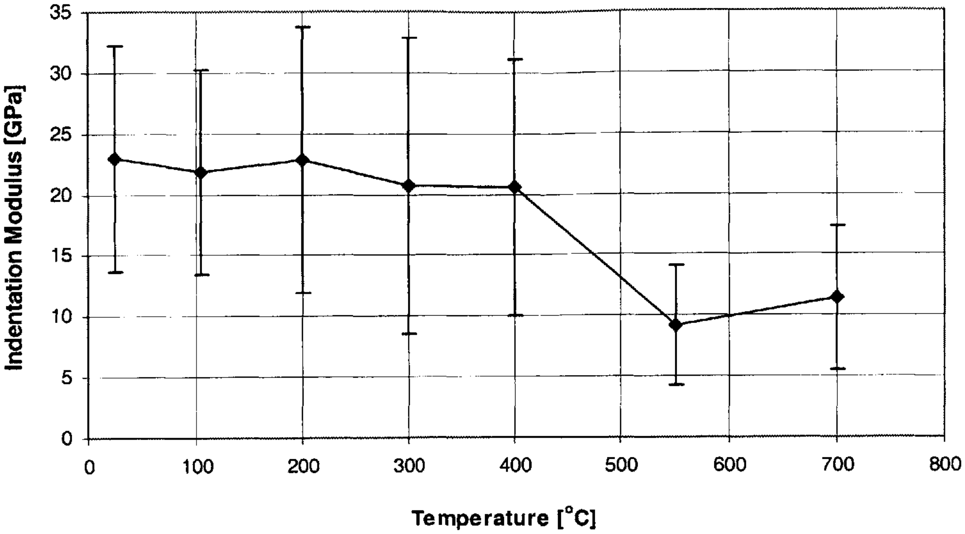

Figure 6-2: Nanoindentation elasticity results considering one homogeneous phase at the scale of investigation.

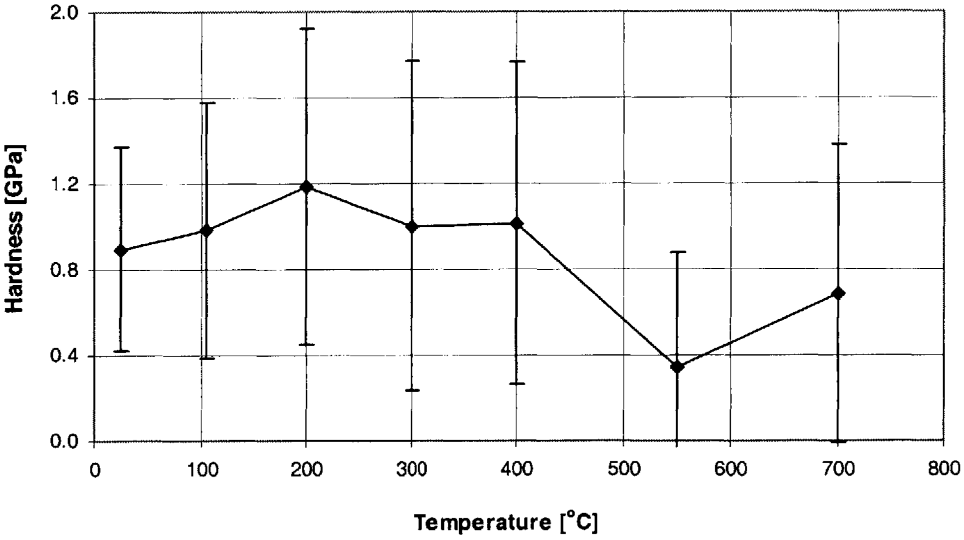

Figure 6-3: Nanoindentation hardness results considering one homogeneous phase at the scale of investigation.

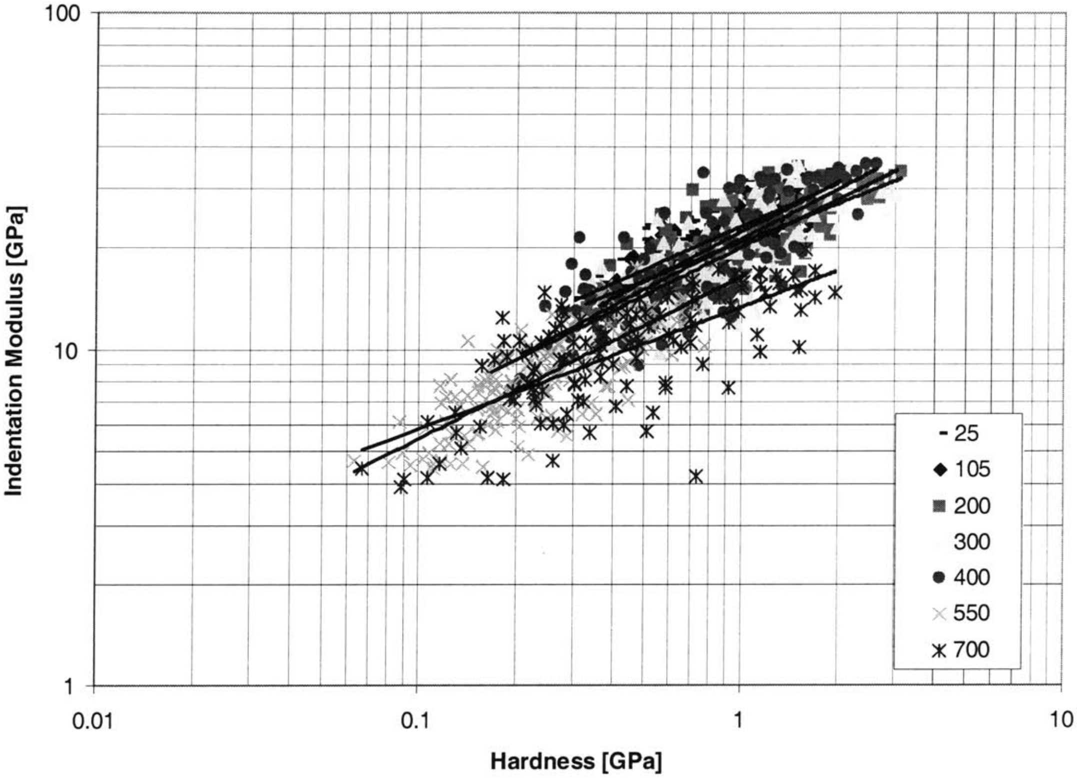

Figure 6-4: Nanoindentation results: indentation modulus versus hardness for all indentations at all temperatures of investigation.

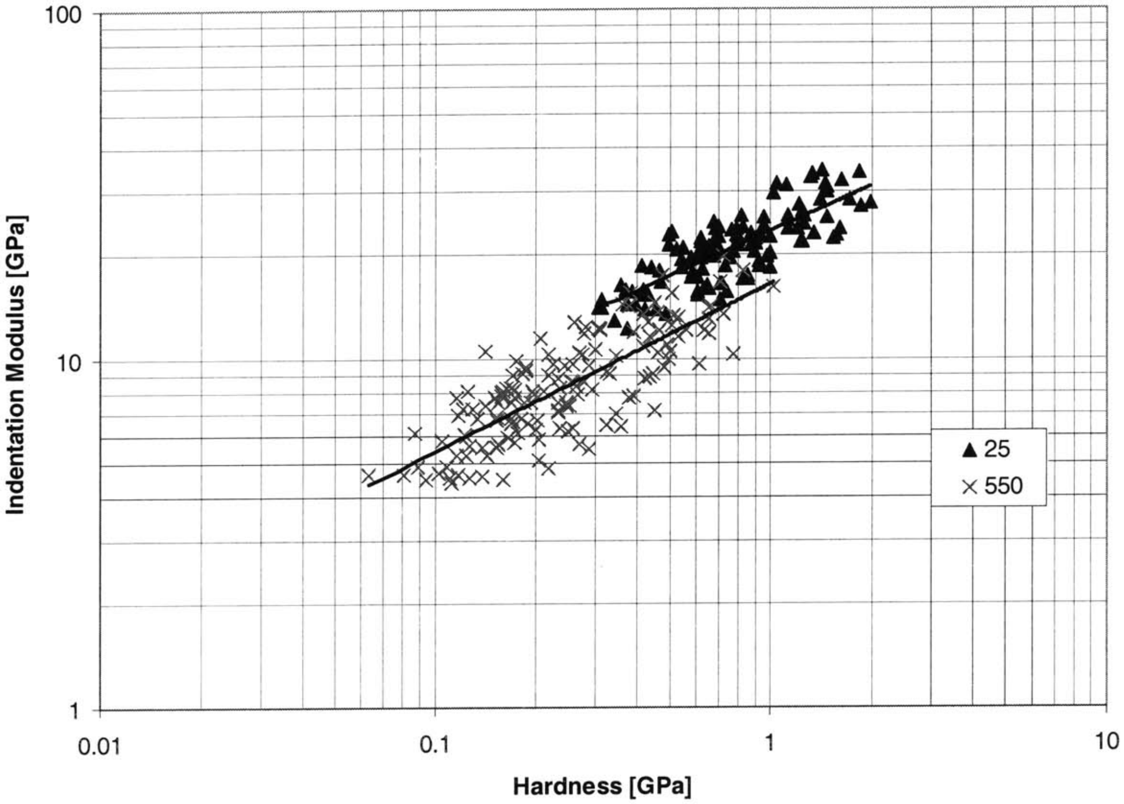

Figure 6-5: Nanoindentation results: indentation modulus versus hardness for all indentations on unheated samples (25^{o}C) and samples heated to 550^{o}C.

noteworthy, and indicates that material properties vary significantly between the locations of each indentation. This is the first evidence of the various phases which are actually present at the scale of investigation.

The most noticeable feature of the indentation modulus (M) and hardness (H) results is the extremely large standard deviation of all results (see Table 6.1 and Figures 6-2 and 6-3). Based on these standard deviations, the assumption of one phase at the scale of investigation is clearly illogical, further verifying the presence of several phases at 'Level 1' of the multiscale microstructure. However, despite these large standard deviations, the effect of temperature on the indentation modulus and the hardness is still useful for comparison to microindentation results. Most noticeably, the trends at both scales of investigation are quite similar. Both show a slow initial decrease in indentation modulus, followed by a large decrease at higher temperatures of investigation. Likewise, both show an initial increase in hardness followed by a large decrease at higher temperatures of investigation. Additionally, comparison of the magnitude of results indicates that both the hardness and indentation modulus are much larger at the smaller scale accessed by nanoindentation. This qualitatively shows the effect of porosity and possibly microcracking on the results.

Last, the $M - H$ scaling relation parameter (α) can again be used as a means of evaluating the validity of indentation results. At most temperatures of investigation, the value of α in Table 6.1 was remarkably close to the theoretical value of 0.5. Only results for samples exposed to 200^{o}C and 700^{o}C varied somewhat from this theoretical value. This indicates that the surface of these samples might have been slightly rougher than the other samples. However, the low value of $\alpha = 0.36$ for samples heated to 700^{o}C might come from another source. In light of the existing knowledge that has been discussed (see Table 2.6), the effects of increasing porosity and microcracking at the scale of investigation might also cause this deviation in α from the theoretical value.

6.4 Method of Analyzing Multiple Phase Frequency Distributions

Clearly, the previous section established that more than one phase exists at the scale of investigation. Therefore, the fact that several phases are present must be taken into account when interpreting the data. Therefore, once the invalid data had been eliminated as discussed in Section 6.1.2, frequency distributions were used to determine peaks which represented each individual phase. The goal was to fit each peak with a Gaussian distribution in order to determine properties of each phase. However, a consistent fitting method is necessary to ensure accurate results.

- **Bin Size:** In order to plot a frequency distribution, it is first necessary to select a bin size. This seems trivial, however, the bin size must be selected with care. If too large of a bin size is selected, the results will effectively be homogenized, similar to selecting a greater indentation depth. However, if too small of a bin size is selected, results could fluctuate so much that distinguishable peaks are no longer visible. Therefore, a method of selecting an appropriate bin size is necessary.

  In order to fit a Gaussian distribution to each phase present in a frequency distribution, it is necessary to determine the mean value, standard deviation, and volume fraction of each gaussian distribution representing each phase. Therefore, in order to fit n phases, the total number of unknowns is $3 \times n$. However, there is an additional constraint that the sum of all the volume fractions must equal one, resulting in a total number of unknowns of $3n - 1$.

  The selection of the bin size determines the number of input values to the gaussian fitting. In other words, the bin size determines the number of input values, or the number of bins, m, within the range of indentation data. In order for the system to be determined, the number of inputs must equal the number of unknowns: $m = 3n - 1$. Therefore, the minimum number of bins necessary for an accurate fitting of gaussian distributions to each phase is $m_{min} = 3n - 1$. A typical indentation modulus frequency distribution is shown in Figure 6-6.

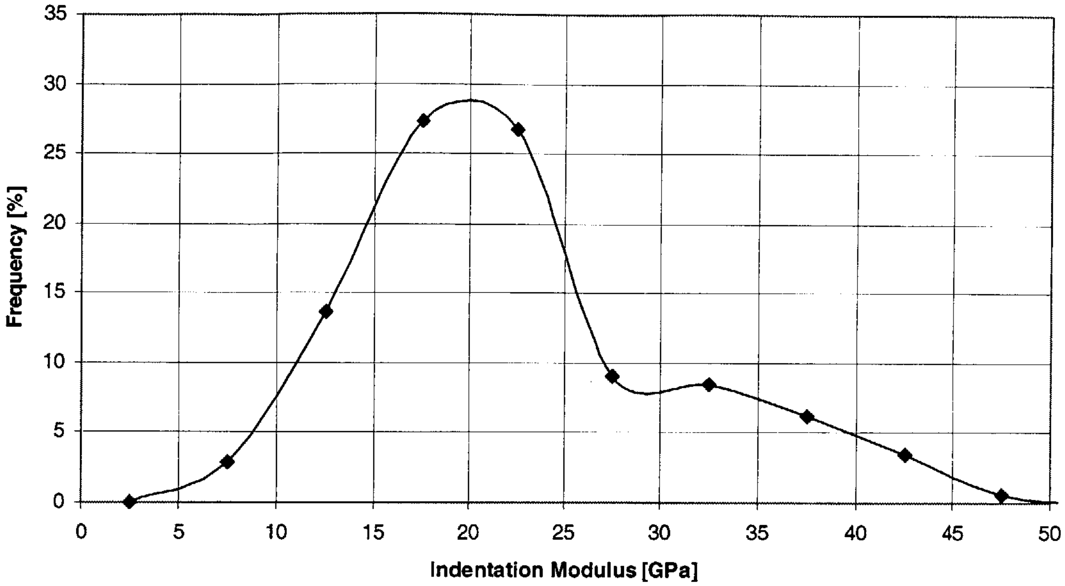

Figure 6-6: Nanoindenation results: indentation modulus frequency distribution for unheated samples (25°C).

- **Fitting Method:** With the bin size selected, a method of determining the best fit gaussian distributions was necessary. First, the sum of the phase gaussian distributions (f_b^{sum}) corresponding to each bin (b) was determined:

$$f_b^{sum} = f_b^{phase\ 1} + f_b^{phase\ 2} + ... + f_b^{phase\ n} = \sum_{r=1}^{n} f_b^r \tag{6.1}$$

where f_b^r is the gaussian distribution frequency value for phase r corresponding to bin b, and n is the total number of phases. Second, the difference between the sum of the phase gaussian distributions (f_b^{sum}) and the indentation frequency value (f_b^{indent}) for each bin was calculated ($f_b^{indent} - f_b^{sum}$). Finally, fitting was performed by minimizing the sum of the squares of this difference:

$$\min\left(\sum_{b=1}^{m_{min}} \left(f_b^{indent} - f_b^{sum}\right)^2\right) \tag{6.2}$$

A typical frequency distribution with gaussian distributions fit to each phase is displayed in Figure 6-7(a). Fitting resulted in the determination of the mean value, standard deviation, and volume fraction of each phase.

- **Effect of Bin Size:** Once the fitting had been completed for the required number of bins, $m_{min} = 3n - 1$, a method of reducing the possible error due to the particular bin size selected was desired. First, a second frequency distribution was plotted with the number of bins (m_2) increased by 30-50% (see Fig. 6-7(b)). Increasing the bin size increased the 'noise' in the frequency distributions and made the phase peaks less defined. Second, the sum of the phase gaussian distributions ($\mathrm{f}_{b_2}^{sum}$) corresponding to each new bin (b_2) was determined. Third, the difference between the sum of the phase gaussian distributions ($\mathrm{f}_{b_2}^{sum}$) and the indentation frequency value ($\mathrm{f}_{b_2}^{indent}$) for each bin was again calculated ($\mathrm{f}_{b_2}^{indent} - \mathrm{f}_{b_2}^{sum}$). Fourth, the sum of the squares of this difference was calculated:

$$Sum\ of\ Squares = \sum_{b_2=1}^{m_2} \left(\mathrm{f}_{b_2}^{indent} - \mathrm{f}_{b_2}^{sum}\right)^2 \tag{6.3}$$

Last, fitting was determined by minimizing the sum of the sum of the squares of the two bin size frequency distributions:

$$\min\left(\sum_{b=1}^{m_{min}} \left(\mathrm{f}_{b}^{indent} - \mathrm{f}_{b}^{sum}\right)^2 + \sum_{b_2=1}^{m_2} \left(\mathrm{f}_{b_2}^{indent} - \mathrm{f}_{b_2}^{sum}\right)^2\right) \tag{6.4}$$

In other words, the error between the 'Sum of Gauss Distributions' and the 'Indentation Data' in Figures 6-7(a) and 6-7(b) was simultaneously minimized. As a result, the possible error associated with selecting one particular bin size was effectively reduced, and the mean value, standard deviation, and volume fraction of each phase was finally determined.

6.5 Analysis of Phase Properties

6.5.1 Phase Modulus of Elasticity Results

The indentation modulus frequency distribution used to obtain phase results for unheated samples (25°C) was displayed in Figure 6-7. The rest of the indentation modulus frequency

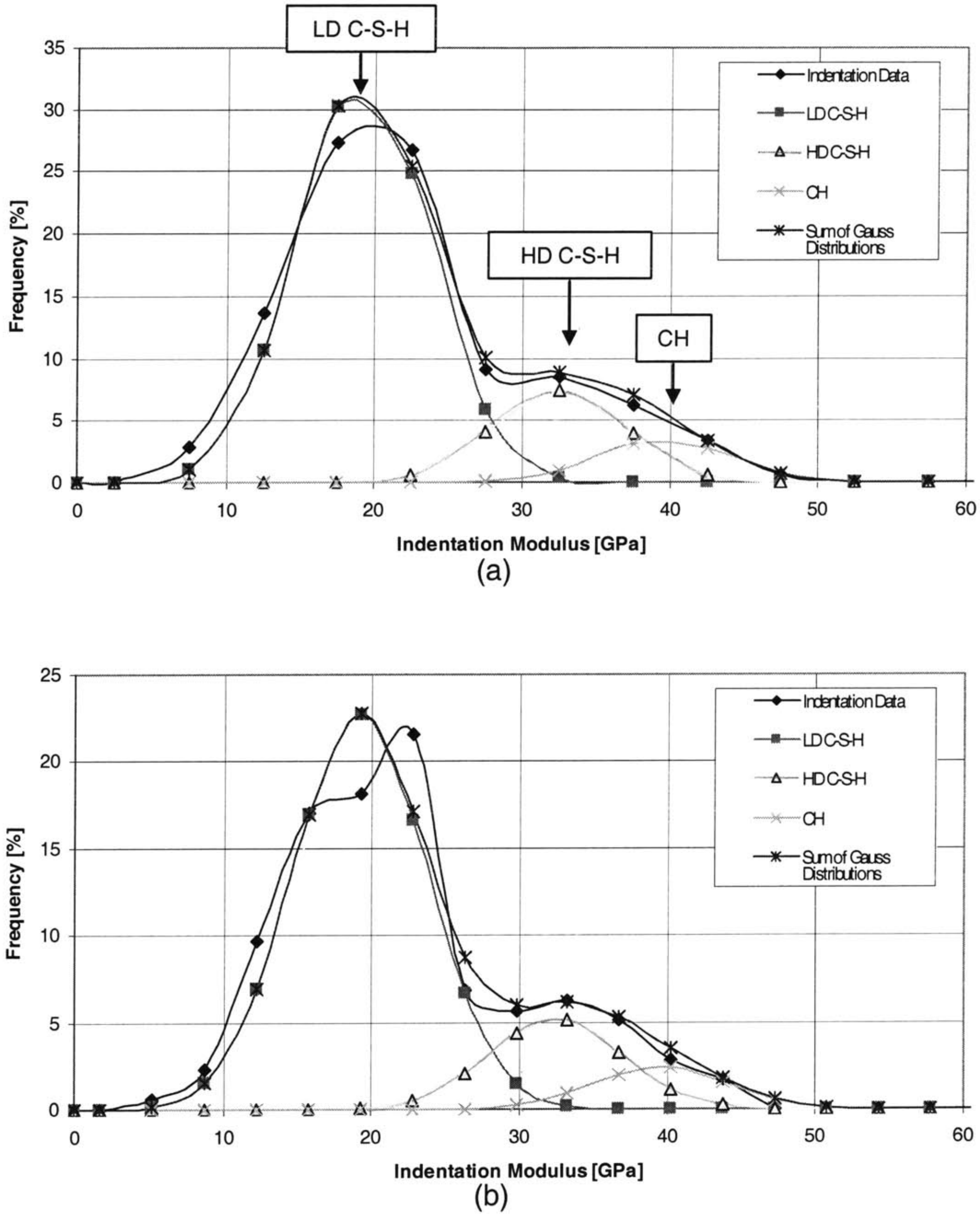

Figure 6-7: Nanoindentation indentation modulus frequency distribution with gaussian distributions fit to each phase for unheated samples (25°C): (a) minimum bin size, (b) number of bins increased 30-50%.

distributions, from which the phase elasticity values and volume fractions were determined, are presented in Figures 6-8 and 6-9. Additionally, the effect of removing data corresponding to discontinuous load-displacement plots ('cracked' data) is shown in Figure 6-10. This figure clearly shows that the 'cracked' data corresponding to a meaningless peak with relatively low elasticity was successfully removed by eliminating discontinuous load-displacement plots.

Using the indentation modulus frequency distributions, the mean indentation modulus (M) and volume fraction of each phase was determined. Table 6.2 displays the results of this analysis. The relative percentage of the two types of C-S-H is of particular interest and is included in Table 6.2. Figure 6-11 displays the evolution of the indentation modulus of each phase with respect to exposure temperature. The actual modulus of elasticity (E) can be calculated from the results in Table 6.2 using Eq. (5.5), assuming a Poisson's ratio of 0.24.

6.5.2 Phase Hardness Results

Similar to the indentation modulus, the hardness of each phase was determined using hardness frequency distributions with fitted gaussian distributions. However, because the hardness is especially sensitive to the measurement of the contact area, the error and standard deviation of hardness results were larger than for the elasticity results. As a result, phase hardness peaks were often less distinct in the hardness frequency distributions, so phase properties were more difficult to determine. Because of this, the fitting method described in Section 6.4 was still used, but with one exception. The phase volume fractions determined using indentation modulus frequency distributions were fixed when minimizing the error using the hardness frequency distributions. As a result, the mean values and standard deviations were the only unknowns which were adjusted during minimization.

Figure 6-12(a) shows the hardness frequency distribution for the indentations on unheated samples (25°C). At first glance, two primary peaks seem clear, which were originally assumed to represent the LD C-S-H and HD C-S-H. However, Figure 6-12(b) displays the hardness frequency distribution with gaussian distributions fit to each phase using the fitting method previously described. Because the three fitted phases were not clearly visible, verification that the fit results were accurate was needed. For verification, the hardness frequency distribution of each phase (LD C-S-H, HD C-S-H, CH), as determined by the indentation modulus

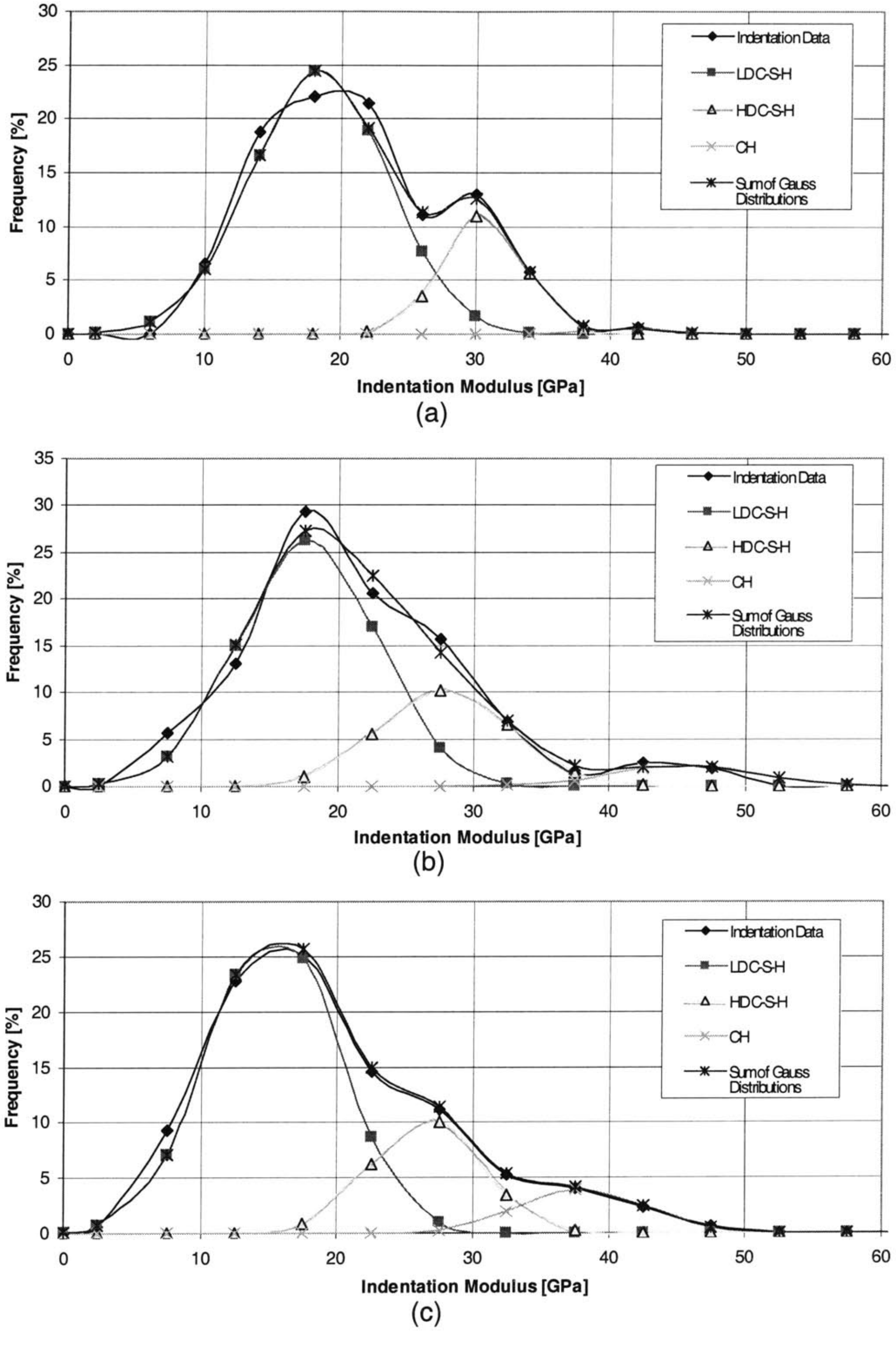

Figure 6-8: Nanoindentation indentation modulus frequency distribution with gaussian distributions fit to each phase for samples heated to (a) 105°C, (b) 200°C, (c) 300°C.

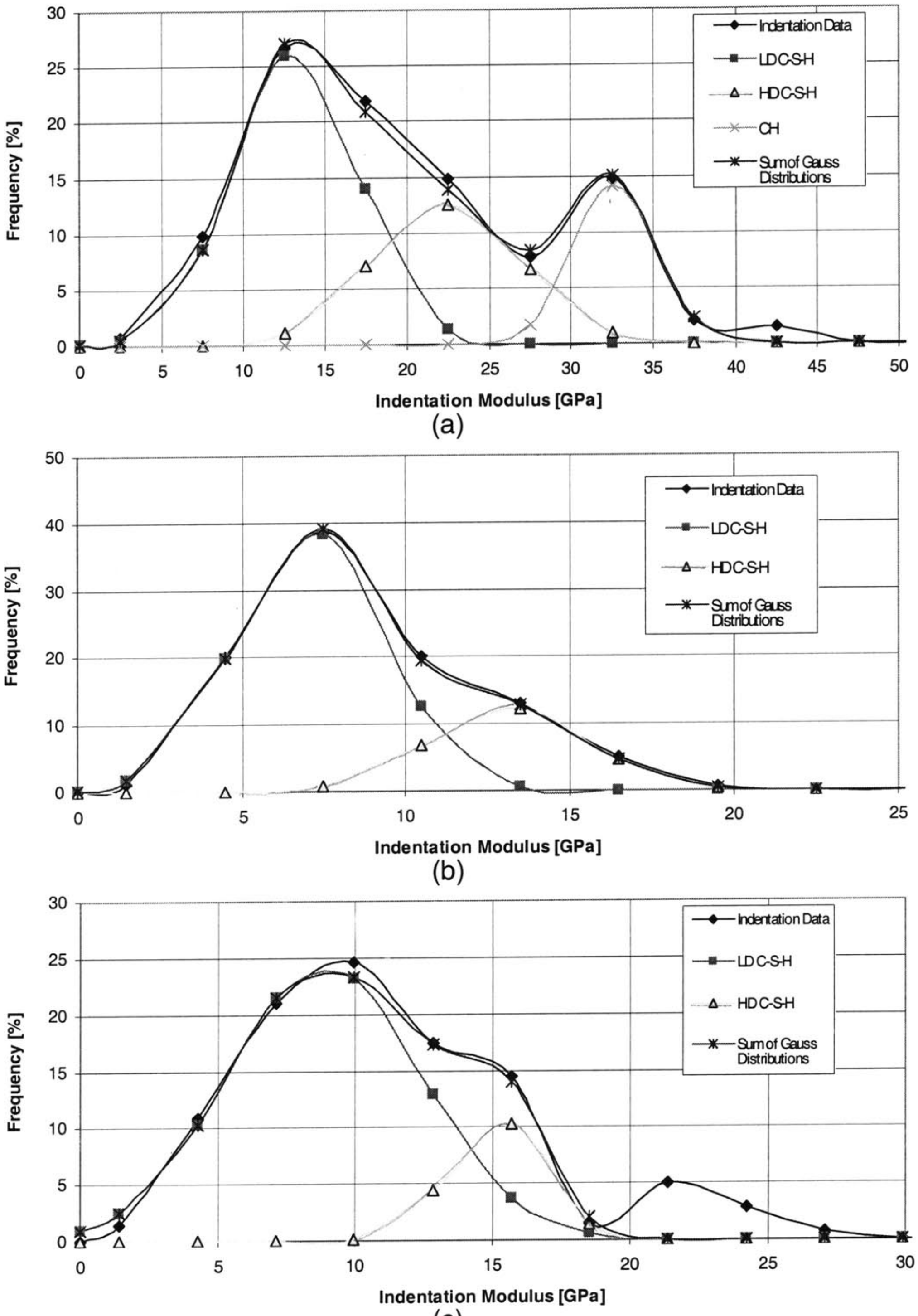

(a)

(b)

(c)

Figure 6-9: Nanoindentation indentation modulus frequency distribution with gaussian distributions fit to each phase for samples heated to (a) 400°C, (b) 550°C, (c) 700°C.

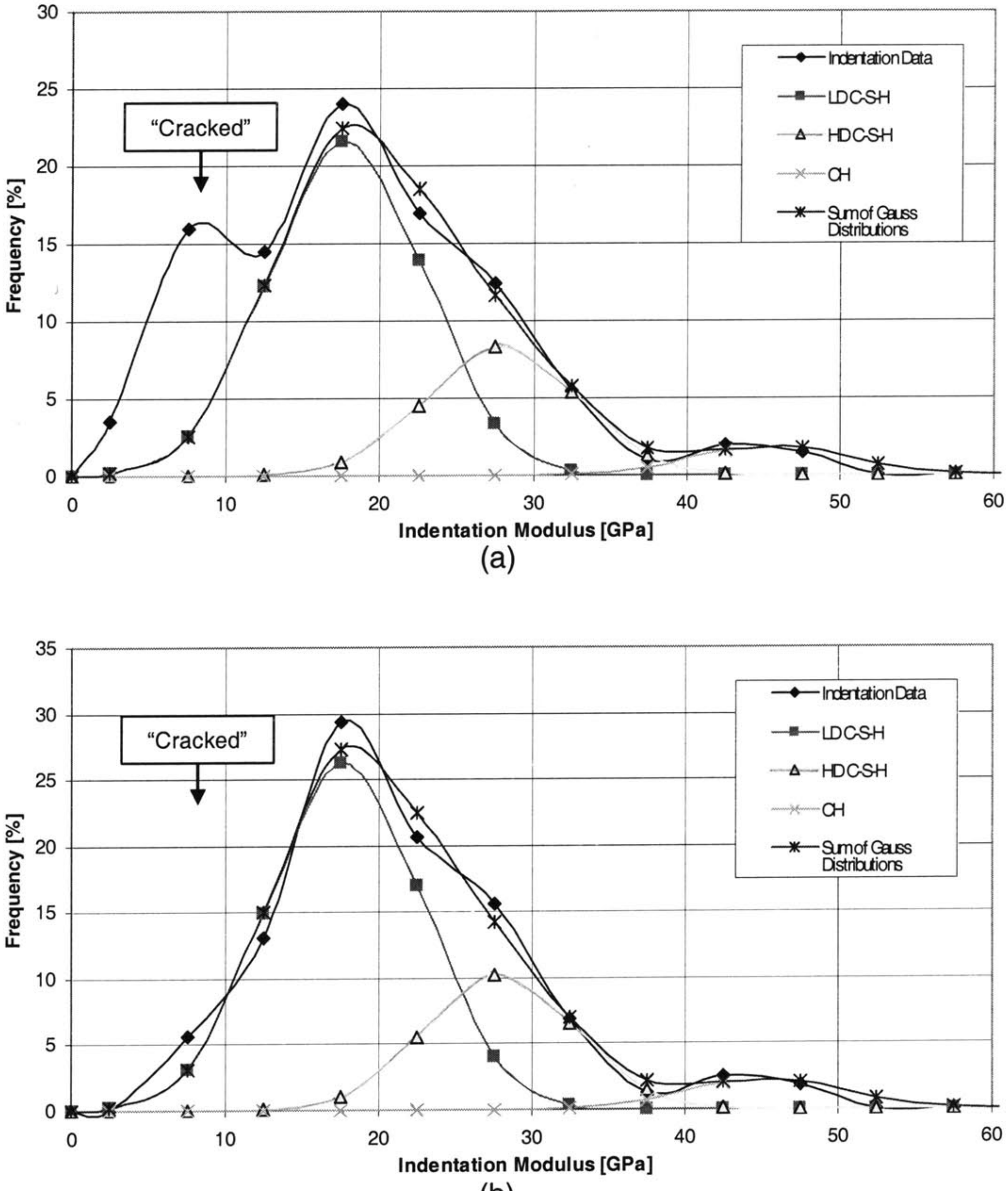

(a)

(b)

Figure 6-10: Nanoindentation indentation modulus frequency distribution with gaussian distributions fit to each phase for samples heated to 200^{o}C: (a) raw data, (b) discontinuous data eliminated.

Temp.	**Indentation Modulus** [GPa]			**Volume Fraction** [%]			**C-S-H** [%]	
[^{o}C]	**LD C-S-H**	**HD C-S-H**	**CH**	**LD C-S-H**	**HD C-S-H**	**CH**	**LD**	**HD**
25	19.2	32.4	39.5	73	17	8	81	19
105	18.4	30.5	-	77	21	-	79	21
200	17.8	27.9	45.4	66	25	6	72	28
300	15.3	26.5	38.0	66	21	9	76	24
400	13.2	22.4	32.7	50	28	18	64	36
550	7.1	13.1	-	73	25	-	75	25
700	8.9	15.1	-	75	16	-	82	18
						Average:	75.6	24.4

Table 6.2: Indentation modulus and volume fraction of each phase determined from nanoindentation indentation modulus frequency distributons.

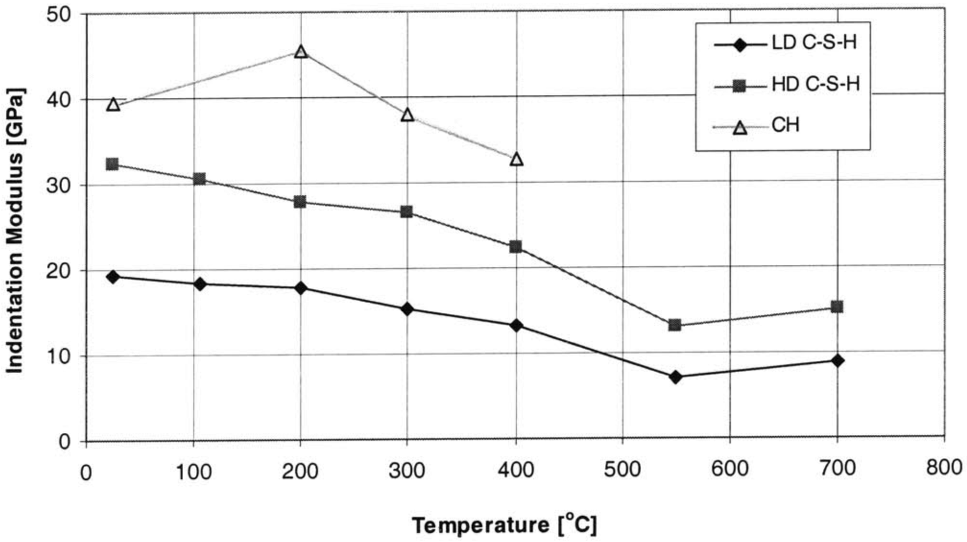

Figure 6-11: Nanoindentation indentation modulus results for each phase of cement paste heated to various temperatures.

frequency distributions, were plotted (see Fig. 6-12(c)). This plot indicates the large variation in hardness, but provides a valuable method of determining the approximate hardness of each phase. Comparison of Figure 6-12(b) and Figure 6-12(c) indicates that the fitting method was effective. The hardness gaussian distributions of each phase correspond well with the hardness frequency distributions derived from elasticity results. This method of verifying the hardness fitting results was used for all temperatures of investigation.

Hardness frequency distributions with fitted gaussian distributions for all heated samples are displayed in Figures 6-13 and 6-14. From these hardness frequency distributions, the mean hardness values of each phase were determined and are shown in Table 6.3. Additionally, the hardness of each phase is plotted with respect to temperature in Figure 6-15.

6.6 Discussion of Phase Properties

The results of nanoindentation provide critical information regarding the evolution of the microstructure of cement paste after high temperature exposure. Using this new data along with data in the literature, a more comprehensive evaluation of the effects of high temperatures on cement paste is possible. First, the results from unheated samples (25°C) will be discussed and compared with existing data. Second, the effects of temperature on the modulus of elasticity and hardness will be compared with existing data in order to determine changes in the cement paste microstructure. Third, the volume fractions of the individual phases will be investigated.

6.6.1 Phase Properties of Unheated Samples

Results of the current investigation are compared with results in the literature in Table 6.4. Both elasticity and hardness results compare quite well for all three phases investigated. Each phase will now be discussed separately.

- **LD C-S-H:** The LD C-S-H elasticity result is slightly lower than previous results on OPC [12], but slightly higher than previous results on white cement paste [15]. The fact that elasticity results were slightly lower than previous results on OPC can be attributed to the shorter curing period used in this investigation. A shorter curing period leads to increased capillary porosity which would affect the LD C-S-H phase more than the other

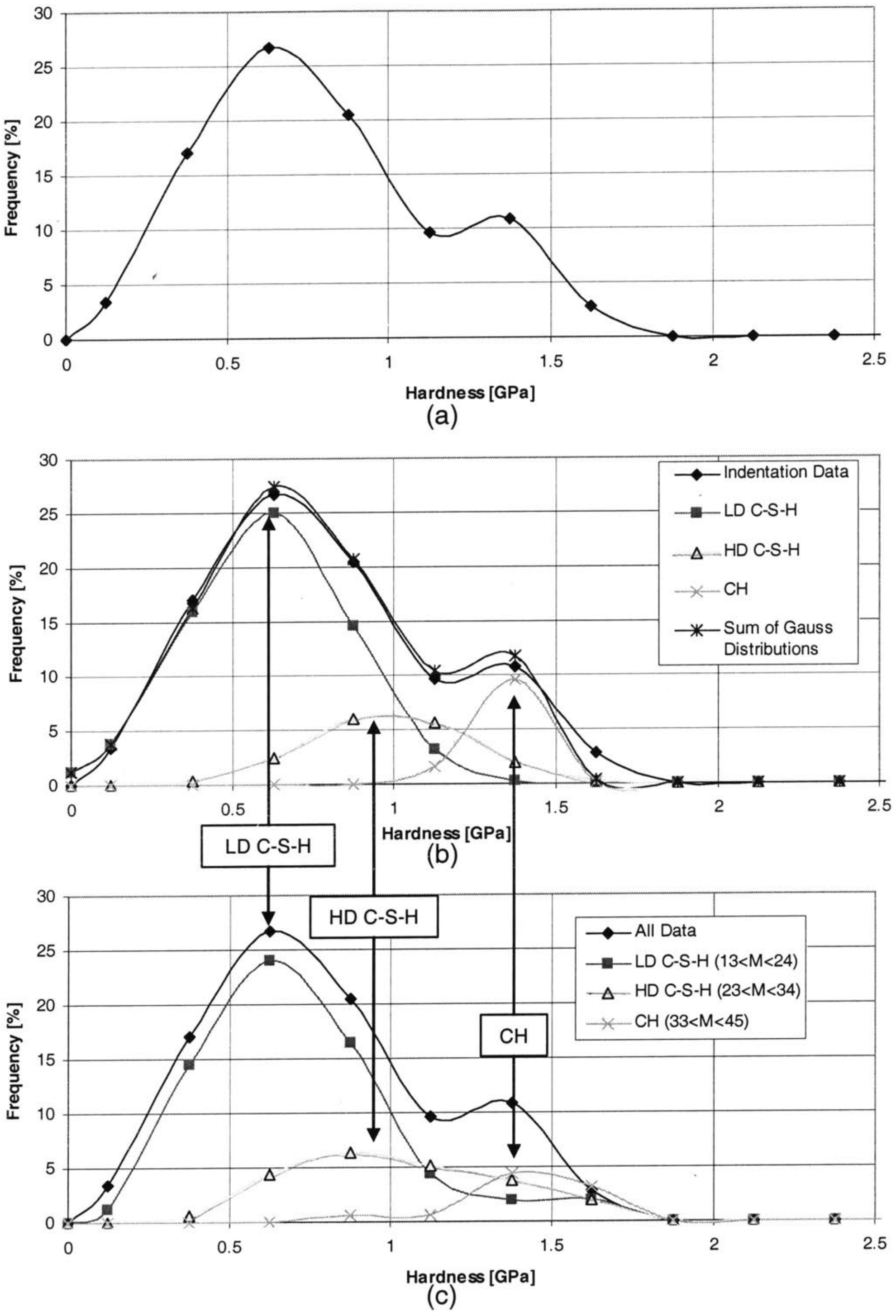

Figure 6-12: Nanoindentation hardness results for unheated samples (25^{o}C): (a) frequency distribution only, (b) frequency distribution for all data and each phase as determined by indentation modulus results, (c) frequency distribution with gaussian distributions fit to each phase.

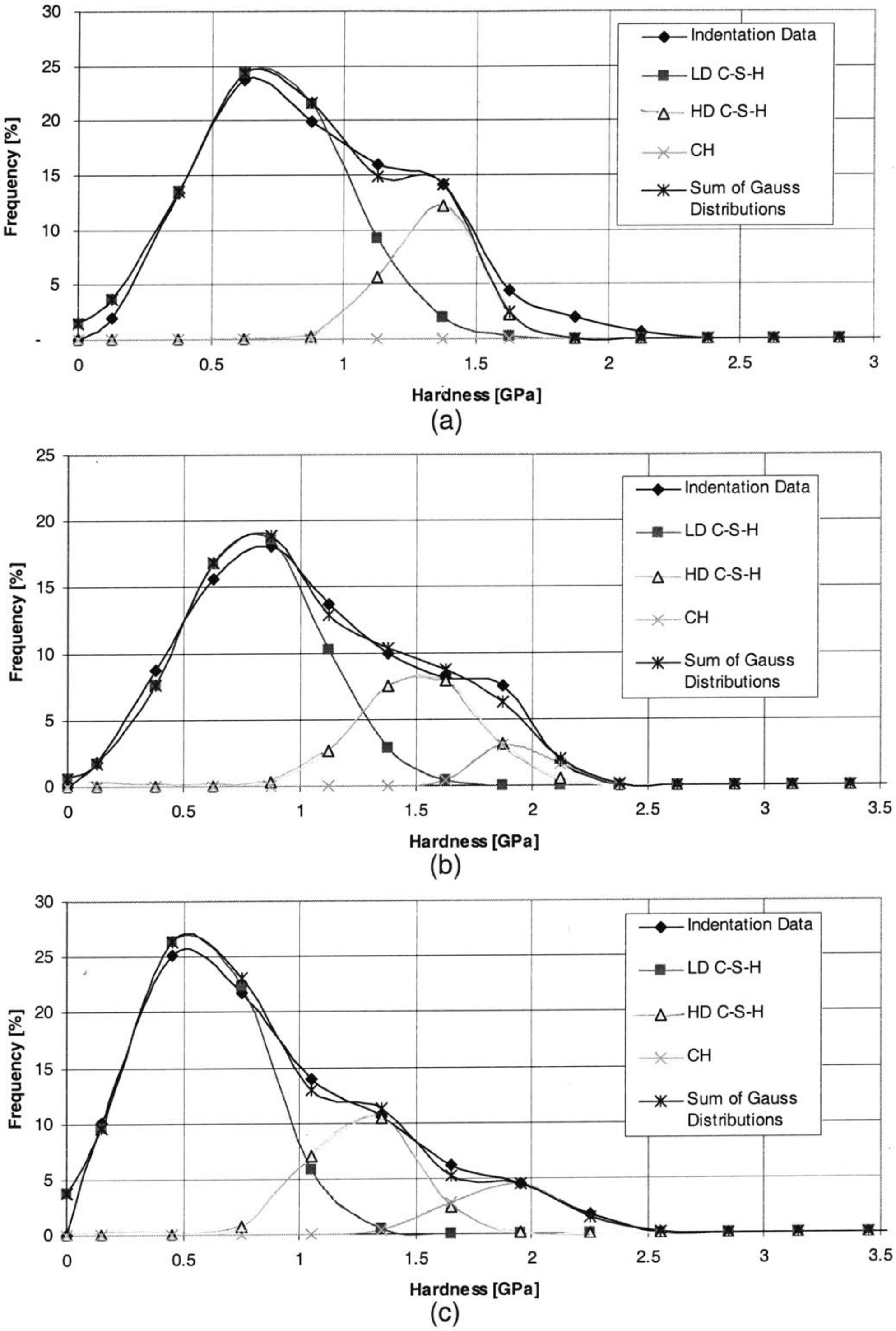

(a)

(b)

(c)

Figure 6-13: Nanoindentation hardness frequency distribution with gaussian distributions fit to each phase for samples heated to (a) 105°C, (b) 200°C, (c) 300°C.

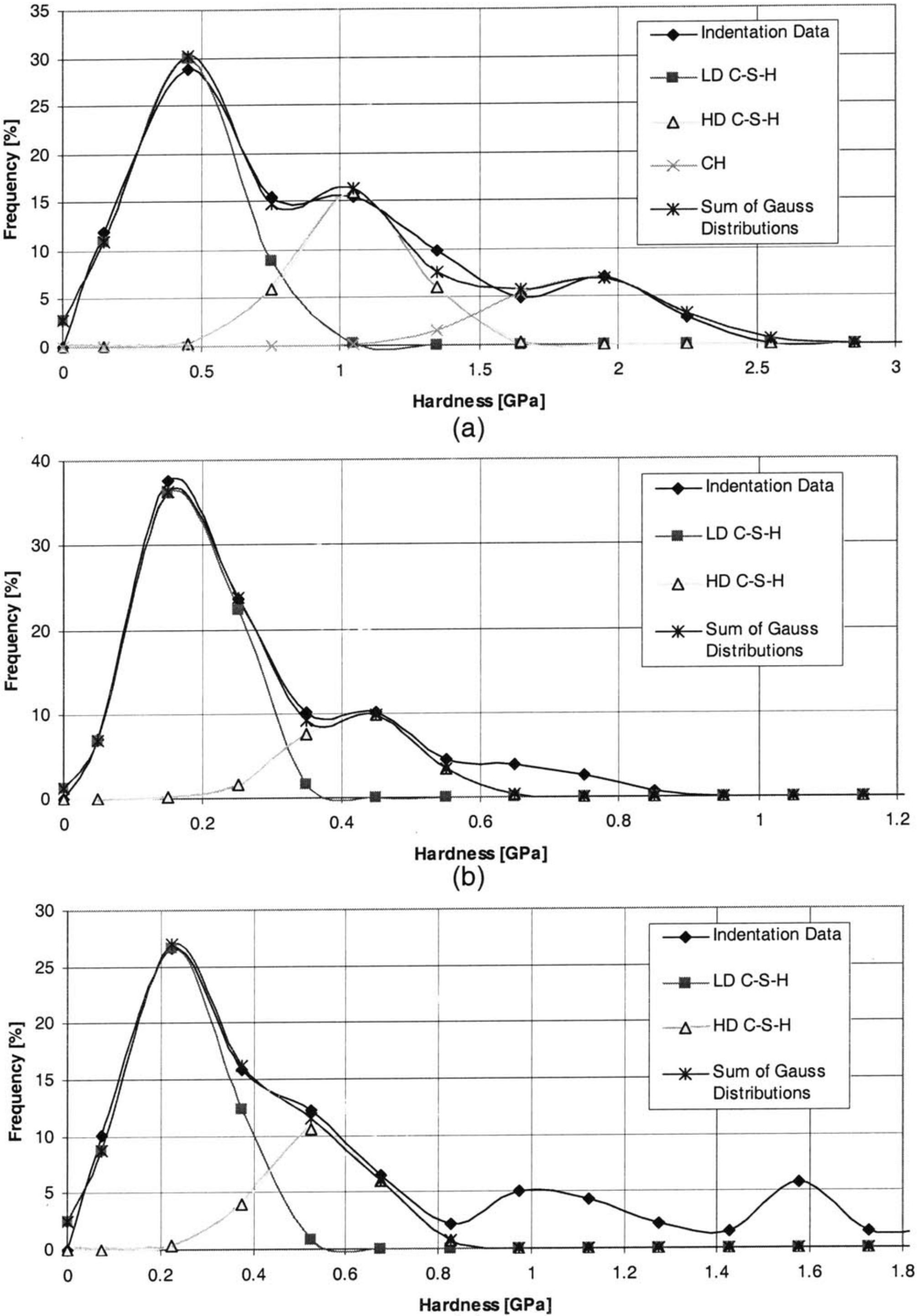

(a)

(b)

(c)

Figure 6-14: Nanoindentation hardness frequency distribution with gaussian distributions fit to each phase for samples heated to (a) 400°C, (b) 550°C, (c) 700°C.

Temperature	**Hardness** [GPa]		
[^oC]	**LD C-S-H**	**HD C-S-H**	**CH**
25	0.61	0.98	1.32
105	0.71	1.33	-
200	0.79	1.51	1.94
300	0.56	1.26	1.94
400	0.44	1.05	1.87
550	0.18	0.42	-
700	0.24	0.55	-

Table 6.3: Hardness of each phase determined from nanoindentation hardness frequency distributons.

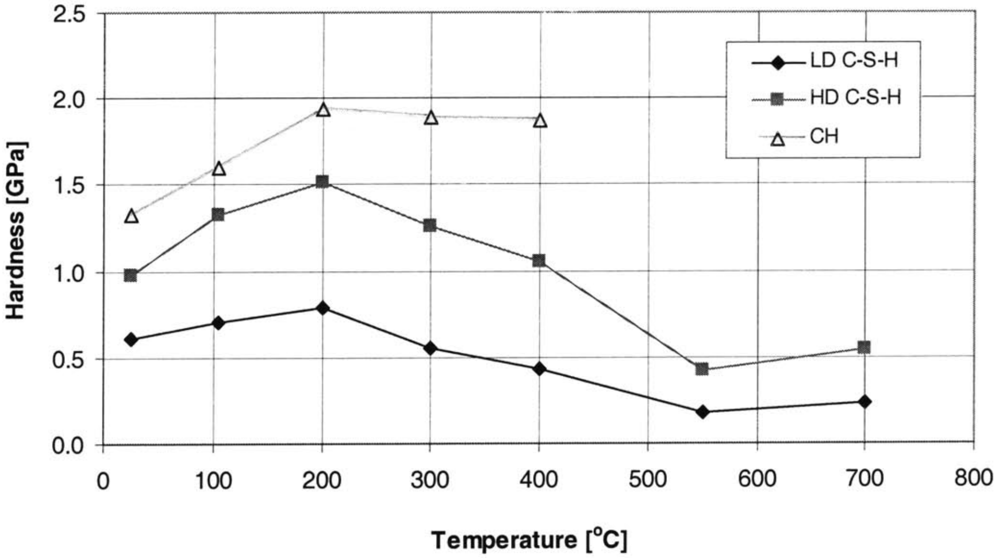

Figure 6-15: Nanoindentation hardness results for each phase of cement paste heated to various temperatures.

Phase	E [GPa]	H [GPa]	**Reference**
LD C-S-H	21.7±2.2		Constantinides [12]
	20±2		Acker [1]
	17.7 ± 5.0	0.45 ± 0.17	Constantinides [15]*
	18.1 ± 4.6	*0.61 ± 0.26*	*Current Investigation*
HD C-S-H	29.4 ± 2.4		Constantinides [12]
	31 ± 4		Acker [1]
	28.9 ± 2.8	0.86 ± 0.19	Constantinides [15]*
	30.6 ± 3.8	*0.98 ± 0.22*	*Current Investigation*
CH	38 ± 5		Constantinides [12]
	36 ± 3	1.35 ± 0.5	Acker [1]
	36.9 ± 2.5	1.23 ± 0.14	Constantinides [15]*
	37.3 ± 3.5	*1.32 ± 0.25*	*Current Investigation*

*Results from investigation of white cement paste.

Table 6.4: Comparison of results with results in the literature for unheated cement paste.

phases. The fact that the results of Constantinides [15] on white cement paste are lower than all other results is quite interesting. The primary difference between white cement paste and OPC paste is that white cement paste contains a much smaller volume fraction of aluminate and ferrite phases. Additionally, several investigators have reported that hydrated aluminate and ferrite phases are present within the outer (LD) C-S-H phase [52]. Therefore, hydrated aluminate and ferrite phases seem to stiffen the LD C-S-H phase slightly. This result is logical because hydrated aluminate and ferrite have a higher density [53] and are more crystalline in nature [52] than the C-S-H phases.

The LD C-S-H hardness result of this study is of the same order of magnitude as the results of Constantinides [15], but still somewhat higher. Again, the difference can be attributed to the presence of aluminate and ferrite phases within the LD C-S-H, but the effect of these minor phases is greater on the hardness than the elasticity. The source of the hardness increase can not be determined conclusively, but a discussion of the relation between packing density and hardness, which is related to the compressive strength, might be useful. If one assumes that LD C-S-H can be modelled as a granular solid with spherical grains (see Section 2.2.1), then the number of contact points of each grain, N, can be related to the hardness or strength of the material. Also, as mentioned in Section 2.2.1, the LD C-S-H gel porosity ($\phi_{LD} = 0.37$) comes close to the maximum *random* packing limit of monosized spheres, in which each sphere has six contact points ($N = 6$). The white cement tested by Constantinides [15] would have pure LD C-S-H phases, and would therefore correspond to the low-density packing limit. However, the results of this investigation on Type I OPC indicate that the introduction of aluminate and ferrite phases within the LD C-S-H increases the hardness. This is logical and can be easily explained with the granular solid model in mind. Introducing smaller spheres within a matrix of larger spheres would increase the packing density and number of contacts, and therefore increase the hardness. The idea of packing density will be further discussed in Chapter 8.

- **HD C-S-H:** The HD C-S-H elasticity results compare well with the results of Acker [1], and are slightly higher than the results of Constantinides on both Type I OPC [12] and white cement paste [15]. Although the difference in results is small, it might be explained by the inherent spatial proximity of HD C-S-H to clinker grains. HD C-S-H is not randomly distributed throughout the material matrix, it is necessarily located adjacent to clinker grains by its formation process (see Section 2.2.2). Therefore, if clinker grains are still present, they could have an effect on the measurement of the HD C-S-H elasticity. The results of Acker were obtained by testing Ductal, an ultra high performance mortar with an extremely low w/c ratio and therefore a large volume fraction of unhydrated clinker. The results of this investigation were obtained by testing normal cement paste which was cured for only 28 days, also resulting in the presence of unhydrated clinker at the time of testing. The results of Constantinides, on the other hand, were obtained by testing well-hydrated cement pastes with almost no clinker present at the time of testing. Based on these three investigations, it seems that unhydrated clinker does have a small effect on the measurement of the elastic modulus of HD C-S-H when using nanoindentation.

  The HD C-S-H hardness results are again of the same order of magnitude as the results of Constantinides [15], but again slightly higher. The difference correlates with the difference in elasticity, and can also be explained by the effect of unhydrated clinker on the measurement of the HD C-S-H phase properties. A secondary effect causing increased hardness could be the presence of hydrated aluminate and ferrite phases within the HD

C-S-H. However, although the presence of hydrated aluminate and ferrite phases within LD C-S-H is certain, their existence within HD C-S-H is still debated [52]. Additionally, even if these minor phases are present within HD C-S-H, they have only been observed in very small amounts and would therefore have little effect on the HD C-S-H phase properties.

- **CH:** The CH hardness and elasticity results compare remarkably well with other investigations (see Table 6.4). It is worth noting that Acker [1] located and indented directly on CH crystals to determine their properties. On the other hand, grid indentation was used in this investigation and by Constantinides [12]. Both methods yield similar results.

6.6.2 Effects of Temperature on the Modulus of Elasticity

The evolution of the indentation modulus of each phase with respect to temperature exposure is displayed in Figure 6-11. By inspection, both the LD C-S-H and HD C-S-H elasticities evolve similarly when exposed to high temperatures. This supports the idea of the existence of one basic building block composing each C-S-H phases [33]. If both phases are composed of the same basic building block, then that building block will be similarly affected by temperature regardless of the packing density. Additionally, changes in the packing densities would be a result of the same effects on the basic building block, so the packing densities (gel porosities) would most likely evolve similarly. The evolution of the elasticity of the C-S-H phases with respect to temperature will be discussed first, followed by a discussion of the effect of temperature on the elasticity of the CH phase.

- **C-S-H Phases:** The elasticity of both C-S-H phases decreased steadily but relatively slowly up to 300°C. In the same temperature range, MIP results show that the porosity increases only slightly up to 200°C and is basically constant between 200°C and 300°C (see Table 2.6). Therefore, because MIP porosity changes very little, it seems that the decrease in elasticity was a result of a change in the microstructure at a scale below the gel porosity, which MIP can not access. Regardless, the fact that MIP changed very little supports the nanoindentation results. For example, if MIP porosity results were to indicate that the gel porosity increases significantly, this would necessarily be seen in the nanoindentation results, and the results of this investigation would be contradictory.

Between 300°C and 400°C, nanoindentation results indicated that the elasticities of the C-S-H phases decrease slightly more rapidly. In the same temperature range, MIP results indicate that the gel porosity (<10 nm pore diameter) increases significantly (see Table 2.6). Therefore, in this temperature range, it seems that C-S-H dehydration at a smaller scale is beginning have an effect on the gel porosities. This effect is directly measured using MIP and is supported by nanoindentation results.

Between 400°C and 550°C, nanoindentation results indicate that the elasticities of the C-S-H phases decrease even more rapidly. MIP results indicate a continued increase in the gel porosity (<10 nm pore diameter) in this temperature range, but also an increase in larger pore diameters (40-100 nm pore diameter). This increase in larger pore diameters is most likely due to the decomposition of CH, but could also be a result of an increase in the average size of the gel pores. Regardless, the gel porosities clearly increase in this temperature range, as confirmed by both MIP and nanoindentation results. However, the possible effects of the CH decomposition in this temperature range can not be ignored. CH decomposition is accompanied by a large change in volume, which could have significant effects on the density and connectivity of the microstructure. Because of this, the C-S-H elasticity results might slightly underestimate the actual elasticity of the phases in this temperature range due to CH dehydration.

Between 550°C and 700°C, nanoindentation results indicate that the elasticities of the C-S-H phases remain relatively constant, and perhaps even increase slightly. This result is surprising, as continual degradation of the microstructure was expected with higher temperature exposure. Additionally, continual decrease in elasticity occurred at larger scales as indicated by microindentation results (see Fig. 5-6). However, MIP results indicate a significant increase in large pores (>100nm pore diameter), but no change in the smaller gel pores. This supports the possibility of the C-S-H elasticities remaining constant. Additionally, the increase in larger pores supports the continual decrease of elasticity measured at larger scales.

The increase in larger pores indicated by MIP could be a result of increased cracking, CH decomposition, and/or changes in morphology of the C-S-H (see Table 2.6). This temperature range also corresponds with the range of secondary C-S-H dehydration described by Harmathy [28] (see Fig. 2-1). Therefore, because chemical phase changes of the C-S-H could be occurring, the presence of LD and HD C-S-H are uncertain. Perhaps a third, fully dehydrated C-S-H phase is present, or the LD and HD C-S-H phases are present in another form. Regardless, possible C-S-H transformation allows the possibility of the elasticity of the C-S-H phases increasing. Lastly, an increase in larger pore diameters (>100 nm) could have a significant effect on the results of nanoindentation if the selected indentation depth (100-200 nm) was of the same order of magnitude as this pore size.

- **CH Phase:** The effect of high temperature exposure on the CH phase was difficult to determine because CH is present in a relatively small volume fraction, and is not distributed as well as the C-S-H phases. Nevertheless, the elasticity of the CH phase increased slightly up to 200^{o}C, and then decreased between 200^{o}C and 400^{o}C (see Fig. 6-11). This change was not expected because very little dehydration occurs in the CH phase up to 370^{o}C. However, initial heating could result in a more crystalline structure of the CH phase, which can be seen by the increase in elasticity up to 200^{o}C. The measured decrease in elasticity above 200^{o}C could be a result of the decreasing elasticity of the C-S-H matrix phase, which acts as the substrate in nanoindentation testing. The decrease in elasticity at 400^{o}C could also be a result of partial dehydration of CH at this temperature.

  At 550^{o}C and 700^{o}C, CH is fully dehydrated into CaO, which is known to be much stiffer in nature. However, detection of the CaO phase at 550^{o}C was not possible using nanoindentation. This was most likely due to the low elasticity of both C-S-H phases at this temperature. If one were to indent directly on CaO which was located on a much softer substrate (C-S-H matrix), the low elasticity of the substrate would dominate the result. This is especially true in this case where the connectivity of the material has been reduced by increased porosity and possible microcracking. It is interesting to note that a phase with higher stiffness is present at 700^{o}C (see Fig. 6-9(c)) which was not present at 550^{o}C (see Fig. 6-9(b)). Perhaps this is the dehydrated CaO phase, or possibly a transformed C-S-H phase as previously discussed.

6.6.3 Effects of Temperature on the Hardness

The evolution of the hardness of each phase with respect to temperature exposure is displayed in Figure 6-15. As with the elasticity, the hardness of both C-S-H phases evolved similarly. This again supports the idea of the same basic building block composing each C-S-H phase. The effect of high temperature exposure on the hardness of the C-S-H phases and the CH phase will now be discussed separately.

- **C-S-H Phases:** The hardness of both C-S-H phases increased steadily with exposure temperature up to 200°C, and then decreased steadily during temperature exposures between 200°C and 400°C. This result is similar to the results of microindentation, which also showed an initial increase in hardness followed by a continual decrease with temperature exposures above 300°C. The source of the initial increase is difficult to determine, but appears to be a result of both drying of the pore space and dehydration of C-S-H. MIP and nanoindentation elasticity results indicate that the gel porosity changes very little up to 300°C, so the initial increase in hardness appears to result from an increasing hardness within the basic building block. The hardness decreases more rapidly at 400°C and above, which supports the idea of increasing gel porosity in this temperature range. Recall the sphere packing model discussed in the Section 6.6.2. An increase in gel porosity would cause a decrease in the number of sphere contact points, and therefore a decrease in the hardness.

  Between 550°C and 700°C, it was again surprising that the hardness of both C-S-H phases remained relatively constant but even increased slightly. Again, MIP results indicate that the porosity and average pore diameter increase in the same temperature range. This would indicate that the connectivity of the microstructure is increasing while the porosity is also increasing. Again, this could be caused by a microstructural transformation during the secondary range of C-S-H dehydration.

- **CH Phase:** The hardness of the CH phase also increased up to 200°C, but then remained relatively constant until decomposing above 400°C (see Fig. 6-15). The initial increase again supports the possibility of CH becoming more crystalline, as discussed in Section 6.6.2.

At 550°C, when CH is fully dehydrated, results were similar to the elasticity results and a harder CaO phase was barely detectable. At 700°C, however, the hardness frequency distribution (see Fig. 6-14(c)) clearly shows the presence of a harder phase or phases that were not detected at 550°C (see Fig. 6-14(b)). Two possible explanations for the presence of these harder phases are:

1. The harder phases formed between 550°C and 700°C as a result of the secondary range of C-S-H dehydration which caused a microstructural transformation.
2. The connectivity of the microstructure increased from 550°C to 700°C, allowing the detection of these harder phases. So these harder phases, perhaps CaO, were present at 550°C, but were not detected because the overall microstructure was more disconnected and degraded. In other words, the weak substrate dominated the results, and the harder phases could not be detected.

Regardless, the higher hardness values (>1.0 GPa) measured at 700°C are not necessarily representative of the actual hardness of these harder phases. The 'substrate effect' would cause these higher hardness values to be underestimated. Furthermore, the 'substrate effect' would also cause a large scatter in the hardness results, so the number of harder phases present is also uncertain.

6.6.4 Phase Volume Fractions

One of the most significant results of nanoindentation was the determination of the volume fractions of the various phases. The relative volume fractions of the C-S-H phases will be discussed first, followed by the volume fraction of the CH phase.

- **C-S-H Phases:** Of special interest is the relative volume fractions of the C-S-H phases for comparison with other studies. Additionally, the relative percentages of C-S-H are the most accurate volume fraction measurements available. This is due to the formation process discussed in Section 2.2.2. Because LD and HD C-S-H form as an inner and outer product, they are very well distributed throughout the cement paste. This lends itself very well to statistical grid indentation, which depends on random, well-distributed phases for accurate results.

The indentation modulus frequency distribution results (see Table 6.2) show initial relative percentages for LD C-S-H and HD C-S-H of 81% and 19% respectively. These results confirm the fact that LD C-S-H dominates the C-S-H matrix phase for a w/c ratio of 0.5. Furthermore, they compare reasonably well with the results of Constantinides [12], who found relative LD C-S-H and HD C-S-H percentages of 70% and 30%, respectively. The difference in results could be due to the shorter curing time used in this investigation. The initial results also compare reasonably well with the hydration model of Jennings [33], who also estimates the relative volume fractions of LD C-S-H and HD C-S-H to be approximately 70% and 30%, respectively.

Now that the initial relative percentages of LD C-S-H and HD C-S-H seem logical, the evolution of the volume fractions with respect to temperature exposure must be explored. The indentation modulus frequency distribution results show little variation in relative volume fractions at all temperatures of investigation (see Table 6.2). The relative percentages of LD C-S-H and HD C-S-H generally remained in the ranges of 70-80% and 20-30%, respectively. As a result, it was concluded that the relative volume fraction of the C-S-H phases were unaffected by high temperature exposure. Accordingly, average relative volume fractions of all investigated temperatures were taken in order to best estimate the actual relative volume fractions present in the material. The average relative volume fractions were found to be approximately 75% LD C-S-H and 25% HD C-S-H (see Table 6.2). These values will be used in Part III for modeling.

The conclusion that the relative C-S-H volume fractions do not change when cement paste is exposed to high temperatures is significant when compared to previous investigation into the effects of heat curing. Constantinides [13] investigated the effects of heat curing on cement paste using nanoindentation, and determined that the relative HD C-S-H volume fraction increased with heat curing. Therefore, high temperature exposure *during* the formation of C-S-H increases the relative percentage of HD C-S-H, and therefore decreases the percentage of LD C-S-H. However, the results of this study indicated that high temperature exposure *after* the majority of C-S-H formation had occurred, had no effect on the relative C-S-H volume fractions. Therefore, *formation* of C-S-H is affected by high temperature exposure, but *transformation* of C-S-H from LD to HD due to high temperature exposure does not occur.

- **CH Phase:** The volume fraction of CH was also determined from indentation modulus frequency distributions, although it is a much more difficult value to obtain accurately. Contrary to C-S-H, CH crystals are not necessarily well-distributed, and also can be very large in size (see Section 2.2.2). These factors increase the variability in the volume fraction results when using the method of statistical grid indentation. Nevertheless, indentation modulus frequency distribution analysis yielded an initial CH volume fraction of 8%. This value is reasonable, considering the typical CH volume fraction in cement paste is approximately 10-15%.

  Exposure of cement paste to higher temperatures also had little effect on the volume fraction of CH. Based on indentation modulus frequency distribution results, one could argue that the volume fraction of CH increases with temperature exposure, especially after exposure to 400°C. However, this single result was more likely caused by a concentration of CH crystals in the area of the indentation grid, and is not enough to justify an increase in the volume fraction of CH due to high temperature exposure. As a result, the volume fraction of CH was determined to be constant as well. In order to best estimate the CH volume fraction, the average volume fraction of CH at all temperatures of investigation was taken and found to be approximately 11%. However, the CH volume fraction can also be estimated directly by use of the mix design and chemical reactions. This method will be applied and discussed in Chapter 8.

6.6.5 Verification of Results for Samples Heated to 550°C and 700°C

In order to verify the unexpected result that both the hardness and elasticity remain constant or even increase between 550°C and 700°C, new samples were tested at these temperatures. The new samples were cast at the same time as all other samples, but were allowed to cure for 3 months in lime water instead of 28 days. They were then prepared, heated, and tested using the same methods previously described. The new results were averaged with the initial results, and are shown in Figures 6-16 and 6-17.

The new results confirm the trends observed in the initial results, showing that both the

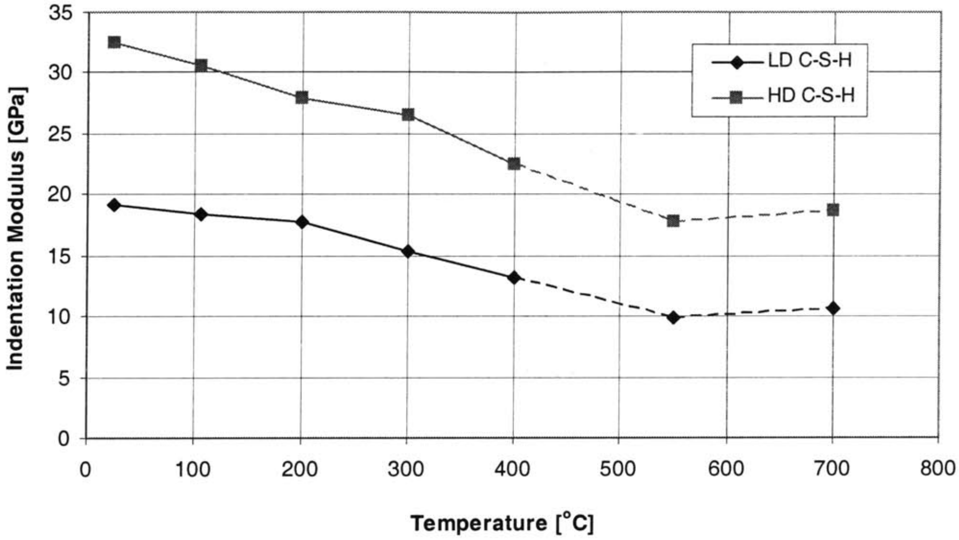

Figure 6-16: Nanoindentation indentation modulus results for the C-S-H phases of cement paste heated to various temperatures. Results revised at 550°C and 700°C.

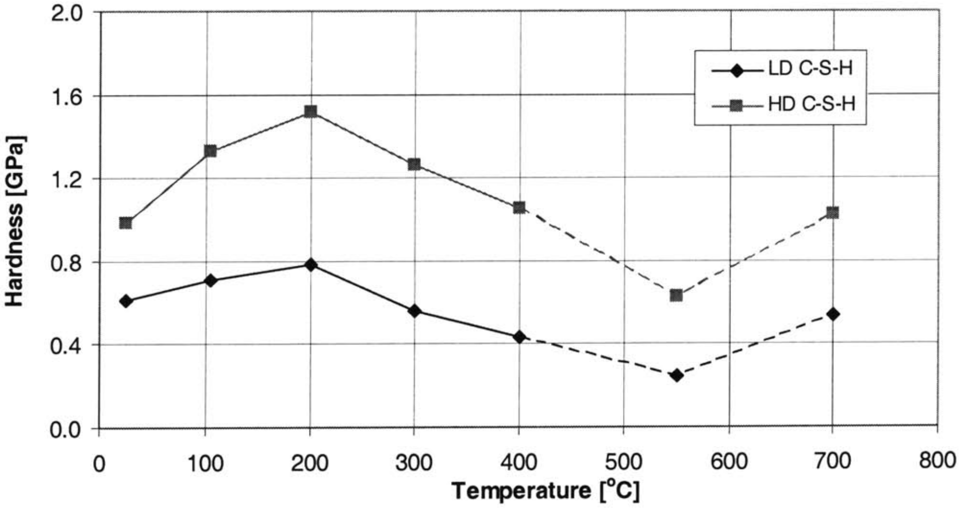

Figure 6-17: Nanoindentation hardness results for the C-S-H phases of cement paste heated to various temperatures. Results revised at 550°C and 700°C.

hardness and elasticity of both C-S-H phases remain relatively constant or even increase between 550°C and 700°C. Furthermore, the new results were slightly higher than the original results, which can only be explained by a longer curing period. A longer curing period results in a significantly reduced capillary porosity, as was seen in the results of microindentation. The reduction of capillary porosity would decrease the 'substrate effect', especially at higher temperatures where the microstructure is more porous and disconnected.

These new results confirm the conclusions drawn earlier in this section regarding these higher temperatures. The porosity increases (as shown by MIP results), as do the elasticity and hardness. This can be explained by a rearrangement of the microstructure, perhaps caused by a microstructural transformation of C-S-H during the secondary period of C-S-H dehydration.

6.7 Summary and Conclusions of Nanoindentation

Nanoindentation has been previously used to access the phase properties of cement paste at 'Level I' of the multiscale microstructure, but this investigation marks the first attempt at determining the effects of high temperature exposure on these phases. The following summarizes the conclusions drawn from this investigation.

- **General Results:** Disregarding the fact that different phases were present at the scale of investigation, the general results showed similar evolutions of the elasticity and hardness with respect to temperature as the results of microindentation. However, the standard deviations clearly indicate that assuming only one phase is present is insufficient for meaningful interpretation of the results. Meaningful interpretation requires evaluation of the phase properties.

- **Frequency Distributions:** The fitting method introduced in Section 6.4 provided an effective means of estimating the phase properties at each temperature of investigation. It must be noted that the statistical method used is only a method of *estimation*, but provided results which compare remarkably well with results on unheated cement paste in the literature.

- **Volume Fractions:** For a cement paste with $w/c = 0.5$, the relative percentages of LD C-S-H and HD C-S-H were found to be 75% and 25%, respectively, and were unaffected by high temperature exposure. In other words, high temperature exposure *after curing* does not cause a transformation from one type of C-S-H to the other. Therefore, changing the w/c ratio would change the initial relative percentages of LD and HD C-S-H, but these relative percentages would remain constant regardless of temperature exposure.

- **Elasticity:** The effects of high temperature exposure on the elasticity of the phases of cement paste at 'Level I' were successfully determined. Furthermore, because high temperature elasticity degradation of both types of C-S-H was observed at 'Level I', the source of this degradation must exist at a smaller scale ('Level 0').

- **Hardness:** The effects of high temperature exposure on the hardness of the phases of cement paste at 'Level I' were successfully determined. Hardness results compare well with the results of microindentation, confirming that the hardness increases with the initial loss of water due to evaporation and dehydration. Porosity has a significant effect on hardness, as indicated by the fact that the hardness decreased significantly in the temperature ranges where MIP shows that the gel porosities increase.

- **Evidence of a Single Basic Building Block:** The fact that the hardness and elasticity of both types of C-S-H evolve similarly with respect to temperature exposure supports the idea that C-S-H is formed by different packing densities of the same basic building block. The existence of one building block will be further investigated using microporoelastic modeling in the following chapters.

In conclusion, nanoindentation was successfully used to evaluate the effects of high temperature exposure on the phases of cement paste at 'Level I' of the multiscale microstructure. Clearly, C-S-H dehydration and CH decomposition both contribute to high temperature degradation at this scale. Results indicate that high temperature degradation occurs at an even smaller scale which is not yet accessible experimentally. As a result, microporoelastic modeling will be used in the following chapters to better pinpoint the sources of this high temperature degradation.

Part III

Microporoelastic Modeling

Chapter 7

Multiscale Microporoelastic Modeling

The previous chapters have clearly established that cementitious materials are complex heterogeneous materials, made up of several phases that manifest themselves at various length scales. The multi-scale microstructure of cementitious materials was introduced in Chapter 2 in order to define the different scales that are present. Then, in Part II the mechanical properties of each scale were investigated and compared with previously published results. Now, a method of linking the results of the different length scales investigated is desired. More specifically, this part of this study will focus on linking the *elasticity* results of the investigated scales. In order to achieve this, elements of continuum micromechanics will be applied.

The goal of this chapter is to introduce two microelastic models based on two different homogenization schemes which will be applied to experimental results in Chapter 8. These microelastic models will be presented in their general form for application to multiphase materials, as well as in a more specific form applying to porous materials with a single solid phase.

7.1 Introduction

The underlying idea of continuum micromechanics is that it is possible to separate heterogeneous materials into homogeneous phases. In other words, heterogeneous materials are assumed to be made up of various phases with on-average constant material properties. With knowledge of the material properties and spatial characteristics of each phase, these phases can be homogenized to obtain the bulk properties of a heterogeneous material. This process is defined by the three critical elements of continuum micromechanics [56]:

1. *Representation:* Representation identifies and characterizes the homogeneous phases in a heterogenous material. This involves defining the on-average material properties, characteristic length scale, and morphology that *represent* each homogeneous phase.

2. *Localization:* Localization establishes a link between a stress or strain applied on the boundary of an entire heterogeneous material volume with the resulting *local* stress and strain in each homogeneous phase.

3. *Homogenization:* Linear homogenization is basically a volume averaging of the homogeneous phases in a heterogeneous material. The process delivers *homogenized* material properties using the individual phase mechanical properties, volume fractions, and morphologies.

Representation was the goal of the majority of this study so far. The phase properties, characteristic length scales, and morphologies of cement paste have been extensively discussed. However, in order to apply continuum micromechanics to the represented phases, methods of localization and homogenization are required. Ulm *et al.* applied both localization and homogenization successfully in their discussion of concrete as a poromechanics material [56]. Similar methods are used in this study below.

7.2 Localization & Homogenization

The multiscale microstructure separates cementitious materials into 'Levels' which define the homogeneous phases present at the corresponding length scale. Each of these 'Levels' can be considered a heterogeneous material to which localization theory can be applied. In other words, a representative material volume, V, consisting of the phases present at any given 'Level' can be defined, and a strain boundary condition applied to this representative material volume can be considered. This strain boundary condition is described by:

$$\underline{\xi}(\underline{x}) = \mathbf{E} \cdot \underline{x} \tag{7.1}$$

where $\underline{\xi}(\underline{x})$[1] is the microscopic displacement, $\mathbf{E}$ is the macroscopic boundary strain, and $\underline{x}$ is the microscopic position vector. Additionally, the microscopic strain in each phase, $\varepsilon(\underline{x})$, is linked to the macroscopic strain by a strain localization condition:

$$\varepsilon(\underline{x}) = \mathbb{A}(\underline{x}) : \mathbf{E} \tag{7.2}$$

where $\mathbb{A}(\underline{x})$ is the localization tensor. Assuming that each phase of the heterogeneous material is homogeneous, a linear strain concentration can be introduced for each phase, yielding:

$$\langle \varepsilon(\underline{x}) \rangle_{V_r} = \langle \mathbb{A}(\underline{x}) \rangle_{V_r} : \mathbf{E} \tag{7.3}$$

where $\langle y \rangle_{V_r} = \frac{1}{V_r} \int y(\mathbf{x}) dV_r$ represents the volume average of the quantity y over the volume V_r of phase r. Assuming each homogeneous phase is also isotropic:

$$\langle \mathbb{A}(\underline{x}) \rangle_{V_r} = A_r^v \mathbb{J} + A_r^d \mathbb{K} \tag{7.4}$$

where A_r^v and A_r^d are the phase volumetric and deviatoric strain localization coefficients, $\mathbb{J}$ is the volumetric part of the unit tensor $\mathbb{I}$, and $\mathbb{K} = \mathbb{I} - \mathbb{J}$ is the deviatoric part.

At this point, it is necessary to define the homogenization scheme that will be used in order to proceed. Such homogenization schemes provide estimates of the localization coefficients (A_r^v and A_r^d). Several homogenization schemes are available, the two most prominent ones being the Self-Consistent (SC) scheme [30] and the Mori-Tanaka (MT) scheme [39]. Both schemes are based on the assumption that heterogeneous materials can be modelled as ellipsoidal inclusions

---

[1] The following notation will be used throughout this chapter:
$\underline{z}$ = Vector.
$\mathbf{E}$ = Second order tensor.
$\mathbb{C}$ = forth order tensor.
$\mathbb{I}$ = Forth order identity tensor.
'$\cdot$' refers to scalar products, and single tensorial contractions.
':' refers to tensorial double contractions.

embedded in a 'reference medium'. Their difference, however, lies in the reference medium that is selected. The schemes are similar, but will now be presented separately.

7.2.1 Mori-Tanaka Scheme

The MT scheme defines a material in which there is a single dominant phase that is percolated throughout the microstructure. This phase acts as a matrix in which all other phases are embedded. As a result, the dominant phase is defined as the 'reference medium' itself. Clearly, this scheme is only effective if a dominant matrix phase exists. Because 'Level I' of the multiscale microstructure is dominated by the C-S-H matrix, the MT scheme can be used effectively and was initially chosen [56]. Furthermore, because of the random orientation and morphology of the inclusion phases in the microstructure of cement paste, it is natural to assume that the phases represent inclusions that are both isotropic and spherical.

Using the assumption that all phases are isotropic, the stiffness tensor of the dominant phase, $\mathbb{C}_0$, and the stiffness tensor of the other phases, $\mathbb{C}_r$, are defined as:

$$\begin{aligned} \mathbb{C}_0 &= 3k_0\,\mathbb{J} + 2g_0\,\mathbb{K} &\quad (7.5) \\ \mathbb{C}_r &= 3k_r\,\mathbb{J} + 2g_r\,\mathbb{K} &\quad (7.6) \end{aligned}$$

where k_0 and g_0 are the bulk modulus and shear modulus of the dominant phase, and k_r and g_r and the are the bulk modulus and shear modulus of the other phases. Additionally, based on the assumption of spherical inclusions, an estimate A_r^{est} of the localization tensor $\langle \mathbb{A}(\underline{x}) \rangle_{V_r}$ (see Eq. (7.4)) is given by:

$$A_r^{est} = \left[\mathbb{I} + \mathbb{S}_r^{Esh} : \left(\mathbb{C}_0^{-1} : \mathbb{C}_r - \mathbb{I}\right)\right]^{-1} : \left\langle \left[\mathbb{I} + \mathbb{S}_r^{Esh} : \left(\mathbb{C}_0^{-1} : \mathbb{C}_r - \mathbb{I}\right)\right]^{-1} \right\rangle_V^{-1} \tag{7.7}$$

where the so-called Eshelby tensor [21], $\mathbb{S}_r^{Esh}$, is defined by:

$$\mathbb{S}_r^{Esh} = \alpha_0\,\mathbb{J} + \beta_0\,\mathbb{K} \tag{7.8}$$

where:

$$\alpha_0 = \frac{3k_0}{3k_0 + 4g_0} \tag{7.9}$$

$$\beta_0 = \frac{6(k_0 + 2g_0)}{5(3k_0 + 4g_0)} \tag{7.10}$$

In this special case, the volumetric and deviatoric strain localization coefficients introduced in Eq. (7.4) can now be estimated by:

$$A_r^v = \left(1+\alpha_0\left(\frac{k_r}{k_0}-1\right)\right)^{-1}\left[\sum_r f_r\left(1+\alpha_0\left(\frac{k_r}{k_0}-1\right)\right)^{-1}\right]^{-1} \tag{7.11}$$

$$A_r^d = \left(1+\beta_0\left(\frac{g_r}{g_0}-1\right)\right)^{-1}\left[\sum_r f_r\left(1+\beta_0\left(\frac{g_r}{g_0}-1\right)\right)^{-1}\right]^{-1} \tag{7.12}$$

where $f_r = \frac{V_r}{V}$ represents the volume fraction of each phase in the representative material volume, V.

At this point, localization of the strain in each phase has been achieved so homogenization is now possible. Calculation of the homogenized stiffness tensor, $\mathbb{C}_{hom}$, is possible using the standard expression of continuum micromechanics:

$$\mathbb{C}_{hom} = \langle \mathbb{C}(\underline{x}) : \mathbb{A}(\underline{x}) \rangle_V \tag{7.13}$$

Additionally, for drained conditions where a porous material is emptied of its fluid phase, the drained stiffness tensor is obtained:

$$\mathbb{C}_{hom} = \sum_{r=1}^{n} f_r \mathbb{C}_r : \langle \mathbb{A} \rangle_{V_r} \tag{7.14}$$

which, again assuming isotropy, can be expressed in the following form by substitution of Eqs. (7.4) and (7.5):

$$\mathbb{C}_{hom} = \sum_{r=1}^{n} f_r \left(3k_r \, \mathbb{J} + 2g_r \, \mathbb{K}\right) : \left(A_r^v \, \mathbb{J} + A_r^d \, \mathbb{K}\right) \tag{7.15}$$

As a result, the (drained) homogenized bulk and shear modulus can be obtained directly from:

$$K_{hom} = \sum_{r=1}^{n} f_r \, k_r \, A_r^v \tag{7.16}$$

$$G_{hom} = \sum_{r=1}^{n} f_r \, g_r \, A_r^d \tag{7.17}$$

and A_r^v and A_r^d are estimated using Eqs. (7.11) and (7.12). It is now useful to specify the relations which link the elastic properties, K and G, to the Young's Modulus, E, and Poisson ratio, v:

$$K = \frac{E}{3\,(1-2\nu)}; \; G = \frac{E}{2\,(1+\nu)} \tag{7.18}$$

Using these relations, the homogenized modulus of elasticity, E_{hom}, can be calculated:

$$E_{hom} = \frac{9G_{hom}}{\left(3 + \frac{G_{hom}}{K_{hom}}\right)} \tag{7.19}$$

As a result, the equivalent homogeneous elasticity of a heterogeneous material has been obtained.

7.2.2 Self-Consistent Scheme

The SC scheme defines a polycrystalline microstructure in which no phase acts as a matrix in which all other phases are embedded. Because no phase acts as a dominant reference medium, the SC scheme defines the reference medium as the homogenized medium itself. In other words, each phase acts as an inclusion that is embedded in a medium which is the homogenization of all phases, including itself. As a result, the SC scheme is clearly more effective if no dominant phase exists. Additionally, it can be more accurate if a dominant phase does exist, but does not act as a matrix in which all other phases are embedded.

The derivation of the SC scheme is similar to that of the MT scheme, except the reference medium is different. An estimate A_r^{est} of the localization tensor $\langle \mathbb{A}(\underline{x}) \rangle_{V_r}$ can still be obtained from Eq. (7.7), and the Eshelby tensor within each phase is still defined by Eq. (7.8):

$$\mathbb{S}_r^{Esh} = \alpha_{hom} \, \mathbb{J} + \beta_{hom} \, \mathbb{K} \tag{7.20}$$

but the coefficients α_{hom} and β_{hom} are now defined by:

$$\alpha_{hom} = \frac{3K_{hom}}{3K_{hom} + 4G_{hom}} \tag{7.21}$$

$$\beta_{hom} = \frac{6(K_{hom} + 2G_{hom})}{5(3K_{hom} + 4G_{hom})} \tag{7.22}$$

where K_{hom} and G_{hom} are the bulk modulus and shear modulus of the homogenized material itself. The volumetric and deviatoric strain localization coefficients can now be estimated by:

$$A_r^v = \left(1 + \alpha_{hom}\left(\frac{k_r}{K_{hom}} - 1\right)\right)^{-1}\left[\sum_r f_r\left(1 + \alpha_{hom}\left(\frac{k_r}{K_{hom}} - 1\right)\right)^{-1}\right]^{-1} \tag{7.23}$$

$$A_r^d = \left(1 + \beta_{hom}\left(\frac{g_r}{G_{hom}} - 1\right)\right)^{-1}\left[\sum_r f_r\left(1 + \beta_{hom}\left(\frac{g_r}{G_{hom}} - 1\right)\right)^{-1}\right]^{-1} \tag{7.24}$$

where $f_r = \frac{V_r}{V}$ still represents the volume fraction of each phase in the representative material volume, V. The remainder of the derivation is the same as in the MT scheme, with the homogenized bulk and shear modulus defined by:

$$K_{hom} = \sum_{r=1}^{n} f_r\, k_r\, A_r^v \tag{7.25}$$

$$G_{hom} = \sum_{r=1}^{n} f_r\, g_r\, A_r^d \tag{7.26}$$

and the homogenized modulus of elasticity defined by:

$$E_{hom} = \frac{9G_{hom}}{\left(3 + \frac{G_{hom}}{K_{hom}}\right)} \tag{7.27}$$

Again, the equivalent homogeneous elasticity of a heterogeneous material has been obtained. However, evaluation of the homogenized elasticity is clearly more complicated using the SC scheme because the equations are nonlinear.

7.3 Porous Materials with a Single Solid Phase

Although homogenization at 'Level I' lends itself nicely to the MT scheme because of the dominant C-S-H matrix, the proper homogenization scheme at 'Level 0' is not as clear. The two phases that are present at 'Level 0' are the C-S-H globules and the gel porosities. These phases 'homogenize' to become LD C-S-H and HD C-S-H at 'Level I'. Therefore, both C-S-H phases consist of a single solid phase and a single porosity. Clearly the solid phase is dominant in both types of C-S-H ($\phi_{LD} = 0.37$, $\phi_{HD} = 0.24$), which indicates that the MT scheme might be more appropriate. However, the formation of both types of C-S-H by different packing densities of a single type of spherical C-S-H globule (see Section 2.2.2) would be better represented by the SC scheme. As a result, both schemes will be investigated in order to determine which scheme is more appropriate.

For porous materials with a single solid phase, the derivation of each scheme can be simplified significantly. Furthermore, since the indentation modulus of both C-S-H phases can be determined using nanoindentation, the homogenized elastic properties can be accessed. However, the solid and porous phase properties can not be determined experimentally. As a result, a 'downscaling' method is necessary instead of an upscaling method. In other words, the solid and porous phase properties need to be determined as a function of the homogenized properties. This is the goal of the following derivations.

7.3.1 Mori-Tanaka Scheme with a Single Solid Phase

If only one solid phase is present, it is obviously the dominant matrix phase that is assumed to be percolated throughout the material. The homogenized bulk modulus, K_{hom}, can be directly calculated from Eqs. (7.16) and (7.11):

$$K_{hom} = \frac{k_s\,(1-\phi_0)\,(1-\alpha_s)}{(1-\phi_0)\,(1-\alpha_s)+\phi_0} \tag{7.28}$$

where k_s is now the bulk modulus of of the single solid phase, and α_s is defined as:

$$\alpha_s = \frac{3k_s}{3k_s+4g_s} \tag{7.29}$$

where g_s is the shear modulus of the single solid phase. Combining (7.28) and (7.29) yields:

$$K_{hom} = \frac{4g_s k_s (1-\phi_0)}{4g_s + 3k_s\phi_0} \tag{7.30}$$

Similarly, the homogenized shear modulus, G_{hom}, can be calculated from Eqs. (7.17) and (7.12):

$$G_{hom} = \frac{g_s (1-\phi_0)(1-\beta_s)}{(1-\phi_0)(1-\beta_s)+\phi_0} \tag{7.31}$$

where β_s is now defined as:

$$\beta_s = \frac{6(k_s + 2g_s)}{5(3k_s + 4g_s)} \tag{7.32}$$

Combining (7.31) and (7.32) yields:

$$G_{hom} = g_s \frac{(1-\phi_0)(8g_s + 9k_s)}{6\phi_0 (2g_s + k_s) + 8g_s + 9k_s} \tag{7.33}$$

Now, recall the relationships between indentation modulus, modulus of elasticity, bulk modulus and shear modulus:

$$M_{hom} = \frac{E_{hom}}{1-\nu_{hom}^2} = 4G_{hom}\frac{3K_{hom}+G_{hom}}{3K_{hom}+4G_{hom}} \tag{7.34}$$

$$M_s = \frac{E_s}{1-\nu_s^2} = 4g_s\frac{3k_s+g_s}{3k_s+4g_s} \tag{7.35}$$

where M_{hom} and E_{hom}, and M_s and E_s, are the indentation modulus and modulus of elasticity of the homogenized medium and the solid phase, respectively. Using relations (7.34) and (7.35) in combination with Eqs. (7.30) and (7.33) yields:

$$\frac{M_{hom}}{M_s} = \frac{1}{2}\frac{(1-\phi_0)(7-5\nu_s)\left(-13\phi_0 + 2\phi_0\nu_s + 15\phi_0\nu_s^2 - 14 + 10\nu_s\right)}{(7-5\nu_s+5\phi_0+5\phi_0\nu_s)(-8\phi_0+10\phi_0\nu_s-7+5\nu_s)} \tag{7.36}$$

from which the indentation modulus of the solid phase can be directly determined:

$$M_s = \frac{2M_{hom}(7-5\nu_s+5\phi_0+5\phi_0\nu_s)(-8\phi_0+10\phi_0\nu_s-7+5\nu_s)}{(1-\phi_0)(7-5\nu_s)(-13\phi_0+2\phi_0\nu_s+15\phi_0\nu_s^2-14+10\nu_s)} = \frac{E_s}{1-\nu_s^2} \tag{7.37}$$

Now, the indentation modulus and/or the modulus of elasticity of the solid phase have been determined as a function of the homogenized indentation modulus, the porosity, and the

Poisson's ratio of the solid phase.

7.3.2 Self-Consistent Scheme with a Single Solid Phase

In the case of the SC scheme, if only one solid phase is present, the homogenized bulk and shear modulus can be written in the form:

$$K_{hom} = k_s\left(1-\frac{\phi_0}{1-\alpha_{hom}}\right) \quad (7.38)$$

$$G_{hom} = g_s\left(1-\frac{\phi_0}{1-\beta_{hom}}\right) \quad (7.39)$$

where α_{hom} and β_{hom} are defined by Eqs. (7.21) and (7.22). Continued derivation yields the following relationships:

$$\frac{K_{hom}}{k_s} = \frac{4G_{hom}(1-\phi_0)}{4G_{hom}+3k_s\phi_0} \quad (7.40)$$

$$\begin{aligned}\frac{G_{hom}}{g_s} &= \frac{1}{2}-\frac{5}{4}\phi_0-\frac{3}{16}r_s(3-\phi_0)+ \\ &\quad \frac{1}{16}\sqrt{\left(64-320\phi_0+400\phi_0^2+r_s\left(144-168\phi_0-120\phi_0^2\right)+r_s^2\left(81-54\phi_0+9\phi_0^2\right)\right)}\end{aligned} \quad (7.41)$$

where:

$$r_s = \frac{k_s}{g_s} = \frac{2(1+\nu_s)}{3(1-2\nu_s)} \quad (7.42)$$

Eqs. (7.40) and (7.41) yield the following relationship between the homogenized indentation modulus and the indentation modulus of the solid phase:

$$\frac{M_{hom}}{M_s} = \frac{G_{hom}}{4g_s}\frac{(3r_s+4)(12r_s+4G_{hom}/g_s-9r_s\phi_0)}{(3r_s+1)(3r_s+4G_{hom}/g_s)} \quad (7.43)$$

from which the indentation modulus of the solid phase can be directly determined:

$$M_s = \frac{4M_{hom}}{G_{hom}/g_s}\frac{(3r_s+1)(3r_s+4G_{hom}/g_s)}{(3r_s+4)(12r_s+4G_{hom}/g_s-9r_s\phi_0)} = \frac{E_s}{1-\nu_s^2} \quad (7.44)$$

Again, by substituting Eqs. (7.41) and (7.42) into (7.44), the properties of the solid phase have been determined as a function of the homogenized indentation modulus, the porosity, and

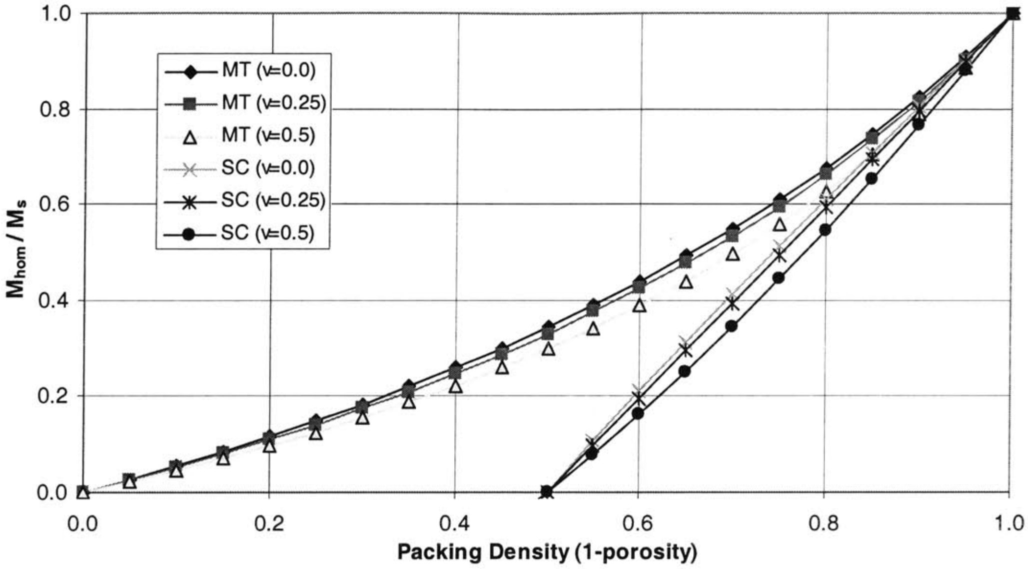

Figure 7-1: Relationship between M_{hom}/M_s and the packing density for the MT and SC schemes assuming three different Poisson's ratios for the solid phase ($\nu_s = 0.0, 0.25, 0.5$).

the Poisson's ratio of the solid phase.

7.3.3 Comparison of the Single Solid Phase Microelastic Models

In order to make an initial evaluation regarding which microelastic model more appropriately represents the two types of C-S-H, a comparison of the models is necessary. It is logical to start from Eqs. (7.36) and (7.43) which both define M_{hom}/M_s as a function of the porosity, ϕ_0, and the Poisson's ratio of the solid phase, ν_s, which is only defined between 0 and 0.5. Using these equations, M_{hom}/M_s was plotted with respect to the packing density $(1 - \phi_0)$ for both the MT and SC schemes (see Fig. 7-1). Three different values for Poisson's ratio were assumed ($\nu_s = 0, 0.25, 0.5$), but Figure 7-1 indicates that the Poisson's ratio has a relatively small effect on the results using either scheme.

As expected, both schemes predict that M_{hom}/M_s converges to one ($M_{hom} = M_s$) as the porosity approaches zero. However, the MT and SC scheme provide vastly different results at lower packing densities. In fact, the SC scheme predicts the homogenized stiffness, M_{hom}, to reach zero at a packing density of 0.5, while the MT scheme predicts that M_{hom} does not reach zero until a packing density of zero. Clearly, the MT scheme is only realistic at higher packing densities.

Assuming that both types of C-S-H are formed by different packing densities of a single type of spherical C-S-H globule, there would be a packing density threshold below which the homogenized stiffness would equal zero. The SC schemes predicts this packing density threshold, or 'percolation threshold', to be 0.5. However, the MT scheme predicts that the material would retain some homogenized stiffness at very low packing densities which is not logical. Recall that the MT scheme was derived based on the fact that spherical inclusions exist within a solid matrix. However, this is not the case at low packing densities when the volume fraction of the inclusions is larger than the volume fraction of the reference matrix. Therefore, the values predicted by the MT scheme are clearly not logical for low packing densities, but the accuracy of the MT scheme for higher packing densities remains in question.

7.4 Summary and Conclusions

Two methods of determining the homogenized modulus of elasticity of a heterogeneous material have now been presented, providing the key to linking the various scales of investigation. For example, using these homogenization methods, the homogenized modulus of elasticity of the C-S-H matrix can be obtained, E_{CSH}, and then used as an input for the C-S-H matrix phase to obtain the elastic modulus of 'Level II' of the multi-scale microstructure, E_{II}. Furthermore, if mortar ('Level III') was being investigated, the homogenized elastic modulus of 'Level II' (cement paste), E_{II}, could then be used as an input to find the homogenized modulus of elasticity of mortar, E_{III}, and so on. In this manner, a method of linking the scales of investigation, an 'upscaling method', has been obtained. This upscaling method will be used with the experimentally determined phase properties to compare the results of this high temperature investigation at various scales.

Furthermore, homogenization methods can also be used to estimate elastic properties at smaller scales. In the case of cement paste, since 'Level I' is the smallest scale at which elastic properties are experimentally accessible, the only available method of estimating elastic properties at 'Level 0' is reverse homogenization. For example, the experimentally determined elastic modulus of each type of C-S-H (E_{LD}, E_{HD}) can be used to determine the elastic modulus of the C-S-H globules (E_{glob}). As a result, a second method of linking scales of investigation, a 'downscaling method', has been obtained. This downscaling method will be used to estimate the effect of temperature exposure on the modulus of elasticity of the globules at 'Level 0'.

Chapter 8

Application of Microporoelastic Models to Experimental Results

With the microelastic models introduced in the previous chapter, the elastic properties of the phases present at each 'Level' of the multiscale microstructure can be linked. In other words, the elastic properties of the basic building block of C-S-H can be linked with the elastic properties of bulk cement paste through several iterations of homogenization. The 'Upscaling Tree' in Figure 8-1 provides a schematic diagram of how all of the phases present at various length scales can be linked. This diagram not only links the scales of investigation, it also defines all of the variables present in our upscaling model. Clearly, the model is dependent on the porosity (ϕ), modulus of elasticity (E), and phase volume fractions (f) at several scales. Additionally, all of these variables can change with each investigated exposure temperature.

As previously mentioned, defining the variables at 'Level I' and Level II' of the multiscale microstructure has been the focus of the majority of this study so far. Now, the primary goal is to link these two scales through homogenization and to compare the results. Secondly, the effect of high temperature exposure at 'Level 0' will be investigated using reverse homogenization or 'downscaling methods' and the experimentally determined properties at 'Level I'.

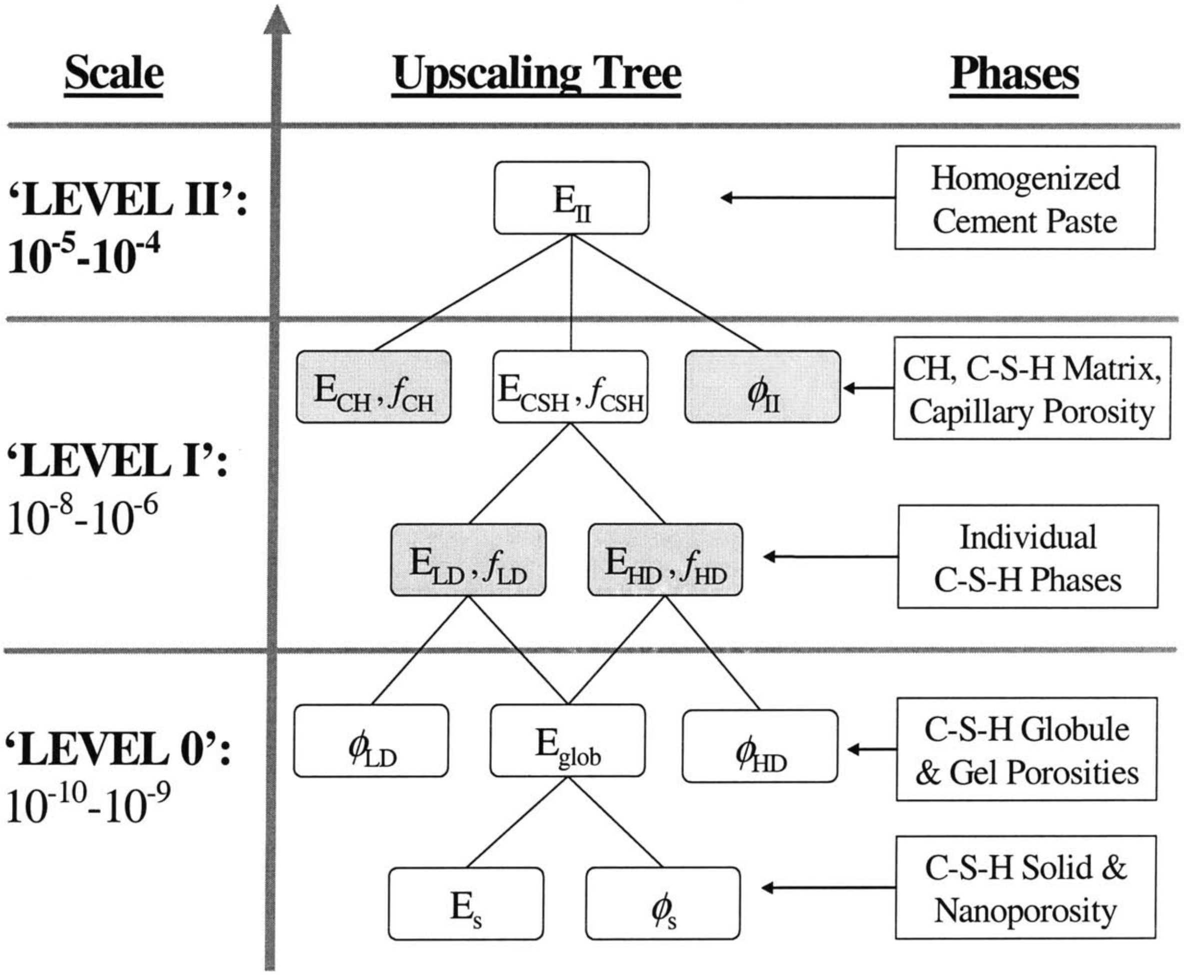

Figure 8-1: Schematic diagram of the homogenization process used to link the elastic properties of the various 'Levels' of the multiscale microstructure.

8.1 Homogenization at 'Level I': Upscaling of Results on Unheated Samples

Before applying homogenization methods to model the effects of high temperature exposure on cement paste, the microporoelastic models will first be applied to the results from investigation of unheated cement paste. Then, once the link between the scales of indentation has been established, the effects of high temperature exposure will be explored using these upscaling methods.

8.1.1 Defining the Initial Phase Properties

The four phases present at 'Level I' are LD C-S-H, HD C-S-H, CH, and the capillary porosity. The corresponding variables necessary for homogenization at this scale are shaded in Figure 8-1. Nanoindentation provided access to the modulus of elasticity and volume fractions of the solid phases (LD C-S-H, HD C-S-H, CH), but the volume fractions need to be verified. Additionally, the capillary porosity is yet to be defined.

Volume Fraction of CH

The results of nanoindentation (see Section 6.6.4) indicated that the volume fraction of CH was approximately 11% and was not affected by exposure of cement paste to high temperature. However, because this result was difficult to determine accurately, verification was needed. For verification, the volume fraction of CH can also be determined from the OPC composition before hydration. Recall the hydration reactions of C-S-H which produce CH as a by-product:

$$\begin{aligned} 2\mathrm{C_3S} + 10.6\mathrm{H} &\longrightarrow \mathrm{C_{3.4}S_2H_8} + 2.6\mathrm{CH} \\ 2\mathrm{C_2S} + 8.6\mathrm{H} &\longrightarrow \mathrm{C_{3.4}S_2H_8} + 0.6\mathrm{CH} \end{aligned} \tag{8.1}$$

Using these relations, the silicate mass percentages ($m_{\mathrm{C_3S}}$ and $m_{\mathrm{C_2S}}$), and the molar masses and densities of C_2S, C_3S, CH, and cement paste [52], an upper bound of the volume fraction of CH can be directly calculated [56]:

$$f_{CH} \leq \frac{0.42m_{\mathrm{C_3S}} + 0.13m_{\mathrm{C_2S}}}{0.71 + 2.24(w/c)} \tag{8.2}$$

Use of the silicate mass percentages given in Table 3.1 ($m_{\mathrm{C_3S}} = 0.53$, $m_{\mathrm{C_2S}} = 0.20$) and the w/c ratio ($w/c = 0.5$) yields $f_{CH} \leq 14\%$. This verifies that the value determined using nanoindentation ($f_{CH} = 11\%$) is reasonable and can be used for modeling.

Capillary Porosity

The porosity of cement paste is defined at each level of the multiscale microstructure according to the characteristic length scale of the pore size. The model of Jennings [33], depicted in Figure 2-4, defines the nanoporosity (ϕ_s) to be 18%, and the LD C-S-H gel porosity (ϕ_{LD}) and HD C-S-H gel porosity (ϕ_{HD}) to be 37% and 24% respectively. It is important to remember that these porosities are inherently characteristic of the corresponding phases, and are therefore independent of the cement paste mix design. However, it is unknown how these porosities evolve during exposure to high temperatures. On the other hand, the capillary porosity is completely dependent on the w/c ratio. High w/c ratios yield increased capillary porosity, and vice versa. Because of this, the initial capillary porosity must be determined experimentally. However, as mentioned in Section 2.2.2, the capillary porosity for a w/c ratio of 0.5 is typically around 3-5%.

The capillary porosity can be estimated using MIP, but MIP equipment was not available so another method of determining the capillary porosity was necessary. As an alternative, the total initial porosity, determined experimentally in Section 3.4, was used. However the initial total porosity measures the sum of all the porosities, so a relationship for calculating the capillary porosity must be derived.

The total gel porosity (ϕ_{gel}) can be calculated directly by combining the two gel porosities and their corresponding volume fractions:

$$\phi_{gel} = f_{LD}\phi_{LD} + f_{HD}\phi_{HD} \tag{8.3}$$

However, this equation does not include the nanoporosity (ϕ_s) present at a smaller scale. Including the nanoporosity, the total porosity at 'Level I' (ϕ_I) can be calculated from:

$$\phi_I = f_{LD}\,[\phi_{LD} + \phi_s(1 - \phi_{LD})] + f_{HD}\,[\phi_{HD} + \phi_s(1 - \phi_{HD})] \tag{8.4}$$

Furthermore, the total porosity at 'Level II' can be calculated by including the capillary porosity:

$$\phi_{II} = \phi_{cap} + f_{LD}\,[\phi_{LD} + \phi_s(1 - \phi_{LD})] + f_{HD}\,[\phi_{HD} + \phi_s(1 - \phi_{HD})] \tag{8.5}$$

Now, a direct relationship between the capillary porosity and the total initial porosity has been established. Substituting the initial values for the nanoporosity ($\phi_s = 0.18$) and gel porosities ($\phi_{LD} = 0.37$, $\phi_{HD} = 0.24$) yields:

$$\phi_{II} = \phi_{cap} + 0.4834 f_{LD} + 0.3768 f_{HD} \tag{8.6}$$

Additionally, including the experimentally determined relative volume fractions (see Section 6.6.4) of LD C-S-H ($f_{LD} = 0.75 f_{CSH}$) and HD C-S-H ($f_{HD} = 0.25 f_{CSH}$) yields:

$$\phi_{II} = \phi_{cap} + 0.457 f_{CSH} \tag{8.7}$$

The volume fraction of C-S-H (f_{CSH}) can be determined using the requirement that the volume fractions of all the 'Level II' phases must add up to one:

$$\phi_{cap} + f_{CSH} + f_{CH} + f_{other} = 1 \tag{8.8}$$

where f_{other} represents the volume fraction of the aluminate, ferrite and clinker phases. Combining Eqs. (8.7) and (8.8) yields:

$$\phi_{cap} = 1.842\phi_{II} + 0.842\,(f_{CH} + f_{other} - 1) \tag{8.9}$$

Assuming that the volume fraction of the other phases is negligible ($f_{other} = 0$):

$$\phi_{cap} = 1.842\phi_{II} + 0.842\,(f_{CH} - 1) \tag{8.10}$$

Phase	**Elasticity** (E) [GPa]	**Volume Fraction** (f)
C-S-H Matrix	-	0.829
LD C-S-H	18.1	$0.75 \times f_{CSH} = 0.622$
HD C-S-H	30.6	$0.25 \times f_{CSH} = 0.207$
CH	37.3	0.11
ϕ_{cap}	-	0.061

Table 8.1: Values used for the homogenization of the phases at Level I of the multiscale microstructure.

Use of the initial total porosity ($\phi_{II} = 0.44$) determined in Section 3.4 and the volume fraction of CH ($f_{CH} = 0.11$) verified in the previous section, the initial capillary porosity was determined to be 6.1% ($\phi_{cap} = 0.061$).

Volume Fraction of C-S-H phases

The volume fractions of the C-S-H phases were determined directly using nanoindentation frequency distributions (see Tables 6.2 and 6.3). However, because volume fraction results using frequency distributions are highly variable, another method of determining the C-S-H volume fractions was desired.

Instead, the volume fraction of the C-S-H phases was determined using the requirement that the sum of all volume fractions equals one (see Eq. (8.8)). Using this requirement, the volume fraction of the C-S-H matrix (sum of both C-S-H phases) was determined, but the volume fraction of each C-S-H phase needed to be defined. Using nanoindentation frequency distributions, the C-S-H matrix was determined to be 75% LD C-S-H and 25% HD C-S-H (see Section 6.6.4). With this result, the volume fractions of the C-S-H phases can be directly calculated. The resulting volume fractions were then compared with the results using nanoindentation frequency distributions for verification.

All the variables necessary for homogenization have now been defined and are summarized in Table 8.1.

8.1.2 Results of Upscaling

The MT scheme defined in Section 7.2.1 and the SC scheme defined in Section 7.2.2 were both used for the upscaling of elastic properties. Using the values in Table 8.1, the homogenized modulus of elasticity was determined to be $E_{II}^{MT} = E_{II}^{SC} = 19.4$ GPa using the MT and SC schemes. Both schemes yield the same result, indicating that the properties of the reference medium were similar in both cases. Microindentation on cement paste cured for the same period (28 days), yielded an elastic modulus of $E_{II}^{micro} = 15.7$ GPa. The difference between these results is quite large and requires an explanation.

First, recall that the results of microindentation on samples cured for 28 days led to the conclusion of a large capillary porosity at the time of testing (see Section 5.4). This would indicate that the initial capillary porosity could have been higher than 6.1%. Second, recall that nanoindentation results indicated the presence of aluminate and ferrite phases within the LD C-S-H, and the presence of clinker phases affecting the results of HD C-S-H. The presence of these minor phases necessitate the re-evaluation of the assumption made in Section 8.1.1 that the volume fraction of the other phases was negligible ($f_{other} = 0$). Because calculation of the initial capillary porosity is highly affected by the the presence of minor phases ($f_{other} \neq 0$), another method of determining the initial capillary porosity is necessary.

As an alternative to using the capillary porosity calculated in Section 8.1.1, the capillary porosity was instead calculated by the MT and SC schemes themselves. Requiring the homogenized modulus of elasticity to equal the results of microindentation ($E_{II}^{MT} = E_{II}^{SC} = E_{II}^{micro} =$ 15.7 GPa), the initial capillary porosity was determined to be $\phi_{cap}^{MT} = 0.166$ and $\phi_{cap}^{SC} = 0.145$ using each method. In order to accommodate this increased porosity, the volume fraction of C-S-H had to be adjusted. The new capillary porosity was used to calculate the corresponding volume fraction of the minor phases using Eq. (8.9), and yielded $f_{other}^{MT} = 0.11$ and $f_{other}^{SC} = 0.09$ using each method. This confirms the expected presence of minor phases at the time of testing. One might conclude that these minor phases should be included as separate phases in the upscaling model. However, since the effects of these minor phases have already been included in the measurement of the phase properties using nanoindentation, their inclusion as separate phases is not necessary.

Because the calculation of capillary porosity using the homogenization schemes was effective for cement paste samples cured for 28 days, the capillary porosity of samples cured for 90 days was also calculated using homogenization. Again, requiring the homogenized modulus of elasticity to equal the results of microindentation ($E_{II}^{MT} = E_{II}^{SC} = E_{II}^{micro} = 20.8$ GPa), the capillary porosity was determined to be $\phi_{cap}^{MT} = \phi_{cap}^{SC} = 0.028$, and the volume fraction of the C-S-H matrix was determined to be $f_{CSH}^{MT} = f_{CSH}^{SC} = 0.862$. This compares well with the typical capillary porosity of 3-5% for a fully cured cement paste with a w/c ratio of 0.5 (see Section 2.2.2).

8.2 Homogenization at 'Level I': Upscaling of Results on Heated Samples

8.2.1 Defining the Input Properties

The input properties necessary for homogenization of results on unheated samples (25°C) have now been defined, and serve as a starting point for defining the variables necessary for homogenization of results on heated samples. All input properties necessary for homogenization of results on heated samples will now be defined.

Elasticity

The elasticities of LD C-S-H and HD C-S-H were determined using nanoindentation for all temperatures of investigation (see Section 6.5). The elasticity of CH was also determined using nanoindentation for all temperatures of investigation up to and including 400°C. At higher temperatures, however, CH has completely dehydrated to form CaO. The actual elasticity of CaO was not able to be measured using nanoindentation, but it is known to be very stiff. Because of this, the elasticity of CaO was assumed to be 50 GPa. However, in order to determine the importance of CaO on the homogenized elasticity result, an elasticity of 100 GPa instead of 50 GPa was also used and caused little difference in the results of upscaling.

Volume Fractions

The phase volume fractions of unheated samples were determined in the previous section, but the effect of high temperature on the phase volume fractions need to be reviewed and defined.

First, nanoindentation results led to the conclusion that the volume fraction of CH was not affected by temperature exposures up to and including 400°C (see Section 6.6.4). Second, nanoindentation results led to the conclusion that C-S-H transformation did not occur as a result of high temperature exposure, so the relative percentage of the C-S-H phases remained constant (see Section 6.6.4). Third, MIP results of previous investigations indicate that the capillary porosity is not affected by temperature exposures up to 400°C (see Table 2.6). As a result, all phase volume fractions were assumed to remain constant up to and including 400°C.

After exposure to 550°C, volume fractions clearly change due to the dehydration of CH. CH dehydration is known to be accompanied by a 30% reduction in volume [43], so the volume fraction of CH was reduced by 30% at 550°C. This phase shrinkage would logically cause an increase in capillary porosity, so it was assumed that the decrease in the CH volume fraction would cause an increase in the capillary porosity of the same magnitude. MIP results indicate that an increase in capillary porosity occurs from 400°C to 550°C, confirming this assumption. In summary, CH dehydration causes a decrease in the CH/CaO volume fraction, an increase in capillary porosity, and no change in the C-S-H phase volume fractions at 550°C.

After exposure to 700°C, the volume fraction of CaO was assumed to be the same as at 550°C because no additional CH dehydration occurs. However, the volume fractions of the other phases are much more difficult to determine accurately. MIP results indicate that the capillary porosity increases dramatically, which would necessarily cause a reduction in the volume fractions of the C-S-H phases. Additionally, volume measurements indicated that the total volume stopped decreasing between 550°C and 700°C (see Section 4.2), while C-S-H dehydration continued. Because C-S-H dehydration is accompanied by shrinkage, this also indicated an increase in capillary porosity which would be accompanied by a decrease in the C-S-H phase volume fractions. As an initial assumption, the capillary porosity was assumed to increase to 20% ($\phi_{cap} = 0.20$), but this assumption will be revisited in the following section.

All variables necessary for homogenization have now been defined and are summarized in Table 8.2.

Temp. [°C]	Elasticity [GPa]				Volume Fraction					
	E_{LD}	E_{HD}	E_{CH}	E_{CaO}	f_{CSH} *	f_{LD}	f_{HD}	f_{CH}	f_{CaO}	ϕ_{cap}
25	18.1	30.6	37.3	-	0.862	0.646	0.216	0.11	-	0.028
105	17.3	28.8	40.0	-	0.862	0.646	0.216	0.11	-	0.028
200	16.8	26.3	42.8	-	0.862	0.646	0.216	0.11	-	0.028
300	14.4	25.0	35.8	-	0.862	0.646	0.216	0.11	-	0.028
400	12.4	21.1	30.8	-	0.862	0.646	0.216	0.11	-	0.028
550	9.3	16.7	-	50	0.862	0.646	0.216	-	0.076	0.062
700	10.0	17.6	-	50	0.724	0.543	0.181	-	0.076	0.20

*A ratio of LD to HD C-S-H of 75/25 was used for all temperatures of investigation.

Table 8.2: Summary of all variables used for upscaling from Level I to Level II.

Temperature [°C]	Modulus of Elasticity [GPa]		
	E_{II}^{micro}	E_{II}^{MT}	E_{II}^{SC}
25	20.8	20.81	20.76
105	19.7	20.08	20.05
200	19.6	19.40	19.37
300	16.7	16.97	16.96
400	15.9	14.58	14.56
550	10.0	10.48	10.43
700	6.08	8.46	7.65

Table 8.3: Results of microindentation and upscaling methods.

8.2.2 Results of Upscaling

Both the MT scheme and SC scheme were used for homogenization. The results are displayed in Table 8.3 and Figure 8-2 with the results of microindentation for comparison.

8.2.3 Discussion of Upscaling

The results of upscaling show that the MT and SC schemes produce nearly identical results for investigation temperatures up to 550°C. Only at 700°C, where the capillary porosity is much larger, do the results vary noticeably. Therefore, it seems that both methods are appropriate where porosities are low, but comparison with microindentation results indicate that the SC scheme is more appropriate when capillary porosities are high. This makes sense because as porosity increases, the proximity of pores with respect to each other would also increase, and the pores would have an effect on each other. In other words, the assumption of the MT scheme that each pore is imbedded in a continuous solid matrix would no longer be accurate because

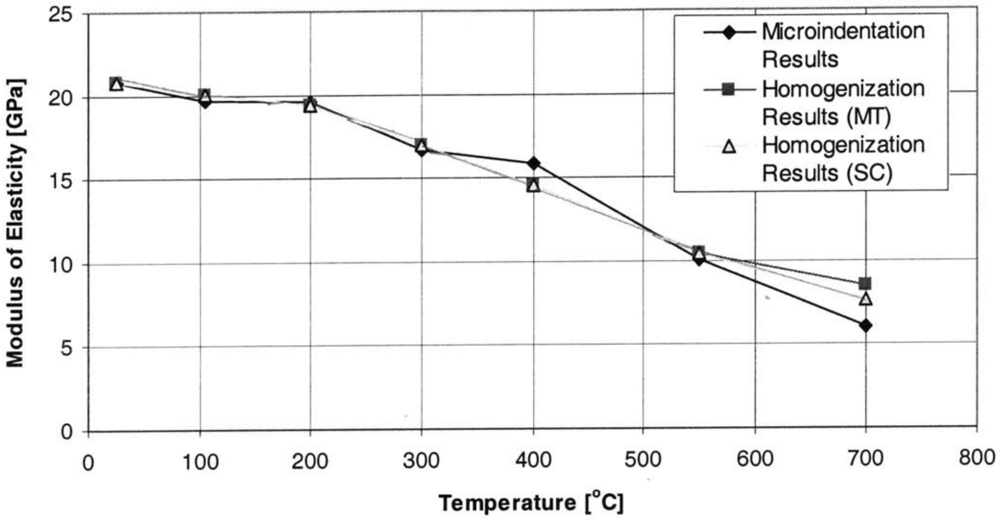

Figure 8-2: Results of microindentation and upscaling methods.

the 'completely solid matrix' would be influenced by the surrounding pores. The assumption of the SC scheme that the matrix is a homogenization of all phases is clearly more appropriate.

Upscaling results compare remarkably well with the results of microindentation (see Fig. 8-2). For investigation temperatures up to 400^{o}C, results confirm that the capillary porosity remains relatively constant and the source of high temperature degradation is within the LD and HD C-S-H phases. At 550^{o}C, upscaling and microindentation results also compare remarkably well, indicating that CH dehydration does cause a direct increase in capillary porosity. This also confirms the increase in capillary porosity observed using MIP.

At 700^{o}C, the assumed increase in capillary porosity ($\phi_{cap} = 0.20$) was not sufficient to capture the drastic decrease in microindentation results, although an increase in capillary porosity is the most logical explanation for this decrease. In fact, if one assumes the upscaling results to match the microindentation results ($E_{II}^{SC} = E_{II}^{micro}$) the resulting capillary porosity would be $\phi_{cap}^{SC} = 0.26$. Although MIP results are not exact because of the discussed limitations of the testing method (see Section 2.4.1), this dramatic increase in capillary porosity is much larger than the porosity increase observed using MIP. As a result, it seems that an increase in capillary porosity is occurring along with another factor to cause this large decrease in elasticity. This other factor is most likely microcracking during indentation and/or the possible transformation of the C-S-H microstructure which will be discussed later in this chapter.

8.3 Reverse Homogenization at 'Level I': Downscaling of Results on Unheated Samples

The properties of the phases present at 'Level 0' of the multiscale microstructure are not accessible experimentally, but they can be estimated using downscaling methods. In this section, the results of nanoindentation (M_{LD} and M_{HD}) and the gel porosities from Jennings model (ϕ_{LD} and ϕ_{HD}) will be used to estimate the elasticity of a single C-S-H globule (E_{glob}), which has been assumed to be the building block of both types of C-S-H. Both the MT and SC schemes will be used in order to determine which is more appropriate. Both types of C-S-H are single solid phase porous materials, so the equations derived in Sections 7.3.1 and 7.3.2 apply and were used. If only one type of C-S-H globule exists, as the Jennings model predicts, the results of downscaling would be the same for both types of C-S-H (i.e. $E_{glob}^{LD} = E_{glob}^{HD}$).

8.3.1 Mori-Tanaka Scheme

The modulus of elasticity of the C-S-H globule was determined using Eq. (7.37). Clearly, the result is dependent upon the indentation modulus of the homogenized medium (M_{LD}^{nano} or M_{HD}^{nano}), the porosity (ϕ_{LD} or ϕ_{HD}), and the Poisson's ratio of the C-S-H globules (ν_{glob}). As previously mentioned, the indentation modulus was determined using nanoindentation and, as a first approximation, the gel porosities from Jennings model were used. Also as a first estimate, ν_{glob} was assumed to be 0.24. Trial 1 in Table 8.4 shows the values of the input properties and downscaling results for this first approximation, which resulted in different values for the elasticity of the globules in each C-S-H phase ($E_{glob}^{LD} \neq E_{glob}^{HD}$). This contradicts the assumption of only one type of C-S-H globule, which indicates that either the MT scheme does not accurately represent the microstructure of C-S-H, or the assumption of one type of C-S-H globule is incorrect. Further investigation was necessary.

First, the assumption that the Poisson's ratio of the globule is equal to 0.24 was reviewed. In order to determine the effect of the Poisson's ratio on the elasticity of the C-S-H globules, downscaling was repeated using minimum ($\nu_{glob} = 0$) and maximum ($\nu_{glob} = 0.5$) values for the Poisson's ratio. Trials 2 and 3 in Table 8.4 indicate that the Poisson's ratio does have an effect on the magnitude of the elasticity of the C-S-H globules, but the elasticity of the globules in each C-S-H phase remain different ($E_{glob}^{LD} \neq E_{glob}^{HD}$). In other words, changing the Poisson's ratio had little effect on the convergence of the elasticity of the C-S-H globules, so the initial assumption that $\nu_{glob} = 0.24$ was not revised.

Second, the gel porosities were reviewed. Assuming that there is only one type of C-S-H globule, the gel porosities were adjusted until convergence was reached ($E_{glob}^{LD} = E_{glob}^{HD}$). Trials 4 through 6 in Table 8.4 show that increasing ϕ_{LD} and decreasing ϕ_{HD} by the same amount led to convergence at $\phi_{LD} = 0.422$ and $\phi_{HD} = 0.188$. These gel porosity values are significantly different than the porosities predicted by Jennings model ($\phi_{LD} = 0.37$, $\phi_{HD} = 0.24$) and the porosities corresponding to the maximum random packing density ($\phi_0 = 0.36$) and the maximum ordered packing density ($\phi_0 = 0.26$) of monosized spheres introduced in Section 2.2.1. In fact, $\phi_{HD} = 0.188$ exceeds the maximum ordered packing density, which is not logical considering the spherical representation of the C-S-H globule in our microstructural model. Again, it seems that the MT scheme does not accurately represent the microstructure of HD and LD C-S-H.

Last, the effect of Poisson's ratio on the values of the gel porosities at convergence was also investigated (see Trials 7 and 8 in Table 8.4). The Poisson's ratio had little effect on the gel porosities at convergence, and only affected the magnitude of the elasticity of the C-S-H globules.

8.3.2 Self-Consistent Scheme

The modulus of elasticity of the C-S-H globule was determined using Eq. (7.44). The result is again dependent on the indentation modulus of the homogenized medium (M_{LD}^{nano} or M_{HD}^{nano}), the porosity (ϕ_{LD} or ϕ_{HD}), and the Poisson's ratio of the C-S-H globules (ν_{glob}). As was done when using the MT scheme, the indentation modulus was determined from nanoindentation, the gel porosities from the Jennings model were initially used, and ν_{glob} was assumed to be 0.24. Trial 1 in Table 8.5 shows the results for these initial assumptions and again indicates a difference in the elasticity of the globules in each C-S-H phase ($E_{glob}^{LD} \neq E_{glob}^{HD}$).

Trial	Input Properties					Downscaling Results	
	M_{LD}^{nano} [GPa]	M_{HD}^{nano} [GPa]	ϕ_{LD}	ϕ_{HD}	ν_{glob}	E_{glob}^{LD} [GPa]	E_{glob}^{HD} [GPa]
1	19.2	32.4	0.37	0.24	0.24	40.8	52.1
2	"	"	"	"	0.0	39.7	50.2
3	"	"	"	"	0.5	34.4	42.6
4	"	"	0.39	0.22	0.24	41.6	48.1
5	"	"	0.41	0.20	0.24	43.6	46.1
6	"	"	0.422	0.188	0.24	44.9	44.9
7	"	"	0.426	0.184	0.0	46.5	46.5
8	"	"	0.414	0.196	0.5	38.4	38.4

Table 8.4: Summary of the input properties and results of reverse homogenization using the MT scheme.

Trial	Input Properties				Downscaling Results	
	M_{LD}^{nano} [GPa]	M_{HD}^{nano} [GPa]	ϕ_{LD}	ϕ_{HD}	E_{glob}^{LD} [GPa]	E_{glob}^{HD} [GPa]
1	19.2	32.4	0.37	0.24	70.6	59.2
2	"	"	0.36	0.26	65.5	64.2
3	"	"	0.357	0.26	64.2	64.2

Table 8.5: Summary of the input properties and results of reverse homogenization using the SC scheme.

In order to evaluate the magnitude of the change in gel porosity that would explain the difference in the elasticity of the C-S-H globules, the gel porosities were again adjusted until convergence was reached ($E_{glob}^{LD} = E_{glob}^{HD}$). Initially, ϕ_{LD} was adjusted to the porosity corresponding to the maximum random packing density ($\phi_0 = 0.36$), and ϕ_{HD} was adjusted to the porosity corresponding to the maximum ordered packing density, ($\phi_0 = 0.26$) (see Trial 2 in Table 8.5). Then, ϕ_{LD} was adjusted to achieve convergence (see Trial 3 in Table 8.5). The gel porosities necessary to achieve convergence were close to the gel porosities in Jennings model, and remarkably close to the maximum packing density porosities. As a result, the SC scheme seems to represent the microstructure of the C-S-H phases quite accurately, and supports the existence of one type of C-S-H globule.

8.3.3 Discussion of Downscaling Methods

Comparison of the downscaling results of the MT scheme and SC scheme indicates that the SC scheme more accurately represents the microstructure of the C-S-H phases. Is this logical? Do the assumptions used to develop each scheme support this conclusion?

The MT scheme is based on the presence of a dominant matrix phase with spherical inclusions. However, the multiscale microstructure is based on the existence of globules which form the two types of C-S-H through different packing arrangements. Clearly the packing of a single particle type, no matter what the shape, does not agree with the assumption of a solid matrix with spherical inclusions. Therefore, the MT scheme does not accurately represent the microstructure of C-S-H.

On the other hand, the SC scheme is based on a perfectly disordered microstructure with no dominant phase in which inclusions exist. Instead, each phase is assumed to be spherical and to exist within a homogenized matrix. Although this representation is not perfect, it is much closer to the packing of a single particle type, and therefore is a much more appropriate representation of the microstructure of C-S-H. Additionally, initial comparison of the two homogenization schemes in Section 7.3.3 led to the conclusion that the SC scheme more realistically predicts a percolation threshold below which the homogenized material completely loses its stiffness.

Based on these downscaling results and the discussion in Section 7.3.3, the SC scheme is clearly more representative of the C-S-H microstructure. Therefore, only the SC scheme will be used to determine the effects of high temperature exposure on the phases at 'Level 0' of the multiscale microstructure in the following section. The initial globule elasticity ($E_{glob} = 64.2$ GPa) and gel porosities ($\phi_{LD} = 0.357$, $\phi_{HD} = 0.26$) found using the SC scheme will be used.

8.4 Reverse Homogenization at 'Level I': Downscaling of Results on Heated Samples

Now that the 'Level 0' phase properties of unheated cement paste have been defined, the effect of high temperature exposure on the 'Level 0' phases can be explored. The SC scheme was determined to be most appropriate, and will be used to determine what is causing the high temperature degradation of the C-S-H phases observed through nanoindentation.

8.4.1 Defining the Input Properties

In order to use the SC scheme to determine the effect of high temperature on the 'Level 0' phase properties of cement paste, it is first necessary to define the properties which are necessary for downscaling. Using Eq. (7.44), downscaling depends on the following properties: M_{LD}, M_{HD}, ϕ_{LD}, ϕ_{HD}, M_{glob}, and ν_{glob}. These properties were defined for unheated samples (25^{o}C), but the properties of samples exposed to higher temperatures require further definition.

First, the results of nanoindentation (see Table 6.2) were used to define the indentation modulus of both C-S-H phases (M_{LD}^{nano}, M_{HD}^{nano}) at all temperatures of investigation. Second, the Poisson's ratio was assumed to be 0.24 for all temperatures of investigation. In reality, the Poisson's ratio is unknown, but the previous section and Figure 7-1 showed that the Poisson's ratio has little effect on downscaling results. At this point, the gel porosities (ϕ_{LD} and ϕ_{HD}) and the globule indentation modulus (M_{glob}) remain unknown, so it is necessary to review the data which is available for their determination.

Gel Porosities

Defining the gel porosities is difficult because they can not be accurately measured experimentally. However, MIP results give some indication of the effect of high temperature exposure on the gel porosities. As mentioned in Section 2.4.2, Komonen *et al.* [35] found that little change in pore diameters less than 40 nm occurred from 120-300^{o}C. Additionally, Jumppanen [32] found that gel porosities ($\sim$2 nm) remained relatively constant from 150-350^{o}C. However, both investigators also found that the gel porosities increase significantly at higher temperatures. No one has directly measured the magnitude of increase, so it is unrealistic to estimate the gel porosities at these higher temperatures of investigation. Based on these findings, the gel porosities can be assumed to remain constant up to 300^{o}C, but remain unknown at higher temperatures.

Globule Elasticity

In order to determine the effect of high temperature exposure on the globule elasticity, we have two sources of experimental data available: nanoindentation elasticity results and mass loss measurements. First, nanoindentation results provide a measure of the change in elasticity of the C-S-H phases (M_{LD} and M_{HD}), which can only result from a change in gel porosity (ϕ_{LD} and ϕ_{HD}) or a change in globule elasticity (M_{glob}).

Second, the primary effect of high temperature exposure on cement paste is the dehydration of C-S-H. Dehydration was evaluated in Section 4.1 by measuring the mass loss with respect to temperature through thermogravimetry (TG) and manual mass measurements. Additionally, as discussed in section 2.3.1, dehydration necessarily occurs within the C-S-H globules because it is a process which takes place on the atomic scale. Therefore, according to the multiscale microstructural model, dehydration of C-S-H would clearly have an effect on the elastic properties of the C-S-H globules (M_{glob}). Furthermore, since mass loss was used to measure C-S-H dehydration, there would logically be a link between mass loss and the elasticity of the C-S-H globules.

In order to correlate these two experimental data sources (nanoindentation and thermogravimetry), the normalized average C-S-H elasticity (from nanoindentation results) is plotted as a function of the normalized C-S-H mass loss in Figure 8-3. Clearly, Figure 8-3 demonstrates a linear relationship between the average C-S-H elasticity and the C-S-H mass loss from 105-300°C. However, at higher temperatures the average C-S-H elasticity begins to decrease more rapidly and deviates from this linear relationship. Additionally, recall that the gel porosity was determined to remain constant in this same temperature range (105-300°C), and then increase at higher temperatures. Therefore, in the temperature range where the gel porosities remain constant, the only variable which can account for the reduction in the C-S-H elasticity is the globule elasticity (M_{glob}). As a result, it is evident that the reduction in the C-S-H globule elasticity is linearly related to the C-S-H mass loss. Furthermore, the deviation from the linear relationship at higher temperatures (>300°C) can be directly related to an increase in gel porosity (ϕ_{LD} and ϕ_{HD}) that is a change in the packing density of the two types of C-S-H.

8.4.2 Downscaling for Temperatures up to 300°C

Based on the fact that the gel porosities remain constant below 300°C, it is appropriate to address downscaling in this temperature region before addressing higher temperatures. All the necessary properties have been defined in order to determine the effect of high temperature exposure on the C-S-H globule elasticity (E_{glob}) in this temperature range.

Table 8.6 summarizes the input properties and results of downscaling for temperatures of investigation up to 300°C. Recall that the results of downscaling the LD and HD C-S-H properties should yield the same results (i.e. $E^{LD}_{glob} = E^{HD}_{glob}$). The HD and LD downscaling

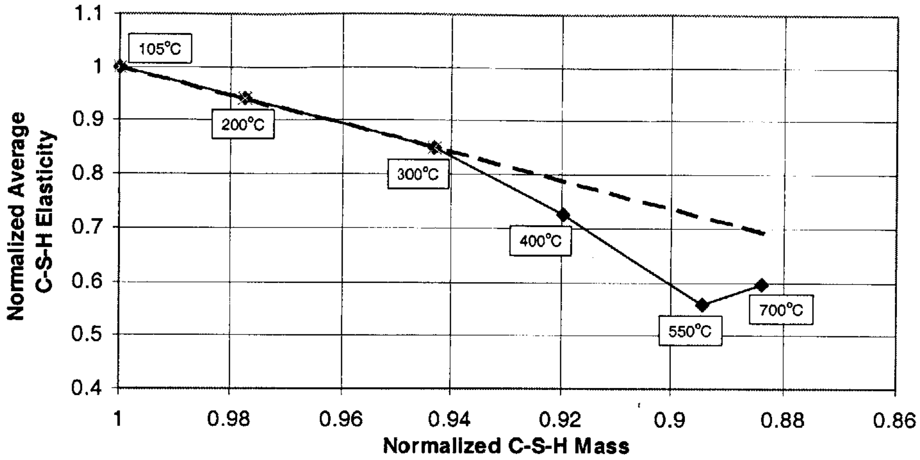

Figure 8-3: Average C-S-H elasticity determined using nanoindentation as a function of C-S-H mass loss determined using thermogravimetry.

Temp. [°C]	Input Properties				Downscaling Results		
	M_{LD}^{nano} [GPa]	M_{HD}^{nano} [GPa]	ϕ_{LD}	ϕ_{HD}	E_{glob}^{LD} [GPa]	E_{glob}^{HD} [GPa]	$E_{glob}^{average}$ [GPa]
25	19.2	32.4	0.357	0.26	64.1	64.1	64.1
105	18.4	30.5	"	"	61.4	60.3	60.9
200	17.8	27.9	"	"	59.5	55.2	57.4
300	15.3	26.5	"	"	51.1	52.4	51.8

Table 8.6: Summary of the input properties and results of reverse homogenization for temperatures of investigation up to 300 C using the SC scheme.

results compare well, with only the 200°C results showing any significant variation. This shows that a change in only the elasticity of the C-S-H globules (E_{glob}) can account for the high temperature degradation of both of the C-S-H phases up to 300°C. Furthermore, it shows that the source of high temperature C-S-H degradation is within the C-S-H globules themselves, as one might expect. Lastly, it supports the conclusion made in previous investigations that the gel porosities remain relatively constant up to 300°C.

8.4.3 Linking C-S-H Mass Loss with C-S-H Globule Elasticity

With the C-S-H globule elasticity determined for temperatures up to 300^{o}C, we have the information necessary to link the C-S-H mass loss with the C-S-H globule elasticity in this temperature range. This can be represented by the following equation:

$$\frac{E^{T}_{glob}}{E^{105^oC}_{glob}} = \left(1 + C\left(\frac{m^T}{m^{105^oC}} - 1\right)\right) \tag{8.11}$$

where $E^{105^oC}_{glob}$ and E^{T}_{glob} are the C-S-H globule elasticity at 105^{o}C ($E^{105^oC}_{glob} = 60.9$) and temperature T, respectively, m^{105^oC} and m^T are the sample masses at 105^{o}C and temperature T, respectively, and C is calibration factor which links the change in mass to the change in elasticity. The calibration factor can be obtained directly from the results in Table 8.6 and the results of thermogravimetry. The C-S-H globule elasticity at higher temperatures can be estimated by rearranging the terms in Eq. (8.11):

$$E^{T}_{glob} = E^{105^oC}_{glob}\left(1 + C\left(m^T_{norm} - 1\right)\right) \tag{8.12}$$

where $m^T_{norm} = \frac{m^T}{m^{105^oC}}$ is the normalized mass at temperature T. Now, the C-S-H globule elasticity has been determined as as function of mass loss, but the mass loss comes from two sources: C-S-H dehydration and CH dehydration. Equation (8.12) is valid up to 400^{o}C because no CH dehydration occurs. However, at 550^{o}C and 700^{o}C, mass loss from CH dehydration must be accounted for. Using the results of thermogravimetry (see Fig. 4-1), the normalized mass loss due to CH dehydration can be estimated and used to accurately determine the C-S-H globule elasticity at 550^{o}C and 700^{o}C:

$$E^{T}_{glob} = E^{105^oC}_{glob}\left(1 + C\left(m^T_{norm} + m^{CH}_{norm} - 1\right)\right) \tag{8.13}$$

where $m^{CH}_{norm} = \frac{m^{CH}}{m^{105^oC}}$. Additionally, m^{CH} is the estimated mass loss corresponding CH dehydration and m^{105^oC} is still the sample mass at 105^{o}C. Therefore, the mass loss corresponding *only* to C-S-H dehydration is:

$$m^{CSH}_{norm} = m^T_{norm} + m^{CH}_{norm} \tag{8.14}$$

Temperature	Input Properties		Results
[^oC]	$E_{glob}^{105^oC}$ [GPa]	m_{norm}^{CSH}	E_{glob}^{T} [GPa]
105	60.9	1.0	60.9
200	"	0.978	57.3
300	"	0.943	51.8
400	"	0.920	48.0
550	"	0.894	44.0
700	"	0.884	42.3

Table 8.7: Summary of the input properties and results of linking mass loss with C-S-H globule elasticity at temperatures above 300 C.

and Eq. (8.13) can be rewritten:

$$E_{glob}^{T} = E_{glob}^{105^oC}\left(1 + C\left(m_{norm}^{CSH} - 1\right)\right) \tag{8.15}$$

As a result, a method of linking the C-S-H globule elasticity directly to the mass loss caused by C-S-H dehydration has been obtained.

8.4.4 Downscaling for Temperatures above 300^{o}C

Using the results in Table 8.6 and Section 4.1, Eq. (8.15) was used to estimate the modulus of elasticity of the C-S-H globules. Table 8.7 summarizes the input properties and results of this method of estimation. Also, Figure 8-4 displays the estimated values of m_{norm}^{CSH} with the normalized results of thermogravimetry for comparison, as well as the resulting normalized C-S-H globule elasticities.

The results show that Eq. (8.13) accurately predicts the values of $E_{glob}^{200^oC}$ and $E_{glob}^{300^oC}$ in Table 8.6, indicating that the calibration factor was calculated correctly ($C = 2.64$). It is understood that this is only a method of estimating the modulus of elasticity of the C-S-H globules which has not been proven correct, but it provides the necessary information in order to continue downscaling the results of nanoindentation at higher temperatures where gel porosities are known to increase. However, despite the fact that is is only an estimation method, it is logical if no chemical reactions or phase transformations occur besides dehydration. This is almost certainly the case in the primary range of C-S-H dehydration (see Section 2.1.2) up to and including 550^{o}C. However, during the secondary range of C-S-H dehydration (650-750^{o}C),

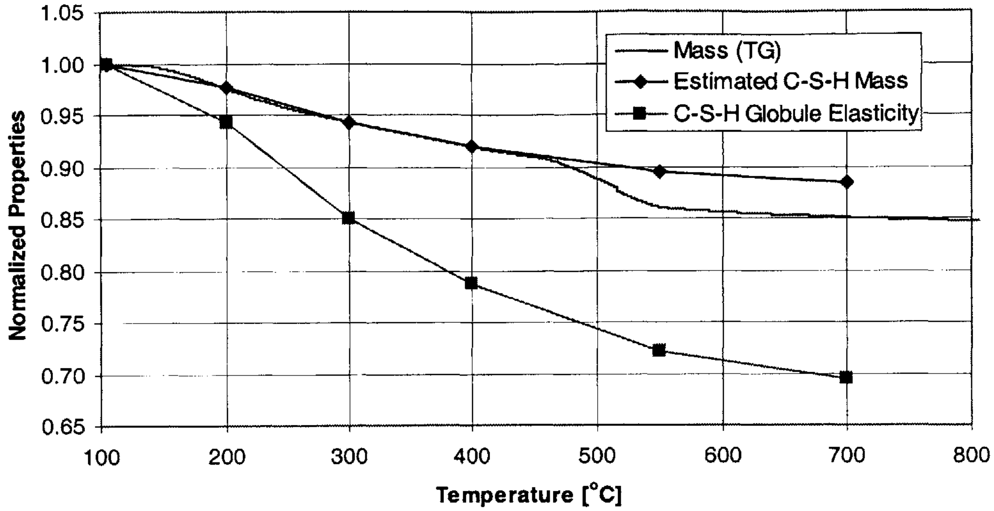

Figure 8-4: Normalized thermogravimetric results, estimated C-S-H mass, and estimated C-S-H globule elasticities with respect to temperature.

decomposition of C-S-H could occur [52] so the accuracy of the estimation of $E_{glob}^{700^oC}$ is less certain.

The Effects of High Temperature on the Gel Porosities

For all temperatures of investigation the C-S-H globule elasticity values have now been determined, so the SC scheme can be used to solve for the change in the gel porosities at temperatures above 300°C.

In order to use the SC scheme to determine the change in the gel porosities above 300°C, the following input properties must be defined at all temperatures of investigation: M_{LD}, M_{HD}, ν_{glob}, and E_{glob}. As done previously, C-S-H phase elasticities were determined using nanoindentation (see Fig. 6-16) and ν_{glob} was assumed to be 0.24. Additionally, the results of linking mass loss with elasticity were used to define the elasticity of the C-S-H globules (see Table 8.7).

Table 8.8 summarizes the input properties and the corresponding estimated gel porosities. From 300-550°C, the results show that the gel porosities increase, but from 550-700°C they decrease slightly.

Temp. [°C]	Input Properties			Downscaling Results	
	M_{LD}^{nano} [GPa]	M_{HD}^{nano} [GPa]	E_{glob} [GPa]	ϕ_{LD}	ϕ_{HD}
300	15.3	26.5	51.8	0.357	0.260
400	13.2	22.4	48.0	0.369	0.278
550	9.9	17.7	44.0	0.393	0.308
700	10.7	18.7	42.3	0.380	0.290

Table 8.8: Summary of the input properties and results of reverse homogenization for temperatures of investigation above 300 C using the SC scheme.

Temperature [°C]	E_{glob} [GPa]	ϕ_{LD}	ϕ_{HD}
25	64.1	0.357	0.260
105	60.9	0.357	0.260
200	57.3	0.357	0.260
300	51.8	0.357	0.260
400	48.0	0.369	0.278
550	44.0	0.393	0.308
700	42.3	0.380	0.290

Table 8.9: Summary of the results of downscaling using the SC scheme.

8.4.5 Discussion of Downscaling

The SC scheme has been used to downscale the results of nanoindentation at all temperatures of investigation. As a result, estimates of the phase properties at 'Level 0' of the multiscale microstructure have been obtained (see Table 8.9). These phase properties are plotted with respect to temperature in Figure 8-5. Additionally, Figure 8-6 shows the effect of an increase in gel porosity (decrease in packing density) on M_{LD}/M_{glob} and M_{HD}/M_{glob} (M_{hom}/M_s, see Fig. 7-1) using the SC scheme.

High Temperature Degradation of C-S-H Globules

The results indicate that high temperature degradation within the C-S-H globules is the only source of the observed high temperature degradation of the C-S-H phases for temperatures up to 300°C (i.e. the gel porosities remain constant). Furthermore, the source of this high temperature degradation within the C-S-H globules has been assumed to be the dehydration of C-S-H. Logically, this assumption would hold true between 105-300°C when the majority of mass loss due to C-S-H dehydration occurs, but the observed degradation of the C-S-H globules

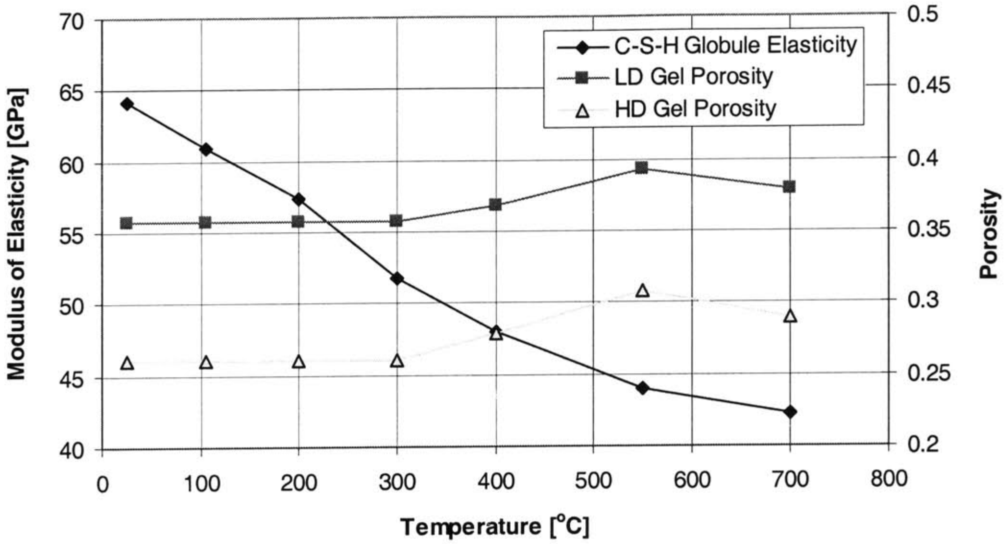

Figure 8-5: Results of downscaling: 'Level 0' phase properties plotted with respect to temperature.

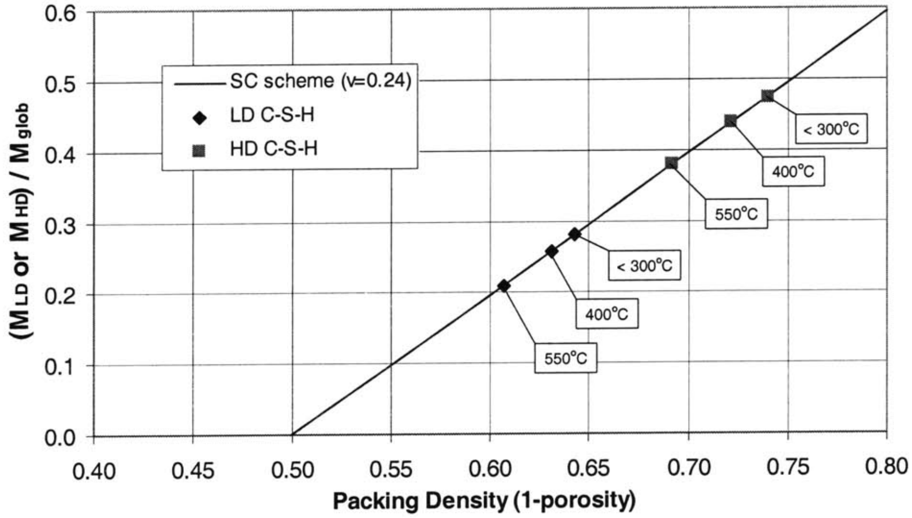

Figure 8-6: Results of downscaling: packing density versus M_{LD}/M_{glob} and M_{HD}/M_{glob} as predicted using the SC scheme assuming $v_{glob} = 0.24$.

from 25-105^oC needs further explanation.

Slight C-S-H dehydration could occur in this temperature range, but alone would not account for an equal amount of degradation as was observed between 105-200^oC, where C-S-H dehydration is known to be substantial. Instead, the removal of water from the nanopores within the C-S-H globules seems a more probable explanation for two reasons. First, the removal of water from the nanopores would cause the C-S-H globule, a single solid porous material, to go from an undrained to a drained state causing a reduction in the elasticity. Secondly, removal of water from the nanopores could have an effect on the microstructure of the C-S-H globules.

At temperatures above 300^oC, recall that the elasticity of the C-S-H globules was estimated using mass loss measurements. Again, this estimation method is logical in the primary range of C-S-H dehydration up to 550^oC, where no transformation of C-S-H is believed to occur. However, if the secondary range of C-S-H dehydration is evidence of a microstructural transformation of C-S-H, the accuracy of the estimation method for the 700^oC results would be less reliable.

Effects of High Temperature on the Gel Porosities

Up to 300^oC, the results indicate that the assumption that the gel porosities remain constant was accurate. From 300-550^oC, linking C-S-H mass loss to a decrease in the C-S-H globule elasticity led to an increase in the gel porosities. MIP investigations confirm this result, showing an increase in gel porosity in the same temperature range [35] [32] (see Table 2.6). At 550^oC, the estimated gel porosities achieved their maximum values ($\phi_{LD} = 0.393$, $\phi_{HD} = 0.308$), above which they decreased slightly at temperatures up to 700^oC.

In order to evaluate whether or not the maximum porosities are logical, recall the idea that the two types of C-S-H are formed from two different *maximum* packing densities of the C-S-H globules (monosized spheres). However, now an evaluation of the *minimum* possible packing density of monosized spheres is valuable. Molecular dynamics simulations show that monosized spheres behave like a gas at porosities above $\phi_0 = 0.51$, behave like a liquid at porosities from $\phi_0 = 0.45 - 0.51$, and behave like a solid at porosities below $\phi_0 = 0.45$ [2]. However, although the theoretical maximum porosity of a solid was found to be $\phi_0 = 0.44$, the maximum porosity observed experimentally was $\phi_0 = 0.42$ [2]. This maximum porosity corresponds to the *minimum* possible packing density of monosized spheres.

Using these results, the maximum estimated porosities ($\phi_{LD} = 0.393$, $\phi_{HD} = 0.308$) are physically possible because they are below the maximum observed porosity of a solid material ($\phi_0 = 0.42$). Furthermore, it is interesting to note that the maximum porosity of LD C-S-H is quite close to the porosity corresponding to the minimum packing density of monosized spheres. As a result, it appears that LD C-S-H nearly achieves its loosest possible packing state at 550°C, at the end of the primary range of C-S-H dehydration. The decrease in gel porosities at higher temperatures support the possibility of a rearrangement or transformation of the microstructure in the secondary range of C-S-H dehydration.

8.5 Summary and Conclusions of Microporoelastic Modeling

In this chapter, the microporoelastic models introduced in the previous chapter were applied to experimental results in order to gain a better understanding of the effect of high temperature on cement paste. First, the scales of investigation of microindentation and nanoindentation were linked using an upscaling scheme. Second, a downscaling scheme was used to pinpoint sources of high temperature degradation at 'Level 0' of the multiscale microstructure. The following conclusions were drawn:

- **Upscaling from 'Level I' to 'Level II':** Both the MT and SC scheme were used to upscale nanoindentation results for comparison with microindentation results. Both schemes predicted the results of microindentation remarkably well, indicating that microporoelastic modeling can be effectively used for cementitious materials. As a result of upscaling, three primary sources of high temperature elasticity degradation of cement paste were identified:
    - C-S-H dehydration: C-S-H dehydration caused a decrease in the elasticity of both C-S-H phases. As a result, the source of high temperature elasticity degradation was determined to be at a smaller scale ('Level 0').
    - CH dehydration: CH dehydration caused an increase in capillary porosity due to

rapid shrinkage of the CH phase. This increase in capillary porosity was confirmed by MIP results.

  - Increase in Capillary Porosity: The capillary porosity increases as a result of CH dehydration between 400-550°C, but continues to increase at higher temperatures. Again, this increase in capillary porosity was confirmed by MIP results.

- **Downscaling from 'Level I' to 'Level 0':** Although the effects of C-S-H dehydration on the elasticity were observed at 'Level I', downscaling was used to pinpoint the source of high temperature elasticity degradation at 'Level 0'. The SC scheme was determined to accurately represent the microstructure of C-S-H and was used for downscaling. As a result of downscaling, two additional sources of high temperature elasticity degradation were identified:

  - C-S-H Globule: Nanoindentation and thermogravimetry were used to determine the high temperature elasticity degradation of the C-S-H globule at all temperatures of investigation.
  - Gel Porosity: The increase in gel porosity above 300°C identified by Komonen *et al.* [35] and Jumppanen [32] was estimated. The LD C-S-H gel porosity (ϕ_{LD}) approached the porosity corresponding to the minimum packing density of monosized spheres at 550°C, which corresponds to the end of the primary range of C-S-H dehydration.

In conclusion, microporoelastic modeling was successfully used to identify the primary sources of high temperature degradation all the way down to 'Level 0' of the multiscale microstructure of cementitious materials.

Chapter 9

Towards an Engineering Model for Cement Paste Exposed to High Temperatures

Thus far, experimental investigation and microporoelastic modeling have been used to identify the primary sources of high temperature degradation of cement paste. These sources of degradation were determined to be inherent properties of the various phases that make up cement paste at several different scales of the microstructure. With this knowledge in hand, the effects of high temperature exposure on an any type of cement paste can be predicted. This is because the cement paste mix design only determines the volume fractions of the phases present in any given cement paste, not the properties of each phase. If the volume fractions can be determined as a function of the mix design, than the high temperature response of any cement paste can be predicted. As a result, an engineering model for predicting the response of any cement paste to high temperature exposure can be obtained.

The goal of this chapter is to take the first steps toward such an engineering model. First, a model for determining the volume fractions of the cement paste phases from the mix design will be introduced. Second, the results of microporoelastic modeling will be used to develop an engineering tool for predicting the effect of high temperature exposure on a range of cement paste mixes. Last, the engineering model predictions will be compared to results in the literature.

9.1 Hydration Model for Determining Initial Volume Fractions

Several researchers have attempted to determine the volume fractions of the phases of cement paste as a function of the mix design. However, an attempt to incorporate all possible cement paste mix designs in this preliminary investigation into the effects of high temperatures is unrealistic. Additionally, the primary property which affects the phase volume fractions is the w/c ratio. As a result, only the effect of the w/c ratio on the phase volume fractions will be considered.

Powers and Brownyard [46] developed the first model which allowed the calculation of the volume fractions of cement paste from the mix design. Their model, based on experimental data, provides an effective way of estimating the volume fractions of the hydration products (f_{hyd}), the unhydrated clinker ($f_{clinker}$), and the capillary porosity (f_{cap}), in addition to the volumetric shrinkage (f_{shrink}):

$$f_{hyd} = 2.12\,(1-p)\,\xi \tag{9.1}$$

$$f_{clinker} = (1-p)\,(1-\xi) \tag{9.2}$$

$$f_{cap} = p - 1.32\,(1-p)\,\xi \tag{9.3}$$

$$f_{shrink} = 0.2(1-p)\xi \tag{9.4}$$

where ξ is the degree of hydration and p is the total initial porosity, which need to be determined. Powers and Brownyard estimated the total initial porosity from:

$$p = \frac{w/c}{w/c + \frac{\rho_w}{\rho_c}} \tag{9.5}$$

where w/c is the water cement ratio, ρ_w is the density of water ($\rho_w = 1,000\ kg/m^3$), and ρ_c is the density of cement ($\rho_c = 3,150\ kg/m^3$). However, the hydration degree (ξ) still needs to be defined. In this investigation, only completely hydrated cement paste is of interest, so a method of estimating the maximum hydration degree (ξ_{max}) from the w/c ratio is necessary. Powers and Brownyard [46] determined that for w/c ratios greater than 0.38, enough water is present in the mix to achieve complete hydration ($\xi_{max} = 1.0$). However, at lower w/c ratios the maximum hydration degree needs to be defined. Constantinides [15] provides the following estimate of maximum hydration degree which will be used in this investigation:

$$\xi_{max} = 2.7(w/c) \quad \text{for} \quad 0 \leq w/c \leq 0.37 \tag{9.6}$$

$$\xi_{max} = 1.0 \quad \text{for} \quad w/c > 0.37 \tag{9.7}$$

Using these equations, the volume fractions of the hydration products (f_{hyd}), the unhydrated clinker ($f_{clinker}$), and the capillary porosity (f_{cap}) can be determined and are shown displayed in Figure 9-1. However, this hydration model does not distinguish between the hydration products. As discussed in Section 2.1, several hydration products exist, but throughout this study three primary hydration products which have been assumed: LD C-S-H, HD C-S-H, and CH. Therefore, a method of estimating the volume fraction of each of these hydration products is necessary.

First, recall that in Section 6.6.4 the volume fraction of CH was determined to be 11% of the volume fraction of the hydration products. Assuming this holds for all w/c ratios is a reasonable first estimate. With this assumption, the volume fractions of CH (f_{CH}) and C-S-H (f_{CSH}) can be determined:

$$f_{CH} = 0.11(f_{hyd}) \tag{9.8}$$

$$f_{CSH} = 0.89(f_{hyd}) \tag{9.9}$$

Now that the volume fraction of C-S-H has been obtained, only the relative volume percentages of LD C-S-H and HD C-S-H are necessary in order to complete this hydration model. Tennis and Jennings [53] developed the first model for determining the relative volume percentages of the two types of C-S-H from the w/c ratio. However, this model was developed by using experimental data with w/c ratios in the range $0.25 \leq w/c \leq 0.5$, and therefore should be limited to applications in that range. In order to estimate relative volume percentages in a wider range of w/c ratios, Constantinides [15] developed the following relationship:

$$f_{LD}^{rel} = 2.12(w/c) - 0.36 \quad \text{for} \quad 0.17 \leq w/c \leq 0.64 \tag{9.10}$$

$$f_{LD}^{rel} = 0 \quad \text{for} \quad w/c \leq 0.17 \tag{9.11}$$

$$f_{LD}^{rel} = 1 \quad \text{for} \quad w/c \geq 0.64 \tag{9.12}$$

where f_{LD}^{rel} is the *relative* volume percentage of LD C-S-H. The *actual* volume fraction of both types of C-S-H (f_{LD} and f_{HD}) can now be calculated:

$$f_{LD} = f_{LD}^{rel}(f_{CSH}) = (2.12w/c - 0.36)(0.89f_{hyd}) \tag{9.13}$$

$$f_{HD} = (1 - f_{LD}^{rel})(f_{CSH}) = (1.36 - 2.12w/c)(0.89f_{hyd}) \tag{9.14}$$

The initial volume fractions of all the primary phases considered throughout this study have now been defined as a function of the w/c ratio and are plotted in Figure 9-2. This hydration model will be used as a starting point for developing an engineering model which predicts the effects of high temperature exposure on cement paste.

9.2 Development of an Engineering Model

9.2.1 Input Properties

In order to predict the response of cement paste to high temperature exposure, the following information is necessary: the initial phase volume fractions, the effect of high temperature exposure on the phase volume fractions, and the phase properties at all temperatures of investigation. The hydration model introduced in the previous section provides the initial phase volume fractions which are the only properties dependent upon the w/c ratio. The rest of the properties are independent of the w/c ratio, and will now be summarized.

Inherent Phase Properties

The results of nanoindentation and microporoelastic modeling provide the needed inherent phase properties of cement paste. Table 9.1 displays these phase properties, which are unaf-

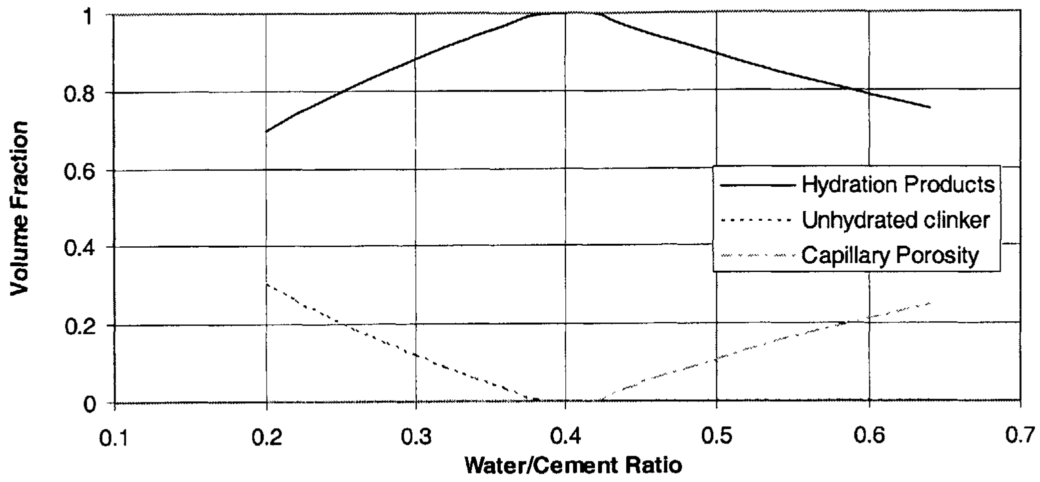

Figure 9-1: Phase volume fractions of fully hydrated cement paste as a function of w/c ratio, as predicted by the Powers and Brownyard model [46].

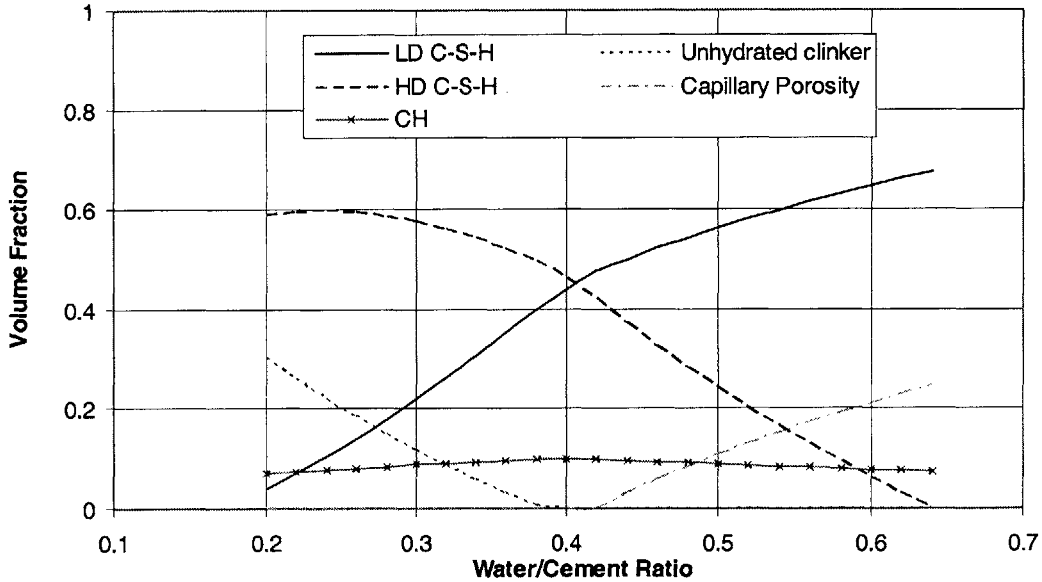

Figure 9-2: Volume fractions of all primary phases of hydrated cement paste as a function of the w/c ratio.

Temperature [°C]	'Level 0' Properties			'Level I' Properties		
	E_{glob} [GPa]	ϕ_{LD}	ϕ_{HD}	E_{CH} [GPa]	E_{CaO} [GPa]	$E_{clinker}$ [GPa]
25	64.1	0.357	0.260	37.3	-	130
105	60.9	0.357	0.260	37.3	-	130
200	57.3	0.357	0.260	37.3	-	130
300	51.8	0.357	0.260	37.3	-	130
400	48.0	0.369	0.278	37.3	-	130
550	44.0	0.393	0.308	-	50	130
700	42.3	0.380	0.290	-	50	130

Table 9.1: Summary of the phase properties used as inputs for the engineering model.

fected by the w/c ratio, and which will be used as inputs for the engineering model. The 'Level 0' phase properties were taken directly from the results of microporoelastic downscaling (see Table 8.9). The 'Level I' phase properties require individual explanation. First, the initial CH elasticity value was determined from nanoindentation, but the CH elasticity was assumed to remain constant at temperatures lower than temperatures which cause CH decomposition. This assumption was made because the source of the change in elasticity in this temperature range has yet to be determined. Second, the elasticity of CaO has not been measured but was assumed to be 50 GPa. Last, the elasticity of all the unhydrated clinker phases were measured by Velez *et al.* [58] and presented in Section 2.2.2 (see Table 2.4). However, because only one unhydrated clinker phase is included in the hydration model, the elasticity of unhydrated clinker was estimated to be 130 GPa.

Effect of High Temperature on the Phase Volume Fractions

Although the initial volume fractions are determined by the w/c ratio, the effect of high temperature on these initial volume fractions is independent of the w/c ratio. The effect of high temperature on the phase volume fractions was determined using nanoindentation and microporoelastic modeling and will now be reviewed:

- **C-S-H Phases:** Nanoindentation results indicated that the relative percentages of LD and HD C-S-H are unaffected by high temperature exposure (see Section 6.6.4).
- **CH Phase:** Nanoindentation indicated that the volume fraction of CH remains constant

up to 400°C (before CH decomposition occurs). During decomposition (between 400-550°C), CH shrinks rapidly by 30% so the volume fraction of CH was reduced by 30% in this temperature range.

- **Capillary Porosity:** MIP results indicate that the capillary porosity remains constant up to 400°C. This was confirmed by microporoelastic upscaling (see Section 8.2). From 400-550°C, MIP results indicate an increase in capillary porosity. Microporoelastic modeling showed that increasing the capillary porosity by the magnitude of the reduction in CH volume fraction caused by CH decomposition, provides a good estimate of the increase in capillary porosity in this temperature range. Between, 550-700°C, microporoelastic upscaling was used to estimate a 20% increase in capillary porosity. This 20% increase will be used for modeling purposes, but it should be noted that the source of this increase is uncertain. It could be a result of heating procedure or macrocracking, which are not inherent phase properties.

9.2.2 Engineering Model

Using the input properties introduced in the previous section, the SC scheme was used to predict the effect of high temperature on the elasticity of cement pastes with a variety w/c ratios. The resulting engineering model is displayed in Figure 9-3. Additionally, the normalized elasticity values of the same cement pastes are plotted as a function of temperature in Figure 9-4.

Figure 9-3 shows that the w/c ratio has a large effect on the magnitude of the modulus of elasticity. However, Figure 9-4 shows that high temperature elasticity degradation is very similar regardless of the w/c ratio. Figure 9-4 does indicate that cement pastes with lower w/c ratios tend to degrade slightly less. However, this trend was a direct result of an increased volume fraction of unhydrated clinker, which was assumed have a constant elasticity at all temperatures. As a result, it seems that the relative effect of high temperature exposure on the elasticity of cement paste is the same regardless of the w/c ratio. This confirms the same conclusions made by Masse [37] from experiments.

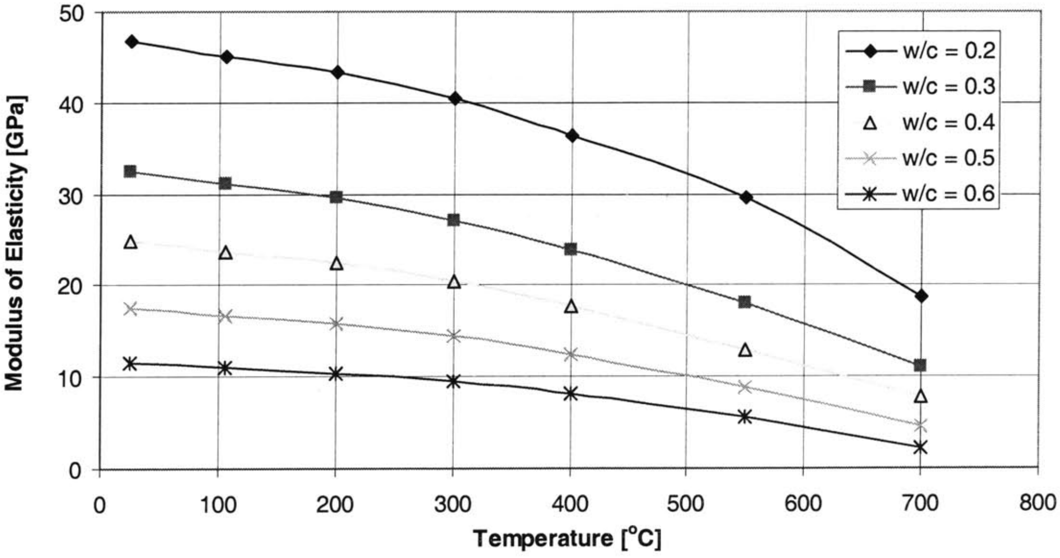

Figure 9-3: Engineering tool for predicting the modulus of elasticity as a function of the w/c ratio and temperature.

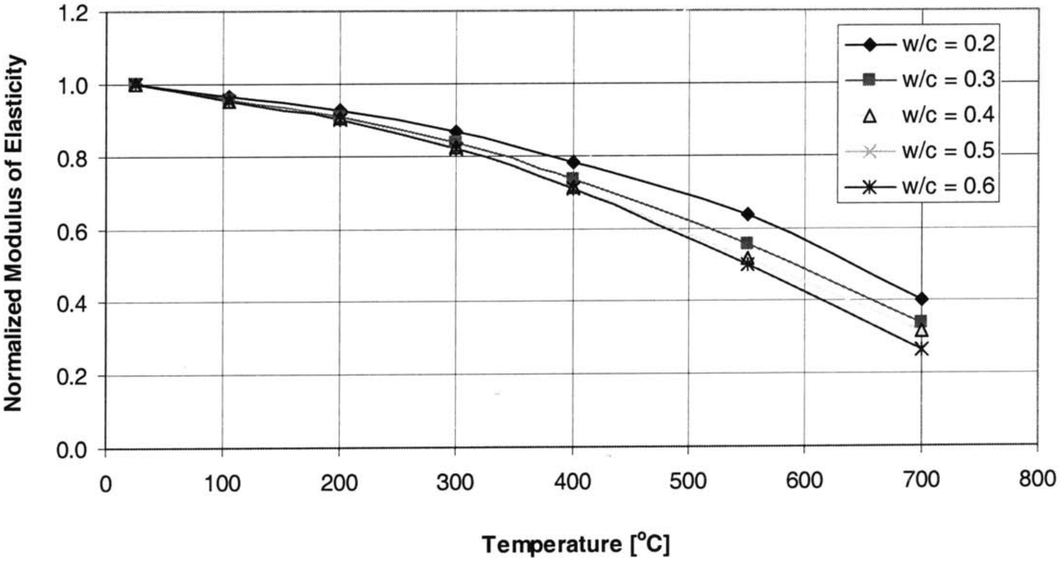

Figure 9-4: Normalized modulus of elasticity as a function of the w/c ratio and temperature as predicted by the engininеering model.

Temperature [°C]:		25	105	200	300	400	550	700	
Data Source	w/c	**Modulus of Elasticity*** [GPa]							e^{**}
Masse *et al.* [37]	0.25	-	36.1	33.1	29.8	26.5	24.5	21.6	0.049
Eng. Model	0.25	38.5	37.0	35.3	32.7	28.9	22.6	14.3	
Dias *et al.* [18]	0.30	27.8	20.9	18.9	15.7	12.5	9.3	7.9	0.139
Model	0.30	32.4	31.0	29.5	27.1	23.8	18.0	11.0	
Masse *et al.* [37]	0.35	-	28.1	24.8	22.9	20.3	18.2	15.3	0.082
Eng. Model	0.35	27.8	26.6	25.2	23.0	20.0	14.8	9.2	
Farage *et al.* [22]	0.40	21.3	19.4	18.4	17.7	-	-	-	0.026
Eng. Model	0.40	24.8	23.7	22.4	20.4	17.7	12.8	7.8	
Masse *et al.* [37]	0.50	-	18.5	16.5	15.8	13.2	12.3	-	0.038
Eng. Model	0.50	17.5	16.7	15.8	14.4	12.4	8.8	4.6	

*Results were interpolated where temperatures do not correspond exactly.

**Fitting error: $e = \frac{1}{n}\sum_{i=1}^{n}\frac{(E_i^{model}-E_i^{measured})^2}{(E_i^{model})^2}$

Table 9.2: Measured and predicted modulus of elasticity values using the engineering model and the results of other investigations.

9.3 Model Validation

In order to validate this engineering tool, comparison with results in the literature is necessary (see Table 9.2 and Figs. 9-5, 9-6, and 9-7). The effectiveness of the engineering model in predicting the results of Masse *et al.* [37], Farage *et al.* [22], and Dias *et al.* [18] will now be discussed.

9.3.1 Comparison with Literature

In general, Figures 9-5 and 9-6 show that the results of Masse *et al.* [37] compare well with the engineering model predictions. More specifically, all three w/c ratios investigated by Masse *et al.* compare remarkably well with engineering model predictions up to 400°C. At 550°C, the model slightly underestimates the results found by Masse *et al.*, and at 700°C, the underestimation is a bit more significantly. Figure 9-7 confirms this underestimation at temperatures above 500°C.

Figures 9-5 and 9-6 show that the model also predicts the results of Farage *et al.* [22] reasonably well. Although the model slightly overestimates the magnitude of the elasticity results found by Farage *et al.*, the model accurately predicts the evolution of the elasticity with respect to temperature up to 300°C. This is also confirmed by Figure 9-7.

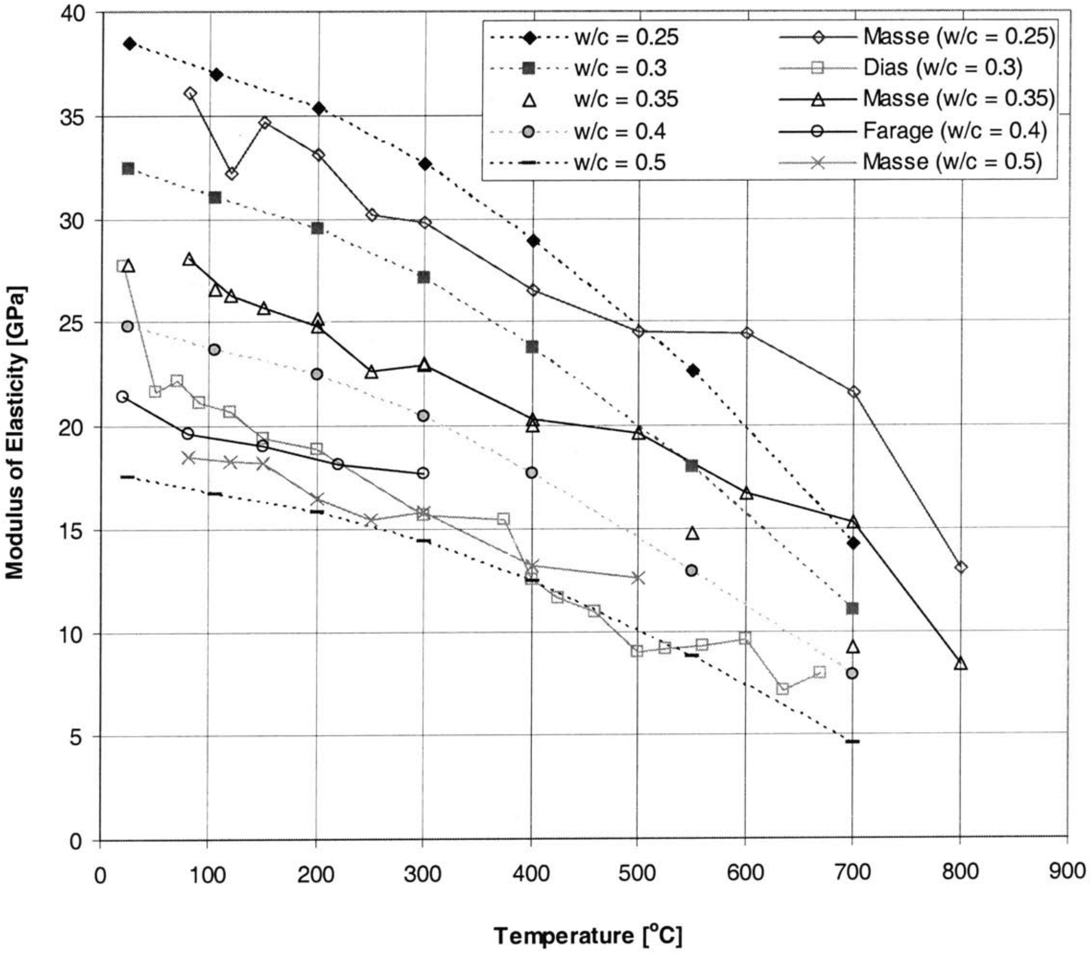

Figure 9-5: Comparison of engineering model with the results of Masse *et al.* [37], Farage *et al.* [22], and Dias *et al.* [18].

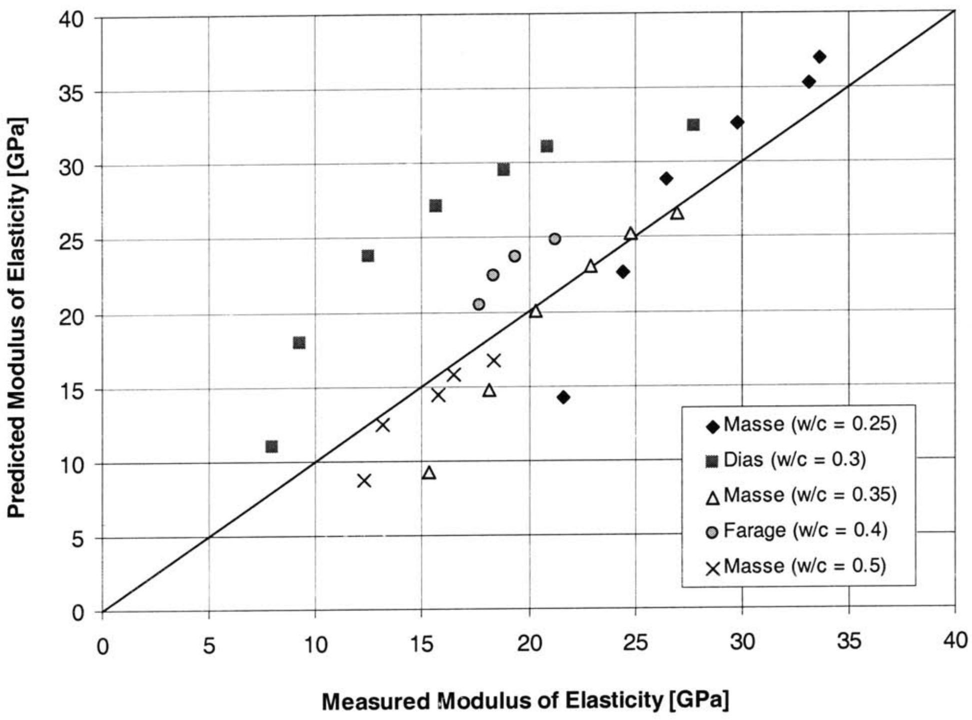

Figure 9-6: Measured versus predicted modulus of elasticity values using the results of Masse *et al.* [37], Farage *et al.* [22], and Dias *et al.* [18].

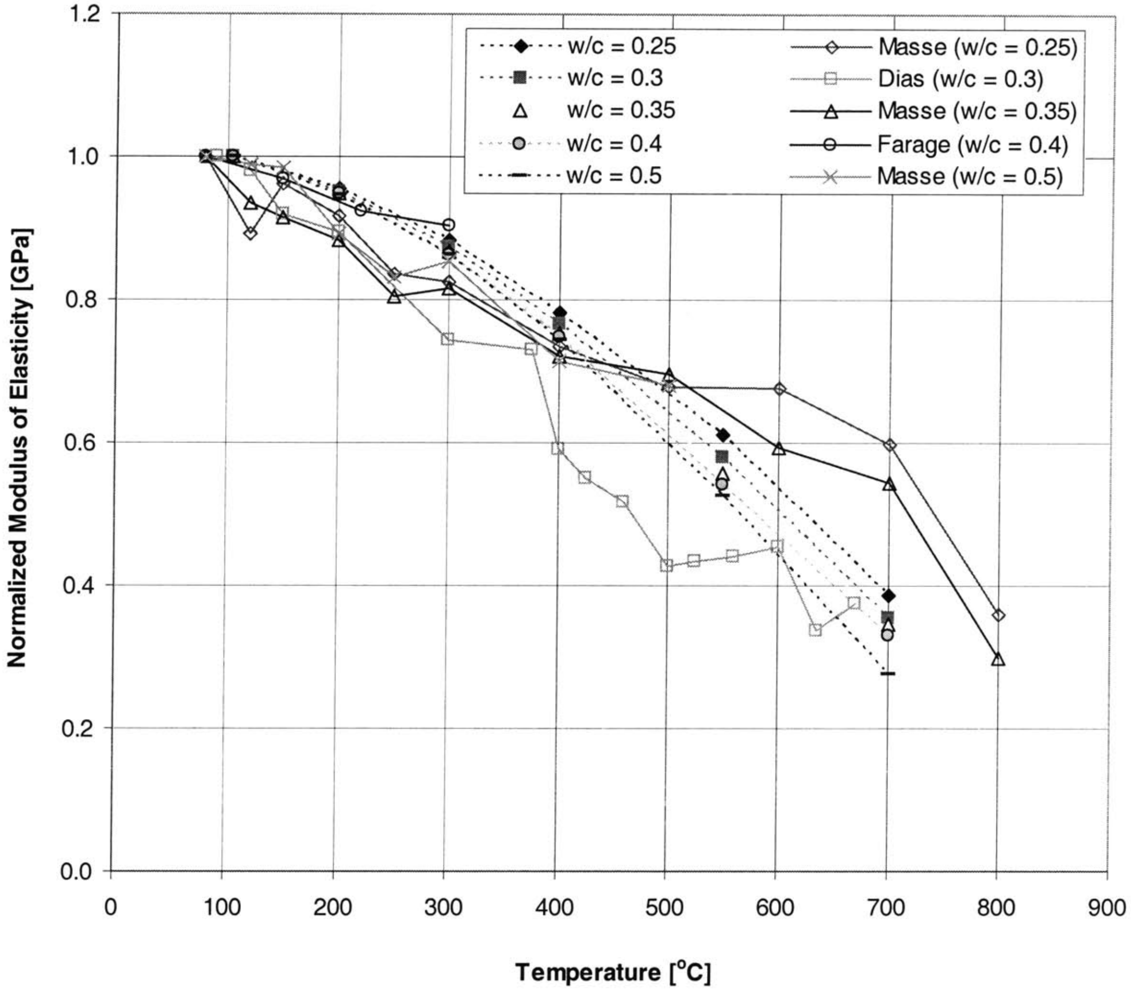

Figure 9-7: Comparison of engineering model with the normalized results of Masse *et al.* [37], Farage *et al.* [22], and Dias *et al.* [19].

Last, Figure 9-5 and 9-6 show that the magnitude of the elasticity results of Dias *et al.* [18] do not compare well with engineering model predictions. However, these results are directly contradictory to the results of Masse *et al.*, so it would be impossible for the model to predict both results accurately. On the other hand, Figure 9-7 shows that the model predicts the evolution of the elasticity with respect to temperature reasonably well. Although, Figure 9-7 shows that the model tends to overestimate the normalized results of Dias *et al.* at higher temperatures.

9.3.2 Discussion

In general, although predicting all the results in the literature accurately is impossible because of inherent contradictions, the model effectively predicted the elasticity of different w/c ratio cement pastes up to 400^{o}C. However, at higher temperatures, the model overestimated the normalized results of Dias *et al.*, but underestimated the normalized results of Masse *et al.* Additionally, after exposure to these higher temperatures (>400^{o}C), researchers have observed a significant increase in microcracking and voids (see Table 2.6). Based on these observations, it seems that microcracking could account for the discrepancy in the normalized results of Masse *et al.* and Dias *et al.* One possible source of differential microcracking would be the heating procedure. Dias *et al.* used a heating rate of 1 K/min (as was used in this study), whereas Masse *et al.* used a heating rate of 0.1 K/min. However, this engineering model estimates a valuable average of the two results, and tends towards a conservative estimate of the elasticity at these higher temperatures.

In conclusion, inherent high temperature degradation of each phase can account for the high temperature elasticity degradation of cement paste up to 400^{o}C, but at higher temperatures other factors seem to influence material degradation. However, using increased macroporosity to estimate the effects of these other factors, the engineering model still provides a valuable estimate of the elasticity of cement paste at these higher temperatures.

9.4 Summary and Conclusions

Using the hydration models of Powers and Brownyard [46] and Constantinides [15], in combination with the results of this study, the first steps towards developing an engineering tool that can predict the elasticity of any cement paste at any temperature have been taken. With the addition of other materials (silica fume, fly ash, etc.) into the hydration model, this engineering model could be expanded to a wider range of cement paste mix designs.

Part IV

Conclusions and Perspectives

Chapter 10

Conclusions

10.1 Summary of Main Findings

The primary goal of this study was to identify the sources of high temperature degradation of cement paste. In order to accomplish this, the results of previous research studies, new experimental investigations, and microporoelastic modeling were used. The following summarizes the main findings:

1. **Macroscopic Experimental Investigations:** Macroscopic investigations showed that the cement paste used in this study behaved similarly to cement pastes used in previous experimental investigations. Thermogravimetry results were particularly valuable for estimating the thermal elasticity degradation of the C-S-H phases. Additionally, experimentation at this scale was extremely valuable to get a general feeling for the effects of high temperature on cement paste, which is critical for a more comprehensive understanding of the subject.

2. **Microindentation:** Microindentation results showed that relatively deep indentation can be used to obtain the properties of homogenized cement paste which traditionally have been measured at the macroscale. This indicates that the majority of high temperature degradation occurs at a scale below the microscale. Additionally, comparison of macroscopic compressive strength results and microindentation hardness results show a clear relationship between hardness and compressive strength at this scale.

3. **Nanoindentation:** Nanoindentation can be used to measure the effects of high temperature exposure on the phases of cement paste. The elasticity and hardness of the primary phases of cement paste (LD C-S-H, HD C-S-H, CH) were determined after exposure to temperatures from 25°C up to 700°C. Additionally, nanoindentation was used to estimate the volume fractions of the various phases. Transformation of LD C-S-H to HD C-S-H during heating was determined not to occur.

4. **Microporoelastic Modeling:** Nanoindentation and microindentation results were successfully linked using microporoelastic upscaling techniques. In the process, the effect of high temperature exposure on the capillary porosity was estimated. Using microporoelastic downscaling techniques, the inherent gel porosities and C-S-H globule elasticity values were determined at all temperatures of investigation. Additionally, the effects of high temperature exposure on the gel porosity and capillary porosity found using microporoelastic modeling compared well with the qualitative results of MIP investigations in the literature. Microporoelastic modeling results showed the Self-Consistent Scheme to be an effective homogenization scheme for cementitious materials.

10.2 Main Contribution of this Study

The main findings of this study were just summarized, but the primary contribution of this study lies in the identification of two sources of high temperature elasticity degradation at the nanoscale:

1. Dehydration within the C-S-H globules which can be estimated using mass loss measurements.

2. A decrease in packing density of both LD and HD C-S-H after exposure to temperatures greater than 300°C.

The identification of these sources was only possible through a unique combination of experimental (microindentation and nanoindentation) and theoretical (microporoelastic modeling) investigations.

10.3 Suggestions for Future Research

Microindentation, nanoindentation, and microporoelastic modeling allow access to the properties of cement paste and of the cement paste phases at very small scales. The application of these methods to determine the effects of high temperature exposure on cement paste has led to the identification of several possible areas for future research:

1. **Comprehensive Elasticity Engineering Model:** The engineering model developed can be used to predict the high temperature response of cement pastes with various w/c ratios. This model could be expanded to include other materials which are often included in cement paste mix designs (silica fume, fly ash, etc.). Furthermore, with knowledge of the effects of high temperature exposure on sands and aggregates, the engineering model could be expanded to include any concrete mix design.

2. **Transient Effects:** The focus of this study was to determine the *material* response of the cement paste phases when exposed to high temperatures. Transient effects (primarily caused by thermal gradients) were avoided by using slow heating and cooling rates. Such transient effects have been studied at the macroscale [54] [55], but a better understanding of thermal effects at the microscale is still necessary. Combining the results of this study with results of investigations regarding transient effects could be used to develop a finite-element model for predicting the *structural* response of concrete exposed to high temperatures.

3. **Time-Dependent Properties (Creep):** Methods for determining time-dependent properties from indentation data are currently under investigation [57]. If successful, these methods could be used to determine the effects of high temperature exposure on the time-dependent properties of the cement paste phases ('Level I') and homogenized cement paste ('Level II').

4. **Strength Properties:** In this study, the effects of high temperature exposure on the elastic properties of cement paste were modeled, but a method of linking the hardness properties determined at different scales is not yet available. Additionally, methods for determining strength properties from indentation hardness results are currently under

investigation [25]. If successful, these methods could be directly applied to the indentation results of this investigation, and strength properties could be determined at the various scales of the multiscale microstructure. Furthermore, an engineering model (similar to the one developed in this study for elasticity) could be developed for predicting the strength properties of any cement paste or concrete.

10.4 Industrial Benefits

Identification of the inherent sources of high temperature cement paste degradation at small scales has led to the development of an engineering model which can predict the effects of high temperature on the elasticity of any cement paste. Such a model could be directly implemented into design codes. Additionally, such an engineering model could be used as a design tool for optimizing concrete mix designs for applications where high temperature exposure is certain (furnace, reactors, etc.) or uncertain (fire). Furthermore, identifying the *material* response of the cement paste phases is the first step towards the development of a finite-element model which can simulate the *structural* response of concrete exposed to high temperatures. Such simulations could be used to model the response of an entire structure when exposed to high temperature (fire or otherwise) in order to ensure structural safety.

Bibliography

[1] Acker, P. (2001). 'Micromechanical analysis of creep and shrinkage mechanisms, in: F.-J. Ulm, Z. Bažant, F. Wittman (Eds.), Creep, Shrinkage and Durability Mechanics of Concrete and other Quasi-Brittle Materials, Elsevier, Oxford, UK.

[2] Aste, T., Saadatfar, M., Sakellariou, A., and Senden, T.J. (2004). 'Investigating the geometrical structure of disordered sphere packings', *Physica A*, 339, 16-23.

[3] ASTM C39-03. (2003). 'Standard Test Method for Compressive Strength of Cylindrical Concrete Specimens', ASTM International.

[4] ASTM C215-02. (2002) 'Standard Test Method for Fundamental Transverse, Longitudinal, and Torsional Frequencies of Concrete Specimens', ASTM International.

[5] ASTM E384-99. (1999). 'Standard Test Method for Microindentation Hardness of Materials', ASTM International.

[6] Bažant, Z.P., and Kaplan, M.F. (1996). 'Concrete at High Temperatures: Material Properties and Mathematical Models', Longman Group, England.

[7] Bažant, Z.P., and Zhou, Y. (2001). 'Why did the World Trade Center collapse? - Simple Analysis', *Journal of Engineering Mechanics*, ASCE, in press.

[8] Beaudoin, J. (1983). 'Comparison of mechanical properties of compacted calcium hydroxide and portland cement paste systems', *Cement and Concrete Research*, 13(3), 319-324.

[9] Bulychev, S.I., Alekhin, V.P., Shorshorov, M.Kh., Ternovskii, A. P., and Shnyrev, G. D. (1975). Ind. Lab., Transl: Zavodskaya Laboratoria, 41, 1137.

[10] Cheng, Y.T., and Cheng, C.M. (2004). 'Scaling, dimensional analysis, and indentation measurements', *Materials Science and Engineering*, R44, 91-149.

[11] Constantinides, G., Ulm, F.-J., and van Vliet, K.J. (2003). 'On the use of nanoindentation for cementitious materials', *Materials and Structures* 205 (Special issue of Concrete Science and Engineering) RILEM, 191–196.

[12] Constantinides, G., and Ulm, F.-J. (2004). 'The effect of two types of C–S–H on the elasticity of cement-based materials: Results from nanoindentation and micromechanical modeling', *Cement and Concrete Research*, 34(1), 67–80.

[13] Constantinides, G., and Ulm, F.-J. (2004). 'Stiffness, strength and creep behavior of heat-cured cement pastes: a multiscale indentation investigation', MIT Research Report to Lafarge, Cambridge, MA.

[14] Constantinides, G., and Ulm, F.-J. (2005). 'Contact Area Estimators for Berkovich and Cube Corner Indentation of Cohesive-Frictional Materials', MIT Research Report to Lafarge, Cambridge, MA.

[15] Constantinides, G. (2005). 'Material Invariant Properties of Cement-Based Materials: An Experimental Microporomechanics Approach', MIT D.Sc. Dissertation, Cambridge, MA.

[16] Cook, R.A., and Hover, K.C. (1999). 'Mercury porosimetry of hardened cement pastes', *Cement and Concrete Research*, 29, 933-943.

[17] Diamond, S. (2000). 'Mercury porosimetry: An inappropriate method for the measurement of pore size distributions in cement-based materials', *Cement and Concrete Research*, 30, 1517-1525.

[18] Dias, W.P.S., Khoury, G.A., and Sullivan, P.J.E. (1990). 'Mechanical Properties of Hardened Cement Paste Exposed to Temperatures up to 700 C (1292 F)', *ACI Materials Journal*, 87(2), 160-166.

[19] Dias, W.P.S., Khoury, G.A., and Sullivan, P.J.E. (1990). 'Shrinkage of Hardened Cement Paste at Temperatures up to 670 C (1238 F)', *ACI Materials Journal*, 87(3), 204-209.

[20] Di Maio, A., Giaccio, G., and Zerbino, R. (2002). 'Non-destructive tests for the evaluation of concrete exposed to high temperatures', *Cement, Concrete, and Aggregates*, 24(2), 58-67.

[21] Eshelby, J. (1957). 'The determination of the elastic field of an ellipsoidal inclusion, and related problems', *Proceedings of the Royal Society London, Series A*, 241, 376–396.

[22] Farage, M.C.R., Sercombe, J., and Galle, C. (2003). 'Rehydration of microstructure of cement paste after heating at temperatures up to 300 °C', *Cement and Concrete Research*, 33, 1047-1056.

[23] Feldman, R. F., and Sereda, P. J. (1968). 'A model for hydrated portland cement paste as deduced from sorption-length change and mechanical properties', *Materials and Structures*, 1(6), 509-519.

[24] Feldman, R.F., and Ramachandran, V.S. (1971). 'Differentiation of interlayer and adsorbed water in hydrated Portland cement by thermal analysis', *Cement and Concrete Research*, 1, 607-620.

[25] Ganneau, F.P., Constantinides, G., and Ulm, F.-J. (2005). 'Dual-indentation technique for the assessment of strength properties of cohesive-frictional materials', accepted by the *International Journal of Solids and Structures* (in press).

[26] Galle, C. (2001). 'Effect of drying on cement-based materials pore structure as identified by mercury intrusion porosimetry: A comparative study between oven-, vacuum-, and freeze-drying', *Cement and Concrete Research*, 31, 1467-1477.

[27] Handoo, S.K., Agarwal, S., and Agarwal, S.K. (2002). 'Physicochemical, mineralogical, and morphological characteristics of concrete exposed to elevated temperatures', *Cement and Concrete Research*, 32, 1009-1018.

[28] Harmathy, T.Z. (1970). 'Thermal properties of concrete at elevated temperatures', *ASTM Journal of Materials*, 5(1), 47-74.

[29] Harmathy, T.Z. (1993). 'Fire Safety Design & Concrete', Longman Group, England.

[30] Hill, R. (1958). 'A self-consistent mechanics of composite materials', *Journal of the Mechanics and Physics of Solids*, 13, 213.

[31] ISO 14577 (2002). 'Metallic Materials - Instrumented indentation test for hardness and material parameters'.

[32] Jumppanen, U.-M., Dieterichs, U., and Hinrichsmeyer, K. (1986). 'Material Properties of F-Concrete at High Temperatures', Research Report 452, Technical Research Centre of Finland, Espoo.

[33] Jennings, H.M. (2000). 'A model for the microstructure of calcium silicate hydrate in cement paste', *Cement and Concrete Research*, 30(1), 101-116.

[34] Khoury, G.A., Majorana, C.E., Pesavento, F., and Schrefler, B.A. (2002). 'Modelling of heated concrete', *Magazine of Concrete Research*, 54(2), 77-101.

[35] Komonen, J., and Penttala, V. (2003). 'Effects of High Temperature on the Pore Structure and Strength of Plain and Polypropylene Fiber Reinforced Cement Pastes', *Fire Technology*, 39, 23-34.

[36] Lin, W.-M., Lin, T.D., and Powers-Couche, L.J. (1996). 'Microstructure of Fire-Damaged Concrete', *ACI Materials Journal*, 93(3), 199-205.

[37] Masse, S., Vetter, G., Boch, P., and Haehnel, C. (2002). 'Elastic modulus changes in cementitious materials submitted to thermal treatments up to 1000°C', *Advances in Cement Research*, 14(4), 169-177.

[38] Monteiro, P.J.M., and Chang, C.T. (1995). 'The elastic-moduli of calcium hydroxide', *Cement and Concrete Research*, 25(8), 1605-1609.

[39] Mori, T., and Tanaka, K. (1973). 'Average stress in matrix and average elastic energy of materials with misfitting inclusions', *Acta Metallurgica*, 21(5), 571-574.

[40] Němeček, J., Kopecký, L., and Bittnar, Z. (2004). 'Heat influence on micromechanical properties of cement pastes', Fracture Mechanics of Concrete Structures, Li et al (editors), Vol. 1, 499-505.

[41] Oliver, W.C., and Pharr, G.M. (1992). 'An improved technique for determining hardness and elastic modulus using load and displacement sensing indentation experiments', *Journal of Materials Research*, 7(6), 1564–1583.

[42] Oliver, W.C., and Pharr, G.M. (2004). 'Measurement of hardness and elastic modulus by instrumented indentation: Advances in understanding and refinements to methodology', *Journal of Materials Research*, 19(1), 3–20.

[43] Petzold, A., and Rohr, M. (1970). 'Concrete for High Temperatures', Maclaren and Sons, London.

[44] Piasta, J., Sawicz, Z., and Rudzinski, L. (1984). 'Changes in the structure of hardened cement paste due to high temperature', *Materiaux et Constructions*, 17(100), 291-296.

[45] Piasta, J. (1984). 'Heat deformations of cement paste phases and the microstructure of cement paste', *Materiaux et Constructions*, 17(102), 415-420.

[46] Powers, T., and Brownyard, T. (1948) 'Studies of the physical properties of hardened portland cement paste', Bulletin 22, Portland Cement Association, Chicago, IL.

[47] Richard, P., Nicodemi, M., Delannay, R., Ribiere, P., and Bideau, D. (2005). 'Slow relaxation and compaction of granular systems', *Nature Materials*, 4, 121-128.

[48] Rostasy, R.S., Weiss, R., and Weidemann, G. (1980). 'Changes of Pore Structure of Cement Mortars due to Temperature', *Cement and Concrete Research*, 10(2), 157-164.

[49] Schneider, U., and Diederichs, U. (1983). 'Detection of Crack by Mercury Penetration Measurements', Fracture Mechanics of Concrete, Elsevier, Amsterdam, 207-222.

[50] Shelby, M.D., Tai, H.J., and Jang, B.Z. (2004). 'Vibration based non-destructive evaluation of polymer composites', *Polymer Engineering and Science*, 31(1), 47-55.

[51] Sneddon, I.N. (1965). 'The Relation Between Load and Penetration in the Axisymmetric Boussinesq Problem for a Punch of Arbitrary Profile', *International Journal of Engineering Science*, 3, 47-57.

[52] Taylor, H.F.W. (1997). 'Cement Chemistry', 2nd Edition, Thomas Telford, London, England.

[53] Tennis, P.D., and Jennings, H.M. (2000). 'A model for two types of calcium silicate hydrate in the microstructure of Portland cement pastes', *Cement and Concrete Research*, 30(6), 855-863.

[54] Ulm, F.-J., Coussy, O., and Bažant, Z.P. (1999). 'The "Chunnel" Fire. I: Chemoplastic Softening in Rapidly Heated Concrete', *Journal of Engineering Mechanics*, ASCE, 125(3), 272-282.

[55] Ulm, F.-J., Acker, P., and Lévy, M. (1999). 'The "Chunnel" Fire. II: Analysis of Concrete Damage', *Journal of Engineering Mechanics*, ASCE, 125(3), 283-289.

[56] Ulm, F.-J., Constantinides, G., and Heukamp, F.H. (2004). 'Is concrete a poromechanics material? – A multiscale investigation of poroelastic properties', *Materials and Structures*, Special issue of *Concrete Science and Engineering*, Vol. 37 (265), 43–58.

[57] Vandamme, M., and Ulm, F.-J. (2005). 'Viscoelastic solutions for conical indentation', accepted by the *International Journal of Solids and Structures* (in press).

[58] Velez, K., Maximilien, S., Damidot, D., Fantozzi, G., and Sorrentino, F. (2001). 'Determination by nanoindentation of elastic modulus and hardness of pure constituents of Portland cement clinker', *Cement and Concrete Research*, 31(4), 555-561.

[59] Wittmann, F.H. (1986). 'Estimation of the modulus of elasticity of calcium hydroxide', *Cement and Concrete Research*, 16(6), 971-972.

[60] Wendlandt, W.W. (1986), 'Thermal Analysis', 3rd Edition, John Wiley & Sons, Inc., New York, USA.

[61] Xu, Y., Wong, Y.L., Poon, C.S., and Anson, M. (2001). 'Impact of high temperature on PFA concrete', *Cement and Concrete Research*, 31, 1065-1073.

[62] Zaoui, A. (2002). 'Continuum micromechanics: Survey.' *Journal of Engineering Mechanics (ASCE),* 128(8), 808–816.

4983-27